The comprehensive analysis of milling stability and surface location error with considering the dynamics of workpiece

Der Fakultät Maschinenwesen

der

Technischen Universität Dresden

zur

Erlangung des akademischen Grades

Doktoringenieur (Dr.-Ing.)

vorgelegte Dissertation

From   M.Sc. Dongqian Wang
born on 5th November, 1990 in Hebei, P.R. China

Completion date: 15.04.2020

Submission date: 26.11.2020

Defence date: 03.03.2021

Reviewer: Prof. Dr.-Ing. Steffen Ihlenfeldt

                      Prof. Dr.-Ing. Welf-Guntram Drossel

Chairman: Prof. Dr.-Ing. habil. Uwe Füssel

Acknowledgements

Abstract

Cutting movement is still one of the main means to obtain the desired machined surface. As the most representative cutting method in subtractive manufacturing, milling is widely used in industrial production. However, the chatter induced by the dynamic interaction between machine tool and process not only reduces the accuracy of the machined workpiece, but also increases the tool wear and affects the rotary accuracy of the spindle. The stability lobe diagram can provide stable machining parameters for the technicians, and it is currently an effective way to avoid chatter. In fact, the dynamic interaction between the machine tool and process is very complicated, which involves the machine tool, milling tool, workpiece and fixture. The induced mechanism of chatter depends on different machining scenarios and is not entirely dependent on the vibration modes of milling tool. Therefore, it is important to obtain stable machining parameters and to know the dynamic surface location error distribution, which can ensure machining quality and improve machining efficiency.

In this dissertation, two methods for constructing stability lobe diagram are first introduced, and then two machining scales, macro milling and micro milling, are studied. For the macro-milling scale, the dynamic response of the in-process workpiece with time-varying modal parameters during the material removal process is analyzed. The stability lobe diagrams for thin-walled workpiece and general workpiece with continuous radial immersion milling are established respectively. Besides, the cumulative surface location error distribution is also studied and verified for the general workpiece. For the micro-milling scale, the dynamics at the micro-milling tool point is obtained by means of the receptance coupling substructure analysis method. The stability lobe diagram and surface location error distribution are analyzed under different restricted/free tool overhang lengths. The relationship between measurement results and burrs is further explained by cutting experiments, and the difference between the two milling scales is compared in the end.

Keywords: Macro & micro milling; In-process workpiece; Frequency response function; Stability lobe diagram; Cumulative surface location error.

TABLE OF CONTENTS

Nomenclature

a_e	Radial depth of cut
b	Axial depth of the cut
$\mathbf{C}$	Damping matrix
D	Diameter of the milling tool
f_d	Damped natural frequency (Hz)
f_h	Quasi-periodic chatter frequency (Hz)
f_n	Frequency function of dominant mode
f_{p1}	Period one frequency (Hz)
f_{p2}	Period doubling frequency (Hz)
f_{sp}	Spindle frequency (Hz)
f_{tp}	Tooth passing frequency (Hz)
f_z	Feed per tooth
$\mathbf{F}(t)$	Milling force
G	Assembly receptance
$h(t)$	Instantaneous uncut chip thickness
h_{sk_v}	Entry of R_{sk_v} : displacement-to-force
H_{11-x}, H_{11-y}	Receptance of micro-milling tool point in X and Y direction
$\mathbf{K}$	Stiffness matrix
K_{pd}	Indentation coefficient
K_t, K_r	Cutting force coefficients in tangential and normal direction
K_{te}, K_{re}	Edge force coefficients in tangential and normal direction

k_v	Excitation location
l_{sk_v}	Entry of R_{sk_v}: displacement-to-couple
$\mathbf{M}$	Mass matrix
m_t	Number of excited modes of milling tool
m_w	Number of excited modes of workpiece
N	Number of teeth
N_f	Ordinal number of lobe
n_{sk_v}	Entry of R_{sk_v}: rotation-to-force
p_{sk_v}	Entry of R_{sk_v}: rotation-to-couple
r	Tool radius
r_e	Radius of cutting edge
R_{sk_v}	Generalized receptances matrix
s	Measurement location
s_c	Current position vector
s_p	Previous position vector
T	Tooth passing period
Ω	Spindle speed (rpm)
ζ	Damping ratio
ω_r	Natural frequency (rad/s)
ω_{rd}	Natural frequency matrix (rad/s)
ω_c	chatter frequency (rad/s)
τ	Time delay

ϕ	Angular position
Φ	State transition matrix
$(w,\, b_s)$	Normal vector and displacement of hyperplane
μ	Frictional coefficient
ε	Phase shift between previous and current tooth
ψ	Tool cutting angle (counterclockwise)
ψ'	Phase shift of eigenvalue
δ	Rotation angle between previous and current tooth

Abbreviation

CMM	Coordinate Measurement Machine
CMS	Component Mode Synthesis
CSLE	Cumulative Surface Location Error
EMA	Experimental Modal Analysis
FEM	Finite Element Method
FRF	Frequency Response Function
IPW	In-process Workpiece
MRR	Material Removal Rate
RC	Receptance Coupling
RCSA	Receptance Coupling Substructure Analysis
SDM	Structural Dynamic Modification
SLD	Stability Lobe Diagram
SLE	Surface Location Error
SVM	Support Vector Machine

1 Introduction

1.1 Background and scientific significance

Milling process involves machine tool, milling tool, workpiece and fixture, and it is important to improve machining efficiency and make the whole process stable and controllable [1]. However, the unfavorable interactions between process and machine tool, such as machining error and chatter, threaten the milling process [2], [3]. There are two imperative indicators to evaluate machining process and machined surface: stability lobe diagram (SLD) and surface location error (SLE). The SLD can show stable and unstable prediction regions before machining. The SLE is an offset error defined as the maximal distance between the desired surface and the machined surface. On the basis of SLD and SLE, the stable parameters can be selected and the machining error can be controlled within the range of machining tolerance. Therefore, it is necessary and important to obtain the SLD and SLE. In terms of machining scale, milling process can be divided into macro-milling and micro-milling. In the macro-milling process from rough to finish machining, the material is removed continuously and the dynamic behavior of the workpiece changes accordingly. As a result, when the dimension of workpiece reaches the condition of thin-walled workpiece, the dynamics of workpiece makes the milling process more complicated. When the in-process workpiece (IPW) dynamics is ignored, though the dynamic model of the system can be simplified, the predicted SLD and SLE will deviate the practical machining results severely. Therefore, the stability analysis of in-process thin-walled workpiece and SLE during continuous machining should be given higher priority in macro-milling.

As we all know, multiple factors are involved in the dynamic model. For example, the cutting force model includes the regenerative effect and process damping, and the dynamic equation includes several coupled modes of tool-workpiece system. Considering the multiple modes of tool-workpiece and process damping effect can further expand the influence factors of traditional model and effectively improve the prediction accuracy. After the dynamics of IPW is determined, especially for the continuous radial material removal, the prediction model for SLD and SLE along tool path will be constructed with the modal parameters from both machine tool and IPW. According to the SLD and the predicted model of SLE, the machining quality will be improved by adjusting the depth of cut, the spindle speed and cutter location compensation, which helps to control the error within allowable range. The comprehensive analysis of SLD and SLE with dynamics of workpiece can overcome the

shortcomings of machining parameters based on the experience database or a single static SLD, which has higher engineering practice.

With the rapid development of miniaturized components, many products require higher accuracy with significantly decreased size. Like macro-milling, micro-milling also faces the problems of machining stability and error. Due to the existence of size effect in micro-milling, micro-milling also exhibits its unique processing characteristics [4]. In addition, the geometric size of micro-milling is small, and its rigidity is far less than that of workpiece. Therefore, the research focus of micro-milling is to determine the frequency response function (FRF) of tool point. Through the dynamic analysis of the micro-milling process, the error during stable machining process can be predicted and the appropriate machining parameters can be obtained.

1.2 Literature review

1.2.1 SLD and IPW dynamics for flexible machining system

Due to the increasing popularity of lightweight design, thin-walled workpieces are widely used in aerospace, communications and other fields. With characteristics of geometric topology and weak rigidity of thin-walled workpiece, great challenges are brought to the milling process. Besides, the interaction effects between process and machine tool, such as the large deformation error, the low quality of the machined surface, the serious damage of the tool, the dynamics changes of the workpiece and the chatter phenomena, are more pronounced in flexible milling systems.

Based on regenerative effects, Budak and Altintas [5] built the chatter prediction model of the milling tool and obtained the two-dimensional SLD that can provide suitable parameters for technicians before machining (See Fig. 1). Bravo et al. [6] applied the relative movement analysis of the subsystems to obtain the stability analysis of flexible system. Eksioglu et al. [7] established the vibration model at tool-workpiece contact zone by introducing mode shapes of both tool and workpiece for each discrete node. Therefore, the dynamic response of tool and workpiece should be considered simultaneously for the flexible system. For the dynamic equation, the delay differential equation of the system is solved mainly with different methods, i.e., frequency domain or time domain [8], [9]. Among former research work, it was worth mentioning that Peng et al. [10] and Friedrich et al. [11] estimated the SLD by using off-line and on-line machine learning method respectively.

In fact, the transfer function in frequency domain is the bridge to solve the equation because it can be transformed into state space in time domain under given conditions. In most

cases, the modal parameters of the dynamic system are required to make the equation concrete. However, the predicted results of the two-dimensional SLD tended to have a certain deviation from the processing results. Except for the prediction precision of different algorithms, this is mainly due to the uncertainty of modal parameters of the system dynamics [12], the simplification of the model and other influences of nonlinear factors [13], [14]. During the interactive process between machine tool and workpiece, multiple modal characteristics would appear [15], which contributes to the uncertainty as well. Hence, it is particularly important to establish accurate prediction models, select appropriate machining parameters and identify machining frequencies to avoid the chatter in flexible system.
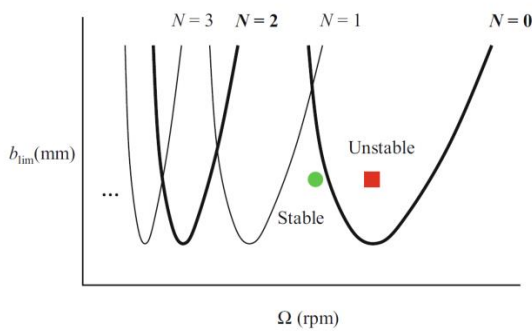
Fig. 1 An illustration for SLD [1]   Fig. 2 Example for material removal simulation [30]
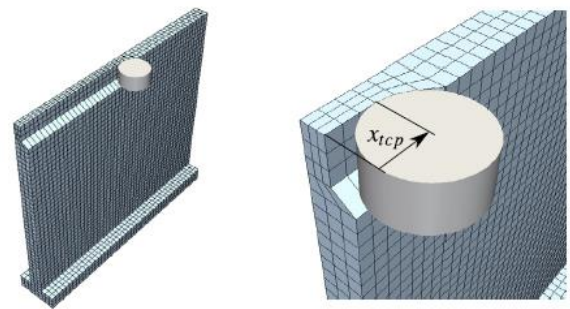
Under the effect of strong milling force, multiple modes of the workpiece would be excited to affect the machined quality. Seguy et al. [15] concluded that the actual chatter frequency was always close to the natural frequency of thin-walled workpiece, and they pointed out that the modes of thin-walled workpiece played a dominant role of the whole system. The challenge is that the machining system may not have only one dominant mode when the possible modes were excited during the machining process [16], [17], [18]. Therefore, the change of the modes makes it difficult to identify the dominant mode of the system, and the modes that do not generate local displacement ought to be eliminated. If all the modes that may be excited were considered into the equations, the efficiency of the SLD would be constrained severely. Zhang et al. [19] considered multiple modes into the dynamic equation by calculating the maximum transfer function values and obtained a conservative two-dimensional SLD. During the machining process, not only the FRF of tool point changes with the spindle speed [20], but also the dynamic response of the IPW will change with the material removal [21]. In the practical cutting process, it is difficult to determine the dynamic response of the in-process tool point FRF. Once the dynamic variation of tool point is considered, it will make the dynamic equation of system more complicated. Therefore, the rotation-free model of spindle has the priority when it comes to the dynamics of the machine-

3

spindle-holder-tool. Since the first few natural frequencies of the thin-walled workpiece are small, these modes are relatively easy to be excited. Thus, it is very significant to determine the real-time dynamic response of the thin-walled workpiece.

For the continuous material removal of workpiece (See Fig. 2), component mode synthesis (CMS) and structural dynamic modification (SDM) are widely used to deal with time-varying dynamics of IPW, which makes it possible to acquire the FRF of the IPW in real-time. Olvera et al. [22] applied the SDM to study the FRF of thin-walled components with compensating mass loading effects of accelerometer. Biermann et al. [23] presented a simulation system considering the finite element (FE) model of turbine blades and material removal effect to study the regenerative chatter during the five-axis machining process. Stepan et al. [24] developed a material removal model with FE method as well and established the SLD along tool positions for turning process, which could avoid chatter effectively. Although Bravo et al. [6] developed a more exact SLD with considering the stage dynamics of both machine and workpiece, to the best of our knowledge, they failed to obtain the dynamics during each stage for material removal. Thevenot et al. [25] used FE model to obtain the modal parameters and identify the dynamic characteristics varying along the tool path, but the dynamics of IPW was unable to be solved and dealt with properly in this way. In order to deal with the dynamics of IPW, Tuysuz et al. [26], [27] and Song et al. [28] adopted reduced-order dynamic substructuring and Sherman-Morrison-Woodbury formula methods respectively to get the modal parameters during the IPW. Dang et al. [29] and Hamann et al. [30] also applied the model order reduction to generate the IPW dynamics. Budak et al. [21] and Yang et al. [31] used SDM, based on FRF database and modal database respectively, to obtain the dynamics of IPW. These methods expanded the way to acquire dynamics during IPW.

1.2.2 Milling force with process damping effect in dynamic analysis

The milling force models are divided into linear models and non-linear models, and the choice of models depends on different purposes. Nonlinear models mainly include different kinds of exponential models and empirical models. Linear cutting force models are widely used because of the advantages in the construction and solution to dynamic equations. From the viewpoint of calculation, the cutting force model is divided into single point model and discrete element model [32], and the difference between the two models is whether the helix angle and mode shape of milling tool are considered into the model or not. The single point model lumps the force to the tool point, which cannot analyze the error along the axial direction. In contrast, the discrete element model can predict the error along the axial direction, but the calculation for the model would become time-consuming.

As shown in Fig. 3, the widely accepted mechanism of the process damping is that the tool flank face intrudes undulations on the machined surface and the indentation volume forms, especially at low spindle speed region, which can consume a part of energy of the chatter and restrain the tool amplitude of vibration [34]. Das and Tobias [35] first studied the process damping, and they introduced the velocity as an additional damping term for the kinetic equation at the low velocity region. Sission and Kegg [36] analyzed the mutual interference between the workpiece and tool, and put forward the corresponding damping force model. Chio and Liang [37] considered the tool wear and developed the SLD with process damping effect. After that, many researchers began to introduce the process damping effects, i.e., process damping force or process damping coefficient, into stability analysis [38], [39], [40]. Molnar et al. [41] investigated the process damping by further reconsidering the velocity-dependent mechanism and gave possible explanations. Recently, Feng et al. [42] expanded the velocity-dependent model [41] and concluded that the velocity-dependent mechanism had more influence on formation of process damping for thin-walled workpiece.
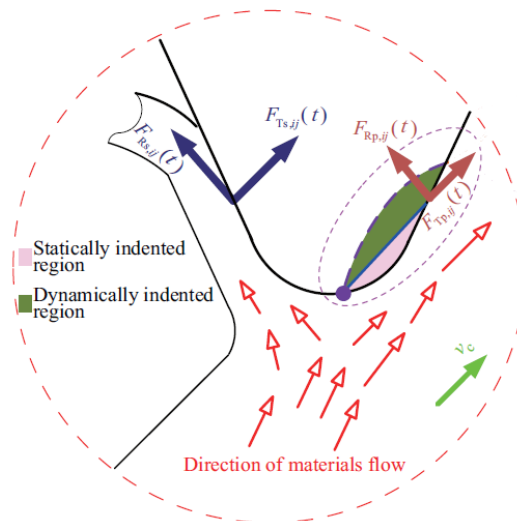
Fig. 3 Generation mechanism of process damping around separation point [33]

Since the regenerative chatter belongs to self-excited vibration, the equivalent damping of the whole machining process system is less than or equal to zero when the chatter occurs. So the system is in the state of negative damping, the vibration amplitude between the milling tool and workpiece will be divergent in this case and may lead the machining process to chaos that different initial states correspond to completely different machining results. For the milling tool, the motion state including the velocity and displacement of the mass point can be represented on the phase plane, and one of its states corresponds to a point on the phase plane. Therefore, the motion of the system can be developed by the trajectory of the points. On the phase plane, an isolated closed phase trajectory is the so-called limit cycle [38], and the corresponding machining system will show self-excited vibration. During the milling process,

different processing parameters can lead to different phase trajectory behaviors. The stable milling process of tool belongs to periodic motion with the limit cycle of the system closed. In unstable case, process damping will suppress part of the disturbances and chatter amplitude with the system phase trajectory converging to the vicinity of limit cycle.

1.2.3 Distribution of SLE during material removal

During the milling process from rough to fine machining, increasing the material removal rate (MRR) is the primary goal. The definition of MRR is

$$MRR = a_e b f_z N \Omega \tag{1.1}$$

where a_e is the radial depth of cut (mm), b is the axial depth of the cut (mm), f_z is the feed per tooth, N is the number of teeth, and Ω is the spindle speed (rpm).

From the viewpoint of MRR, it is better to use high-speed machining under the given condition of feed per tooth and depth of cut. In order to obtain a good machined surface, technicians should not only avoid the occurrence of chatter, but also reduce the machining error [1]. When chatter occurs, the machined surface shows lots of chatter marks and even separates from the milling tool. Accordingly, only under the condition of stable milling, the prediction and control for the machining error would become meaningful.

For the offset error caused by forced vibration at the tool-workpiece contact zone, namely the SLE, it mainly refers to the relative deflection between the tool and the workpiece during the stable milling process, which makes the actual surface deviate from the intended surface (See Fig. 4). Meanwhile, the SLE is an imperative indicator to evaluate machined surface in terms of the accuracy. Although Schmitz [1] and Insperger [44] defined the SLE with different forms, the essence of SLE is the relative dynamic displacement of the tool-workpiece under stable cutting. Like the method for SLD development, the calculation for SLE is well developed with different methods: frequency domain method, temporal finite element analysis, time domain simulation and full discretization method [45], [46], [47], [48], [49]. Schmitz et al. [1], [50], [51] did lots of pioneering and creative research on machining dynamics, and they made a deep study of the distribution of SLE at tool point and along the axial direction (with and without runout). Besides, they studied the whole machining process intensively and simulated the cutting force in time domain with numerical (Euler) iterative algorithm for macro-milling. Based on the optimization criterion of SLE, Kurdi [52] analyzed the selection of robust machining parameters with uncertainties. Ramos [53] applied decision analysis and established a solution model of SLE in frequency domain with considering system dynamics into decision tree. Due to the introduction of uncertainties, the research from

Kurdi [52] and Ramos [53] had higher engineering application in the process of machining parameters optimization. Bachrathy et al. [54] studied the surface properties by surface quality parameters, i.e. surface roughness and SLE, and obtained the function of surface error for helical-edged tool. Eksioglu et al. [7] constructed a model to predict the process states such as cutting forces, vibrations and SLE at discrete-time domain intervals analytically, and the proposed model was validated in down milling. Siebrecht et al. [55] simulated the SLE by developing a constructive solid geometry that visualized SLE as a triangle mesh of the tools. Honeycutt and Schmitz [56] simulated and verified the variation trend about SLE and surface roughness when the machining process was under the conditions of forced vibration and flip bifurcation. Yuan et al. [57] proposed a motion model of arbitrary point on cutter edge by employing harmonic balance method, and predicted the machined surface characteristics such as surface topography, SLE and roughness.
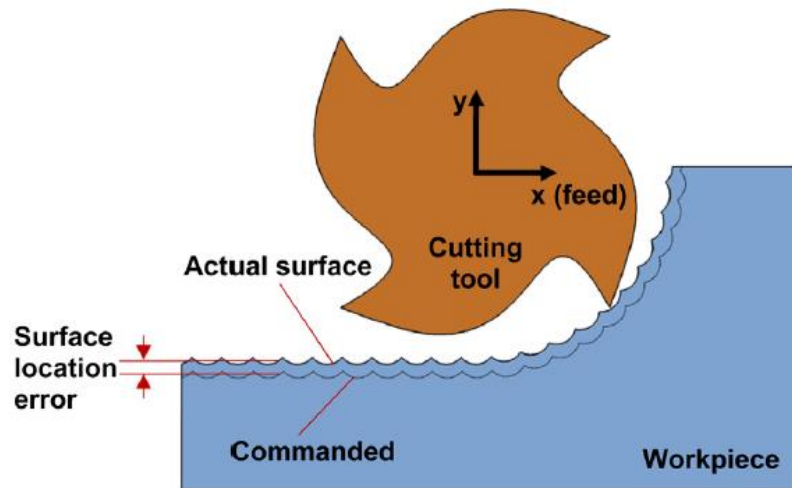
Fig. 4 Illustration about SLE in down milling case [43]

In fact, the expression of SLE is a nonlinear equation that involves many factors, i.e., the spindle speed, instantaneous angular position and so on. Due to the nonlinear characteristics of the SLE, the instability caused by the cumulative effect would occur when the same radial immersion was applied in the continuous milling process. Kiss et al. [58] studied the cumulative effect in SLE firstly, and pointed out the possible instability mode and bistable regions when the machining process experienced continuous radial immersion. Afterwards, Kiss et al. [59] investigated the evaluation of the series of cumulative surface location error (CSLE) in milling operations based on measured frequency response function (FRF) at tool point and proposed an improved stability chart. Li et al. [60] established a prediction model considering both tool stiffness and time-varying stiffness of workpiece with the viewpoint of static deformation, and validated the surface form error of flank milling. Kiran et al. [43] designed a flexure stage and established a two degree of freedoms SLE prediction model with

7

considering dynamics from both milling tool and workpiece. It was worth mentioning that Kiran et al. [43] viewed the dynamic response of the flexure stage in X and Y directions as the dynamics of workpiece. In fact, most researchers put their focus on the dynamic characteristics of tool point to formulate the model of SLE, while the dynamics of workpiece was always ignored. For the workpiece with large stiffness, the dynamic response of tool point would be the main source of SLE. With the material removal, the dynamics of the workpiece cannot continue to be neglected [6], to the best of our knowledge, but few papers studied the prediction of SLE with considering the dynamics of workpiece in continuous material removal.

1.2.4 Dynamic analysis in micro-milling process

The micro-milling machining process is widely applied to the precision engineering techniques and it is the most efficient machining method for forming ideal surface topography [4]. However, the forced vibration and regenerative chatter appearing in the micro-milling process will affect the final processing results, which can lead to larger error and obvious chatter marks. The whole process is an interaction between micro-milling force and dynamic behavior of machine tool, and the transformation between process and machine tool, i.e. the micro-milling force and frequency response function (FRF), determines the final machining quality of the workpiece.
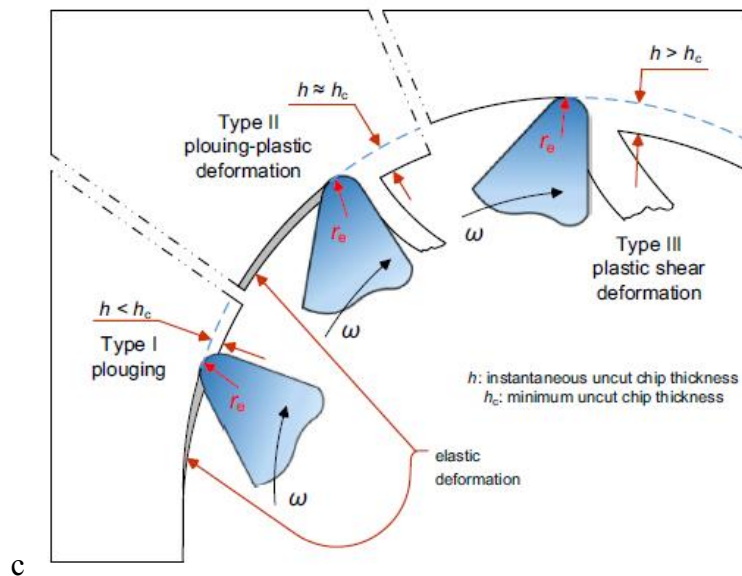
1.2.4.1 Micro-milling force

Fig. 5 Different types for chip thickness in micro-milling [61]

Due to the obvious differences from macro-milling, such as the minimum chip thickness (See Fig. 5), flexible deformation of tool, size effect and effective rake angle, lots of scholars

and researchers have reported on how to develop the micro-milling model and predict the force [62]. Bao and Tansel [63] first proposed a new mechanical cutting force model for micro-end milling operations by taking tool path and the angular delay into account. Malekian et al. [64] studied the mechanism modeling of micro-milling forces with different materials removal types and established the expressions of micro-milling force in corresponding cutting zones. Afazov et al. [65], [66] developed an uncut chip thickness algorithm from the geometric relationship and analyzed the cutting force in micro-milling with finite element method (FEM). Rezaei et al. [67] studied the determination of the minimum uncut chip thickness of micro-end milling tool by experiments and concluded the influences of cutting parameters on the machining process. Boswell et al. [68] concluded the different micro-cutting methods, namely, micro-turning, micro-milling and micro-drilling, and summarized the corresponding phenomena for these machining processes. Chen et al. [61] used time-domain simulation to establish an improved model for micro-milling force including the precise trochoidal trajectory, tool runout and dynamic modulation. However, to the best of our knowledge, the accurate analytical solution to the micro-milling force cannot be obtained because the actual calculation for the instantaneous uncut chip thickness varies with trajectories of different cutting edges. Although the numerical iterative algorithm in time domain may bring a relatively accurate solution to the micro-milling force, it needs many iterations. In addition, it is very difficult to introduce the numerical iterative algorithm into the dynamic equation.

1.2.4.2 Tool-point dynamics determination of micro-milling
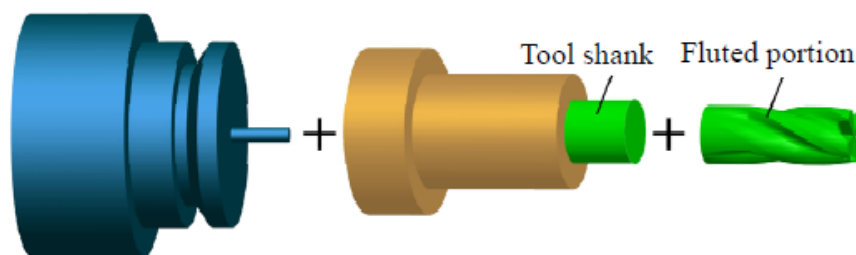
Fig. 6 Example for Receptance coupling assembly [70]

The knowledge of FRFs at the tool point is necessary for micro-milling process. However, the fragile geometry of the micro-milling tool is definitely different from macro-milling tool and it makes experimental modal analysis (EMA) nearly impossible. Receptance coupling substructure analysis (RCSA) was first proposed by Schmitz [69] to overcome these obstacles and predict the assembly FRFs with different coupling styles at the tool point. The basic assembly model of RCSA can be seen in Fig. 6. Based on these work, Schmitz et al. [71], [72]

developed a three-dimensional stability surfaces with variations in macro tool free overhang length and further presented the second generation RCSA for high-speed machining applications. Afterwards Mascardelli and Simon [73] used receptance coupling (RC) method to study the FRF at the micro-milling tool point for multiple substructures and verified that the RC method performed well, even for the tools with a considerably smaller size. Lu et al. [74] also used the RCSA method to obtain the FRFs of micro-milling tool with consideration of rotational degree of freedom. As the individual receptance of substructure mainly depends on the geometric and physical characteristics of tools and holders, the beam theories, such as Euler-Bernoulli beam and Timoshenko beam, are applied to develop the receptance formula. The change of restricted/free overhang length for micro-milling tool will make the FRFs at tool point changed simultaneously. However, the influence of restricted/free overhang length is always ignored and seldom studied in micro-milling when it comes to determine the dynamics at the tool point.

1.2.4.3 SLD and SLE in micro-milling

The modal parameters of the macro-milling system mainly depend on the rigidity of the milling tool or workpiece. For micro-milling tool with small diameter, it is very important to determine the FRF at the tool point, because the stiffness of micro-milling tool is much smaller than that of workpiece [75]. Therefore, the clamping state and the restricted/free overhang length of the tool are very significant, which determines the dynamic machining process.

The SLE of micro-milling process is seldom mentioned in literature. Compared with macro-milling process, micro-milling has smaller machining scale, and the coordinate measurement machine (CMM) used in macro-milling can hardly be applied to the measurement of workpiece in micro-milling [76]. Therefore, the error of micro-milling can only be measured by means of confocal microscope. The chips can be generated smoothly when the instantaneous uncut thickness is greater than the minimum chip thickness. However, when chips are detached from the workpiece, the burrs also cause inconvenience for measurement. Even if the burrs are removed by ultrasonic vibration device, the notches left by the burr roots on the surface of the workpiece will still affect the final measurement. Since the diameter of the micro-milling tool is from 25 μm to 1000 μm, the radial depth of cut is small [4]. Therefore, even under stable cutting condition, the machining error caused by the forced vibration is small as well. In addition to the SLE, there are many factors affecting the machining process, such as tool wear, tool runout, burrs, roughness and measurement errors,

so it is difficult to separate the SLE from the above errors. Only in the case of ignoring part of some factors, experimental exploration can be carried out for SLE.

1.2.5 Uncertainty--challenge in machining process

As shown in Figs. 7 and 8, the SLD of milling process is not accurate. Since different modes correspond to different SLDs, the construction of the SLD depends on the excited modes of the machining system. The first mode is always adopted to establish the SLD, because it usually corresponds to a smaller critical limit depth of cut. In fact, it is unpredictable which modes are excited during the machining process, so the selection of modal parameters is uncertain.

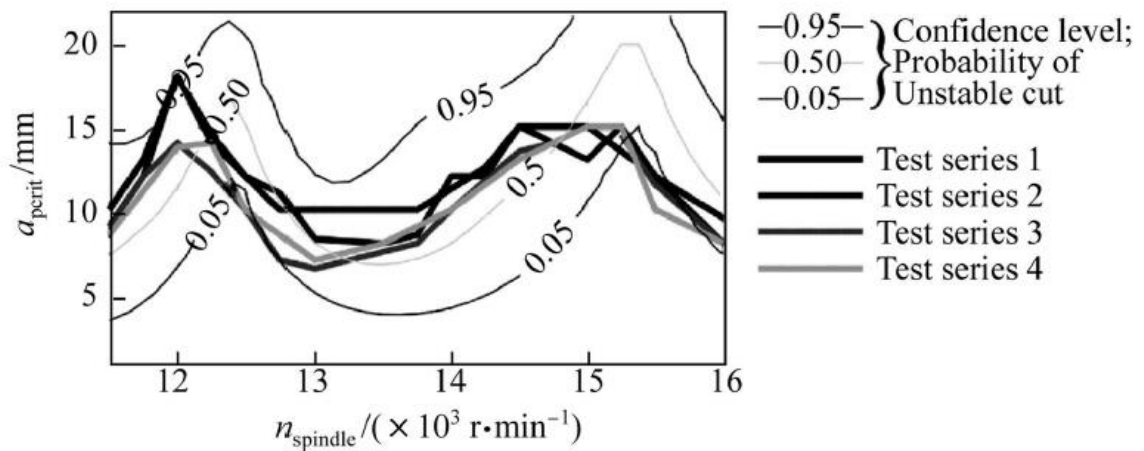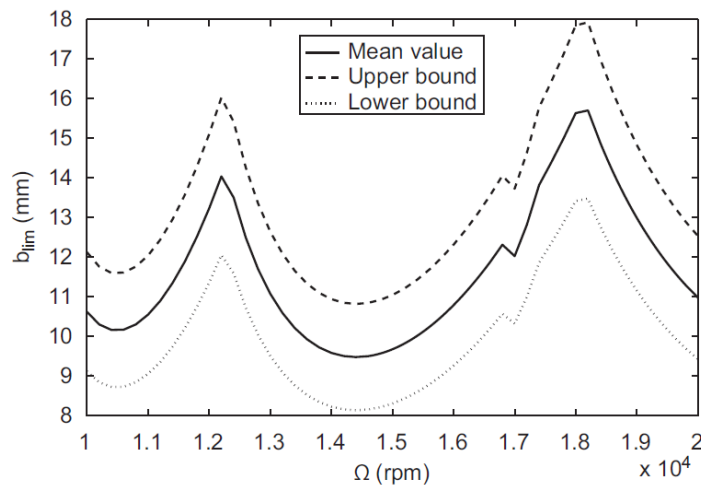Fig. 7 Illustration for SLD with different confidence levels [12]

Fig. 8 Upper and lower boundary of SLD due to uncertainties [77]

In addition, the unstable islands caused by helix angle and bifurcation, time-varying modal parameters during machining process, process damping, direct and cross responses of milling tool, the variation of cut-in and cut-out angles, tool runout and mode transfer of system will

change the boundary of SLD as well [78], [79], [80], [81], [82], [83]. Therefore, it is nearly impossible to obtain ideal SLDs during complex machine-workpiece interaction.

1.3 Current main problems

In both macro and micro milling, stable machining parameters are prerequisites for the prediction of cutting forces and machining errors; once machining process is unstable, any analysis will be meaningless. It is therefore essential to determine a realistic SLD. For milling process, it consists of three main steps: a method for solving the dynamic equation, determination of the modal parameters and extension of the system dynamics model for different machining situations.

Milling stability analysis involves the solution to kinetic equations. Because the interpolation methods of state term and delayed term in dynamic equation determine the convergence and accuracy of the algorithm. Therefore, apart from the existing prediction methods, new stability solution methods need to be further developed and upgraded.

The dynamic response of a macro-milling tool can be identified by dynamic tests, and the dynamics of the workpiece can be obtained by experimental measurements or simulation as well. However, as the material is removed, the dynamic response of the workpiece changes. It is important to obtain a fast and accurate dynamics of IPW when the modes of the workpiece dominate the whole machining process.

However, the existing methods have some disadvantages in mass and stiffness variation matrix assembly, as well as node determination. For example, the material to be removed cannot be easily obtained and the nearest node cannot be identified either, which brings practical difficulties. Therefore, the models of IPW dynamics determination are still immature and need to be further explored.

In macro milling process, there are two main situations where the dynamics of workpiece changes significantly:

Case I. Thin-walled workpiece is machined with material removal;

Case II. General workpiece is continuously machined with relatively much material removal (thickness from thick to thin).

These are by far the two most important and common difficult points during machining process:

1. In the first case, there is still a lack of a rigorous analysis framework for how to integrate process forces and dynamic response of workpiece-tool in a flexible machining system.

2. In the first case, it is also unclear how to establish a robust SLD that has application value.

3. In the second case, it is not clear how to determine the stable machining parameters for

cumulative cutting process.

4. In the second case, there is a lack of method to develop the SLD of continuous cutting in combination with accumulated SLE.

For the micro milling process, the micro-milling tool is less rigid than the workpiece due to the small geometry of the tool and less amount of material removal. Accordingly, the dynamic response of the system is focused on the determination of the dynamics of the micro-milling tool point, which depends on the geometry of the tool, the cross-sectional shape and the restricted/free overhang length. Therefore, there are mainly two machining difficulties in micro-milling process:

5. How to determine a robust SLD and SLE in such a small machining scale is difficult for technicians.

6. Whether the restricted/free overhang length has an effect on the determination of stability and dynamic errors needs to be analyzed in conjunction with the forces of the machining process, the dynamic tests and other phenomena in the experiment (burrs, vibrations).

2 Methodology of the dissertation

As seen in the previous chapter, the process of predicting both SLD and SLE involves the solution to the dynamic equations. The dynamic equations are time-delay differential equations, which are more complex to obtain the solutions. This chapter introduces the deductive process of the updated third-order full discretization method in detail. Besides, the current popular data prediction method, machine learning prediction method based on SVM, is introduced as well.

2.1 Method for stability prediction

2.1.1 Third-order updated full-discretization

Compared with the stability prediction in frequency domain, the time domain method, especially the full-discretization method, has been widely used because of its high prediction accuracy and clear calculation steps. The full-discretization method has definite stability criteria, which can determine whether the eigenvalues corresponding to the spindle speed and depth of cut are stable or not. Meanwhile, the full-discretization method can predict the SLD and SLE synchronously. Since the full-discretization method can further improve the computational efficiency, the follow-up improvements of this method are mainly focused on the approximation of the state term and delayed term in the delay differential equation. Then the updated third-order full discretization method is proposed, which has a high convergence rate [9]. In Chapter 4 and 5, based on the mode shape extracted from workpiece, dynamic solution and Matlab programming will be carried out by applying the updated third-order full discretization method. Now, the updated third-order full-discretization method is introduced in details.

In order to simplify the calculation process, the single degree of freedom milling model is developed. The time periodic delay-differential equation with regenerative effect can be written as [84]

$$\ddot{x}(t) + 2\zeta\omega_r\dot{x}(t) + \omega_r^2 x(t) = -\frac{bh(t)}{m}(x(t) - x(t-\tau))$$

(2.1)

where ζ is the damping ratio, ω_r is the natural frequency, b is the axial depth of cut, m is the modal mass, $x(t)$ is the displacement in the current period, $x(t-\tau)$ is the displacement in the previous period, the time delay τ is equal to the tooth passing period T.

The instantaneous uncut chip thickness $h(t)$ is defined as

$$h(t) = \sum_{j=1}^{N} g\left[\phi_j(t)\right] \sin((\phi_j(t))[K_t \cos(\phi_j(t)) + K_r \sin(\phi_j(t))]$$
(2.2)

where K_t, K_r are the tangential and the normal cutting force coefficients respectively, N is the number of cutter teeth.

The angular position for the jth tooth is written as

$$\phi_j(t) = (2\pi\Omega / 60)t + (j-1)2\pi / N$$
(2.3)

where Ω (rpm) is the spindle speed.

$g(\phi_j(t))$ is the unit step function which identifies whether the jth tooth is in cut or not:

$$g(\phi_j) = \begin{cases} 1 & \text{if } \phi_s \leq \phi_j \leq \phi_e \\ 0 & \text{if } \phi_j < \phi_s \text{ or } \phi_j > \phi_e \end{cases}$$
(2.4)

with

$$\begin{cases} \phi_s = \arccos(2a_e/D-1) \\ \phi_e = \pi \end{cases}, \text{down milling}, \quad \begin{cases} \phi_s = 0 \\ \phi_e = \arccos(1-2a_e/D) \end{cases}, \text{up milling}$$

where ϕ_s and ϕ_e are start angle and exit angle respectively, which describe the tool enters and exits the workpiece; D is the diameter of the milling tool.

By using the transformation $\mathbf{x}(t) = \begin{bmatrix} x(t) \\ m\dot{x}(t) + m\zeta\omega_r x(t) \end{bmatrix}$, Eq. (2.1) can be developed in the state space as

$$\dot{\mathbf{x}}(t) = \mathbf{A}_0\mathbf{x}(t) + \mathbf{B}(t)\mathbf{x}(t) - \mathbf{B}(t)\mathbf{x}(t-\tau)$$
(2.5)

where $\mathbf{A}_0 = \begin{bmatrix} -\zeta\omega_r & \dfrac{1}{m} \\ m(\zeta\omega_r)^2 - m\omega_r^2 & -\zeta\omega_r \end{bmatrix}$ is a constant matrix, $\mathbf{B}(t) = \begin{bmatrix} 0 & 0 \\ -bh(t) & 0 \end{bmatrix}$ is a periodic-coefficient matrix with $\mathbf{B}(t) = \mathbf{B}(t+T)$.

Here, the direct integration scheme is employed to solve Eq. (2.5). Firstly, the period T is divided into n equal time intervals with the length of h, that is $T = nh$, where n is an integer. Eq. (2.5) is integrated on the ith small time interval $[ih, (i+1)h]$, and it becomes

$$\mathbf{x}(t) = e^{\mathbf{A}_0(t-ih)}\mathbf{x}(ih) + \int_{ih}^{t} e^{\mathbf{A}_0(t-s)}\mathbf{B}(s)[\mathbf{x}(s) - \mathbf{x}(s-T)]ds$$
(2.6)

Eq. (2.6) can be equivalently arranged as [85]

$$\mathbf{x}(ih+h) = e^{\mathbf{A}_0 h}\mathbf{x}(ih) + \int_0^h e^{\mathbf{A}_0 s}[\mathbf{B}(ih+h-s)[\mathbf{x}(ih+h-s) - \mathbf{x}(ih+h-s-T)]ds \tag{2.7}$$

The state term $\mathbf{x}(ih+h-s)$ and delayed term $\mathbf{x}(ih+h-s-T)$ in Eq. (2.7) are interpolated by third-order Newton interpolation polynomial. The node values $\mathbf{x}(ih-2h)$, $\mathbf{x}(ih-h)$, $\mathbf{x}(ih)$ and $\mathbf{x}(ih+h)$ denoted as $\mathbf{X}_{i-2}$, $\mathbf{X}_{i-1}$, $\mathbf{X}_i$ and $\mathbf{X}_{i+1}$ respectively, are applied to interpolate $\mathbf{x}(ih+h-s)$. The node values $\mathbf{x}(ih-T)$, $\mathbf{x}(ih+h-T)$, $\mathbf{x}(ih+2h-T)$ and $\mathbf{x}(ih+3h-T)$ written as $\mathbf{X}_{i-n}$, $\mathbf{X}_{i-n+1}$, $\mathbf{X}_{i-n+2}$ and $\mathbf{X}_{i-n+3}$ respectively, are employed to interpolate $\mathbf{x}(ih+h-s-T)$. Compared with high-order interpolation of $\mathbf{x}(ih+h-s)$ and $\mathbf{x}(ih+h-s-T)$, the high-order interpolation of periodic-coefficient matrix $\mathbf{B}(ih+h-s)$ has no obvious effects on calculation efficiency according to the research of Tang [86]. Therefore, $\mathbf{B}(ih+h-s)$ is interpolated by first-order Newton polynomial $\mathbf{B}(ih)$ and $\mathbf{B}(ih+h)$ which denote as $\mathbf{B}_i$ and $\mathbf{B}_{i+1}$ respectively.

The state term $\mathbf{x}(ih+h-s)$ can be expressed by third-order Newton interpolation method:

$$\mathbf{x}(ih+h-s) \approx a_1\mathbf{x}_{i-2} + b_1\mathbf{x}_{i-1} + c_1\mathbf{x}_i + d_1\mathbf{x}_{i+1} \tag{2.8}$$

where

$$a_1 = \frac{s}{3h} - \frac{s^2}{2h^2} + \frac{s^3}{6h^3}, \ b_1 = \frac{-3s}{2h} + \frac{2s^2}{h^2} - \frac{s^3}{2h^3}, \ c_1 = \frac{3s}{h} - \frac{5s^2}{2h^2} + \frac{s^3}{2h^3}, \ d_1 = 1 - \frac{11s}{6h} + \frac{s^2}{h^2} - \frac{s^3}{6h^3} \tag{2.9}$$

The delayed term $\mathbf{x}(ih+h-s-T)$ is developed by third-order Newton interpolation method as well

$$\mathbf{x}(ih+h-s-T) \approx a_2\mathbf{x}_{i-n} + b_2\mathbf{x}_{i-n+1} + c_2\mathbf{x}_{i-n+2} + d_2\mathbf{x}_{i+n+3} \tag{2.10}$$

where

$$a_2 = \frac{s}{3h} + \frac{s^2}{2h^2} + \frac{s^3}{6h^3}, \ b_2 = 1 + \frac{s}{2h} - \frac{s^2}{h^2} - \frac{s^3}{2h^3}, \ c_2 = \frac{-s}{h} + \frac{s^2}{2h^2} + \frac{s^3}{2h^3}, \ d_2 = \frac{s}{6h} - \frac{s^3}{6h^3} \tag{2.11}$$

Then, the periodic-coefficient matrix $\mathbf{B}(ih+h-s)$ is interpolated by first-order Newton interpolation [87]

$$\mathbf{B}(ih+h-s) \approx \mathbf{B}_{i+1} + \frac{(\mathbf{B}_i - \mathbf{B}_{i+1})s}{h} \tag{2.12}$$

Substituting Eqs. (2.8-2.12) into Eq. (2.7) yields

$$\mathbf{x}_{i+1} = \mathbf{P}_i \begin{bmatrix} (\mathbf{F}_0 + \mathbf{M}_{11}^i)\mathbf{x}_i + \mathbf{M}_{12}^i \mathbf{x}_{i-1} + \mathbf{M}_{13}^i \mathbf{x}_{i-2} \\ + \mathbf{M}_{1,(n+1)}^i \mathbf{x}_{i-n} + \mathbf{M}_{1,n}^i \mathbf{x}_{i-n+1} + \mathbf{M}_{1,(n-1)}^i \mathbf{x}_{i-n+2} \\ + \mathbf{M}_{1,(n-2)}^i \mathbf{x}_{i-n+3} \end{bmatrix} \tag{2.13}$$

where

$$\mathbf{P}_i = \left[\mathbf{I} - \mathbf{M}_{i,c} \right]^{-1} \tag{2.14}$$

$$\mathbf{M}_{11}^i = \left(\frac{3\mathbf{F}_2}{h} - \frac{11\mathbf{F}_3}{2h^2} + \frac{3\mathbf{F}_4}{h^3} - \frac{\mathbf{F}_5}{2h^4} \right)\mathbf{B}_{i+1} + \left(\frac{3\mathbf{F}_3}{h^2} - \frac{5\mathbf{F}_4}{2h^3} + \frac{\mathbf{F}_5}{2h^4} \right)\mathbf{B}_i \tag{2.15}$$

$$\mathbf{M}_{12}^i = \left(\frac{-3\mathbf{F}_2}{2h} + \frac{7\mathbf{F}_3}{2h^2} - \frac{5\mathbf{F}_4}{2h^3} + \frac{\mathbf{F}_5}{2h^4} \right)\mathbf{B}_{i+1} + \left(\frac{-3\mathbf{F}_3}{2h^2} + \frac{2\mathbf{F}_4}{h^3} - \frac{\mathbf{F}_5}{2h^4} \right)\mathbf{B}_i \tag{2.16}$$

$$\mathbf{M}_{13}^i = \left(\frac{\mathbf{F}_2}{3h} - \frac{5\mathbf{F}_3}{6h^2} + \frac{2\mathbf{F}_4}{3h^3} - \frac{\mathbf{F}_5}{6h^4} \right)\mathbf{B}_{i+1} + \left(\frac{\mathbf{F}_3}{3h^2} - \frac{\mathbf{F}_4}{2h^3} + \frac{\mathbf{F}_5}{6h^4} \right)\mathbf{B}_i \tag{2.17}$$

$$\mathbf{M}_{i,c} = \left(\mathbf{F}_1 - \frac{17\mathbf{F}_2}{6h} + \frac{17\mathbf{F}_3}{6h^2} - \frac{7\mathbf{F}_4}{6h^3} + \frac{\mathbf{F}_5}{6h^4} \right)\mathbf{B}_{i+1} + \left(\frac{\mathbf{F}_2}{h} - \frac{11\mathbf{F}_3}{6h^2} + \frac{\mathbf{F}_4}{h^3} - \frac{\mathbf{F}_5}{6h^4} \right)\mathbf{B}_i \tag{2.18}$$

$$\mathbf{M}_{1,(n-2)}^i = \left(\frac{\mathbf{F}_2}{6h} - \frac{\mathbf{F}_3}{6h^2} - \frac{\mathbf{F}_4}{6h^3} + \frac{\mathbf{F}_5}{6h^4} \right)\mathbf{B}_{i+1} + \left(\frac{\mathbf{F}_3}{6h^2} - \frac{\mathbf{F}_5}{6h^4} \right)\mathbf{B}_i \tag{2.19}$$

$$\mathbf{M}_{1,(n-1)}^i = \left(\frac{-\mathbf{F}_2}{h} + \frac{3\mathbf{F}_3}{2h^2} - \frac{\mathbf{F}_5}{2h^4} \right)\mathbf{B}_{i+1} + \left(\frac{-\mathbf{F}_3}{h^2} + \frac{\mathbf{F}_4}{2h^3} + \frac{\mathbf{F}_5}{2h^4} \right)\mathbf{B}_i \tag{2.20}$$

$$\mathbf{M}_{1,n}^i = \left(\mathbf{F}_1 - \frac{\mathbf{F}_2}{2h} - \frac{3\mathbf{F}_3}{2h^2} + \frac{\mathbf{F}_4}{2h^3} + \frac{\mathbf{F}_5}{2h^4} \right)\mathbf{B}_{i+1} + \left(\frac{\mathbf{F}_2}{h} + \frac{\mathbf{F}_3}{2h^2} - \frac{\mathbf{F}_4}{h^3} - \frac{\mathbf{F}_5}{2h^4} \right)\mathbf{B}_i \tag{2.21}$$

$$\mathbf{M}_{1,(n+1)}^i = \left(\frac{\mathbf{F}_2}{3h} + \frac{\mathbf{F}_3}{6h^2} - \frac{\mathbf{F}_4}{3h^3} - \frac{\mathbf{F}_5}{6h^4} \right)\mathbf{B}_{i+1} + \left(\frac{\mathbf{F}_3}{3h^2} + \frac{\mathbf{F}_4}{2h^3} + \frac{\mathbf{F}_5}{6h^4} \right)\mathbf{B}_i \tag{2.22}$$

$\mathbf{F}_0$ - $\mathbf{F}_5$ can be expressed by the following relations

$$\mathbf{F}_0 = e^{A_0 h} \tag{2.23}$$

$$\mathbf{F}_1 = \mathbf{A}_0^{-1}(\mathbf{F}_0 - \mathbf{I}) \tag{2.24}$$

$$\mathbf{F}_2 = \mathbf{A}_0^{-1}(h\mathbf{F}_0 - \mathbf{F}_1) \tag{2.25}$$

$$\mathbf{F}_3 = \mathbf{A}_0^{-1}(h^2\mathbf{F}_0 - 2\mathbf{F}_2) \tag{2.26}$$

$$\mathbf{F}_4 = \mathbf{A}_0^{-1}(h^3\mathbf{F}_0 - 3\mathbf{F}_3) \tag{2.27}$$

$$\mathbf{F}_5 = \mathbf{A}_0^{-1}(h^4\mathbf{F}_0 - 4\mathbf{F}_4) \tag{2.28}$$

In Eq. (2.13), $\mathbf{x}_{i-2}$, $\mathbf{x}_{i-1}$, $\mathbf{x}_i$ and $\mathbf{x}_{i+1}$ are the dynamic responses in the current period, and $\mathbf{x}_{i-n}$, $\mathbf{x}_{i-n+1}$, $\mathbf{x}_{i-n+2}$ and $\mathbf{x}_{i-n+3}$ are the dynamic responses in the previous period. It is noted that the number of the node values used for interpolating x(ih+h−s) and x(ih+h−s−T) should be the same so that the one-to-one discrete mapping relation between current period and the previous period can be established. During the calculation process, all the variables '$\mathbf{x}$' should be in two adjacent periods: current period and previous period. If some of the variables '$\mathbf{x}$' are located out of the range of the current and immediate previous period, the corresponding substitutions should be applied to convert them into required range.

Combining Eq. (2.13) and Eqs. (2.14-2.28), the discrete mapping relation between current period and the immediate previous period is developed as

$$
\begin{Bmatrix} \mathbf{x}_{i+1} \\ \mathbf{x}_i \\ \mathbf{x}_{i-1} \\ \mathbf{x}_{i-2} \\ \vdots \\ \mathbf{x}_{i-n+4} \\ \mathbf{x}_{i-n+3} \\ \mathbf{x}_{i-n+2} \\ \mathbf{x}_{i-n+1} \end{Bmatrix} = \begin{bmatrix} \mathbf{M}_{11}^i & \mathbf{M}_{12}^i & \mathbf{M}_{13}^i & 0 & \cdots & \mathbf{M}_{1,(n-2)}^i & \mathbf{M}_{1,(n-1)}^i & \mathbf{M}_{1,n}^i & \mathbf{M}_{1,(n+1)}^i \\ \mathbf{I} & 0 & 0 & 0 & \cdots & 0 & 0 & 0 & 0 \\ 0 & \mathbf{I} & 0 & 0 & \cdots & 0 & 0 & 0 & 0 \\ 0 & 0 & \mathbf{I} & 0 & \cdots & 0 & 0 & 0 & 0 \\ 0 & 0 & 0 & \mathbf{I} & \cdots & 0 & 0 & 0 & 0 \\ \vdots & \vdots & \vdots & \vdots & \ddots & 0 & 0 & 0 & 0 \\ 0 & 0 & 0 & 0 & \cdots & \mathbf{I} & 0 & 0 & 0 \\ 0 & 0 & 0 & 0 & \cdots & 0 & \mathbf{I} & 0 & 0 \\ 0 & 0 & 0 & 0 & \cdots & 0 & 0 & \mathbf{I} & 0 \end{bmatrix} \begin{Bmatrix} \mathbf{x}_i \\ \mathbf{x}_{i-1} \\ \mathbf{x}_{i-2} \\ \mathbf{x}_{i-3} \\ \vdots \\ \mathbf{x}_{i-n+3} \\ \mathbf{x}_{i-n+2} \\ \mathbf{x}_{i-n+1} \\ \mathbf{x}_{i-n} \end{Bmatrix} \qquad (2.29)
$$

Then the state transition matrix Φ for the dynamic system over one period T is written as

$$\Phi = \mathbf{M}_n \mathbf{M}_{n-1} \cdots \mathbf{M}_1 \qquad (2.30)$$

where
$$
\mathbf{M}_i = \begin{bmatrix} \mathbf{M}_{11}^i & \mathbf{M}_{12}^i & \mathbf{M}_{13}^i & 0 & \cdots & \mathbf{M}_{1,(n-2)}^i & \mathbf{M}_{1,(n-1)}^i & \mathbf{M}_{1,n}^i & \mathbf{M}_{1,(n+1)}^i \\ \mathbf{I} & 0 & 0 & 0 & \cdots & 0 & 0 & 0 & 0 \\ 0 & \mathbf{I} & 0 & 0 & \cdots & 0 & 0 & 0 & 0 \\ 0 & 0 & \mathbf{I} & 0 & \cdots & 0 & 0 & 0 & 0 \\ 0 & 0 & 0 & \mathbf{I} & \cdots & 0 & 0 & 0 & 0 \\ \vdots & \vdots & \vdots & \vdots & \ddots & 0 & 0 & 0 & 0 \\ 0 & 0 & 0 & 0 & \cdots & \mathbf{I} & 0 & 0 & 0 \\ 0 & 0 & 0 & 0 & \cdots & 0 & \mathbf{I} & 0 & 0 \\ 0 & 0 & 0 & 0 & \cdots & 0 & 0 & \mathbf{I} & 0 \end{bmatrix}, \quad (i = 1, 2, \cdots, n)
$$

Then, the Floquet theory can be implemented to determine the stability of the dynamic system with the decision criterion:

$$\max(|\lambda(\Phi)|) \begin{cases} <1 & \text{stable} \\ =1 & \text{critical stable} \\ >1 & \text{unstable} \end{cases} \qquad (2.31)$$

2.1.2 Machine learning method

Machine learning, as a branch of computer science, is widely used in graphics, network communication and even chip design, and it also provides technical supports for many interdisciplinary disciplines [88]. The core of machine learning is to train the known samples by using certain algorithms so that a stable learner, which will be used for judging the unknown samples, can be constructed. For the workpiece with large stiffness, the flow chart for stability determination is illustrated in Fig. 9.
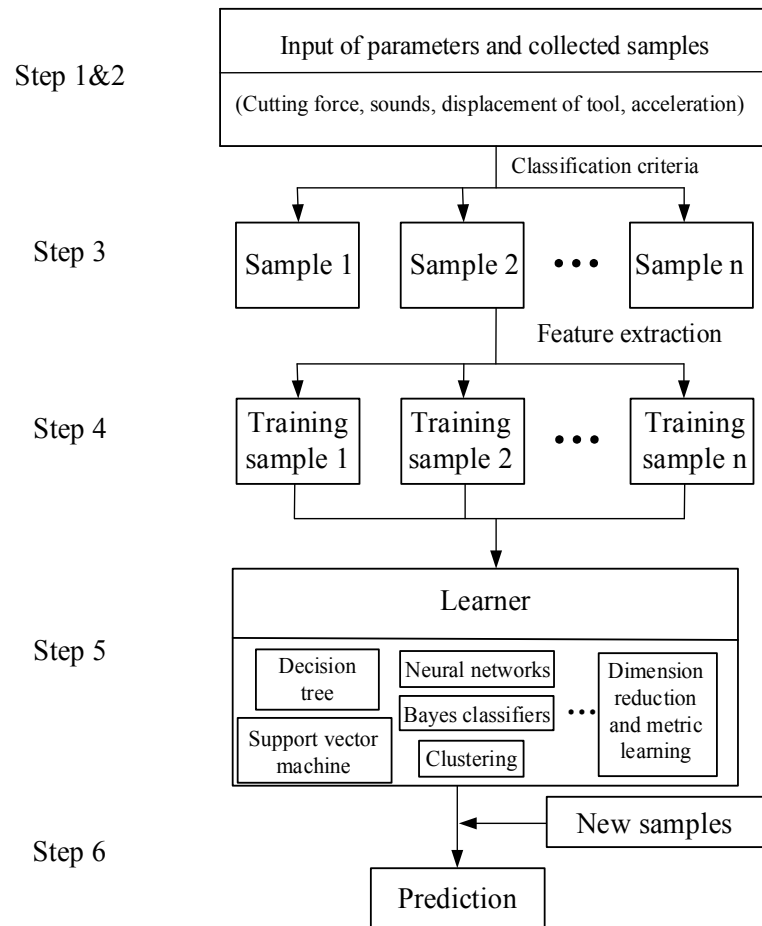
Step 1&2 — Input of parameters and collected samples

(Cutting force, sounds, displacement of tool, acceleration)

Classification criteria

Step 3 — Sample 1 | Sample 2 | • • • | Sample n

Feature extraction

Step 4 — Training sample 1 | Training sample 2 | • • • | Training sample n

Learner

Step 5 — Decision tree | Neural networks | Dimension reduction and metric learning | Bayes classifiers | • • • | Support vector machine | Clustering

New samples

Step 6 — Prediction

Fig. 9 Procedure for SLD establishment with machine learning

The prediction of two-dimensional SLD can be summarized as follows

Step 1. Input some basic parameters of milling tool, such as tool overhang length, number of teeth, helix angle and radial immersion.

Step 2. Collect the milling signals during the machining process, such as milling force, sound, acceleration and displacement of tool point.

Step 3. Divide the collected signals into sample 1 (unstable signal) and sample 2 (stable signal) according to the criteria of chatter occurrence.

Step 4. Extract the key features from sample 1 and sample 2 as training sample 1 and training sample 2.

Step 5. Select machine learning algorithm to build a relative robust learner.

Step 6. Predict new unknown samples with the learner

The second and third step mainly depend on multiple sensors to classify the collected machining signals [89] [90], and the fourth step mainly uses time domain, frequency domain or time-frequency domain methods to extract features [91] [92]. All the above three steps are described by specific methods in the literature, which will not be repeated any more. Thus, the third updated full-discretization method is applied to develop the SLD, and two kinds of different machining parameters are obtained, namely, the stable samples and unstable samples. Then the training samples can be selected from these samples.

Support Vector Machine (SVM) is widely used because of its strong generalization ability and developed software package. Here, the 'fitcsvm' function from Matlab is employed to establish the learner. As shown in Fig. 10, the distance between two different samples of support vector and hyperplane is margin. The hyperplane is used to separate samples of different categories, and the basis of hyperplane determination is to maximize the margin. Therefore, the SVM defines as [88]：

$$\begin{cases} \min\limits_{w,\,b_s} \dfrac{1}{2}\|w\|^2 \\ \text{s.t. } y_i(w^{\mathrm{T}}x_i + b_s) \geq 1,\ i = 1,2,... \end{cases} \tag{2.32}$$

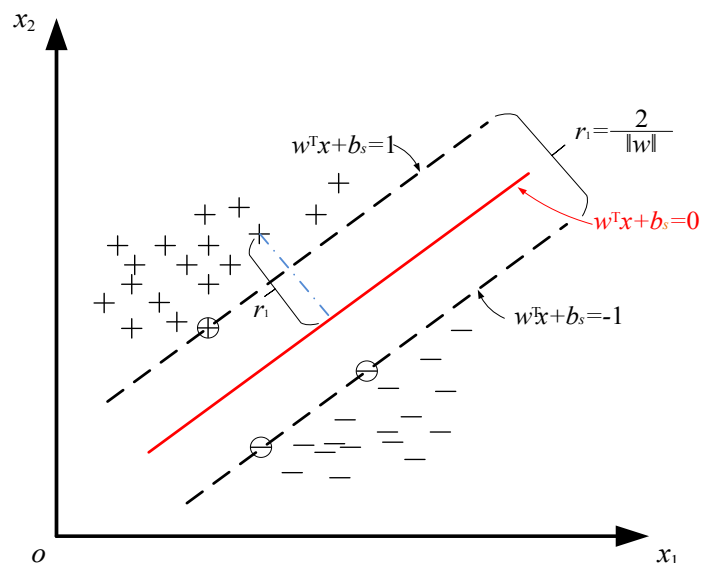where $(w,\,b_s)$ is the normal vector and displacement of hyperplane respectively

Fig. 10 Theory about Support Vector Machine [88]

2.1.2.1 Case study for machine learning

Prior to applying the machine learning method, as shown in Tab. 1 and 2, the geometric and modal parameters of the milling tool are needed.

Table 1 Parameters input of milling tool

Number of tooth	Diameter of tool	Helix angle	Cutting force coefficients in tangential direction	Cutting force coefficients in radial direction
4	10 mm	30°	8.9×10^8 Pa	2.4×10^8 Pa

Table 2 Modal parameters of the machine-spindle-milling tool

Mode	Natural frequency	Modal stiffness	Damping ratio (%)
First mode	3122 Hz	1.2601×10^7 N/m	2.5
Second mode	3873 Hz	2.7412×10^7 N/m	2.1

Based on the above parameters, the updated third-order full discretization method was used to construct the SLD. Then the points in the SLD were divided into the stable parameters and unstable parameters according to the judgement criteria, as shown in Fig. 11. In practical machining process, this procedure corresponds to steps 2 and 3.
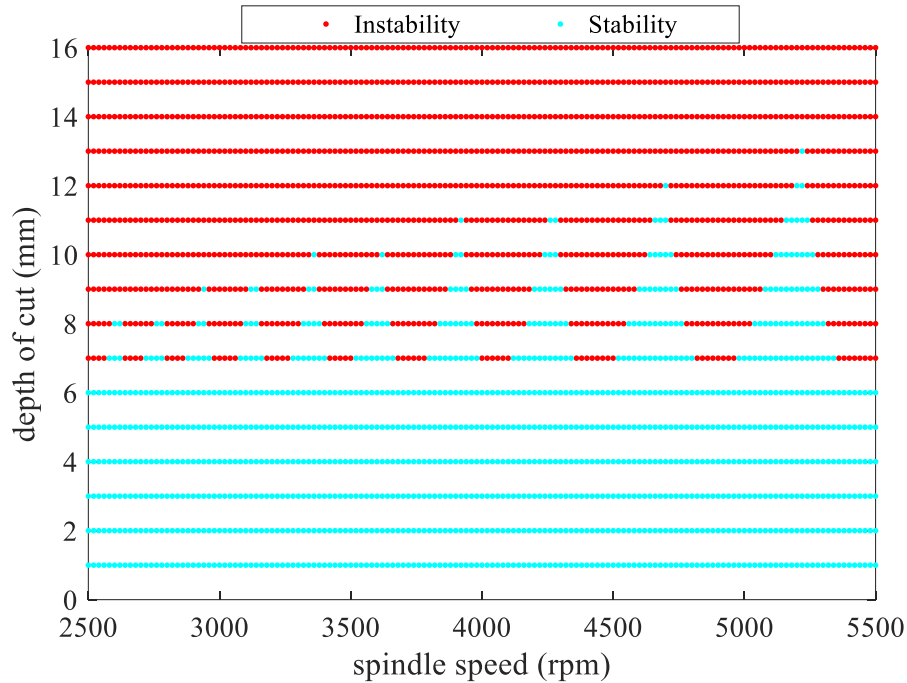

Fig. 11 Discretization points of the SLD

As illustrated in Fig. 12, some stable parameters and unstable parameters are selected as training samples.
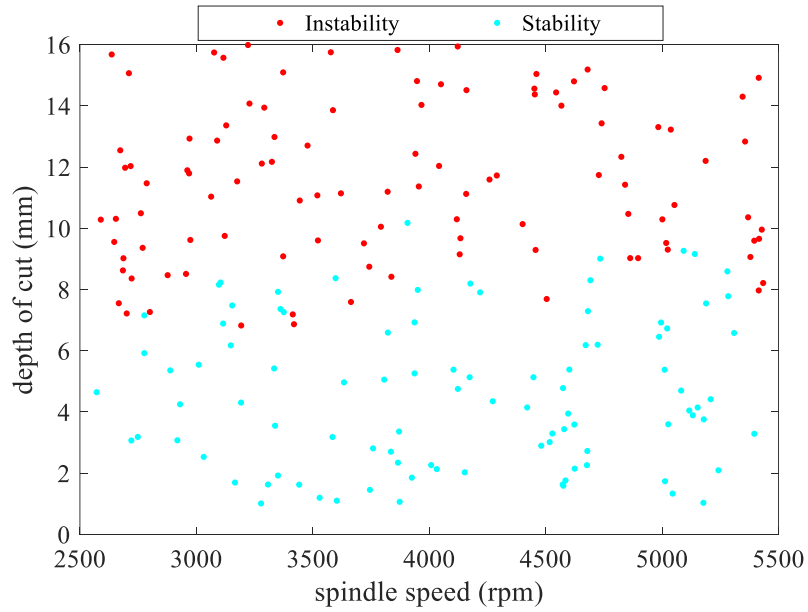
Fig. 12 Random points applied for the upcoming SLD prediction

Finally, the samples are trained and the decision boundary predicted by iterative data is obtained with the algorithm of SVM, as shown in Fig. 13.
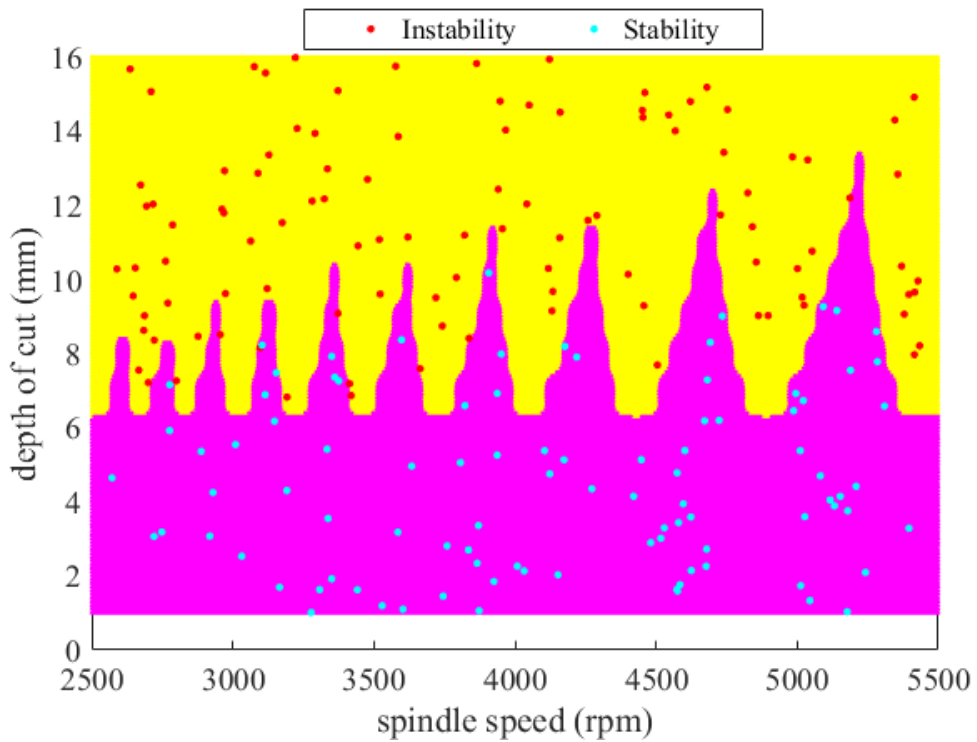

Fig. 13 Prediction of SLD with machine learning method

Compared with the predicted results of the two methods, the results match well with each other. As the machine learning method is mainly based on selected samples, this method is more adaptable to specific machining schemes when there are enough training samples. Besides, uncertain factors have been included in the sample collection process, so the machine learning method has a higher practical application as well.

22

2.2 Research questions and structures

The stability and dynamic error are significant questions for both macro-milling scale and micro-milling scale. In order to answer the questions, the hypothesis is formulated. That is, in a framework based on regenerative chatter, the realistic SLDs and SLEs for both macro-milling and micro-milling process can be predicted and analyzed by using stability prediction method in combination with different machining scenarios.

In terms of macro-milling process, the analysis is focused on the stability and variation of dynamic errors due to the dynamics change of the workpiece. In terms of micro-milling process, the main analysis is the frequency response of the micro-milling tool and the effect of burrs. The above two questions will be further studied from the aspects of process force and dynamic response.

For macro-milling process, how could the change in stiffness and mass matrix quickly be determined and assembled during material removal? What other aspects need to be considered for a reliable and practical prediction of the SLD/SLE with third-order updated full-discretization method? (Case I and Case II)

For micro-milling process, how could the SLD/SLE be established in the small machining scale? What are the main obstacles that are different from macro-milling situations? What is the main factor affecting the SLD/SLE?

Therefore, the dissertation starts from these following aspects: algorithm for stability prediction, establishment of IPW dynamics, characteristics of the instability behavior, and prediction of dynamic SLE for macro-milling and micro-milling respectively. Then the scientific problems about dynamic behaviors evolution and the mapping relationship between milling process and machine tool are expounded in theory. Through the research of these topics, the dynamic behavior of machining system will be deeply grasped, which will provide theoretical guidance and experimental basis for machining stability, error compensation and control of SLE for both macro-milling and micro-milling scale. As shown in Fig. 14, the dissertation is organized as follows:

Chapter 1 presented the research background, scientific significance, the state of the art associated with dynamic analysis for macro-milling and micro-milling, and the current main problems.

Chapter 2 details two methods of stability prediction. One is the third-order updated full-discretization method in which the delayed term and state term are both interpolated by third-order polynomial. The other is the machine learning method based on function of support

vector machine. The structures of the dissertation and relations of the chapters are also shown in this chapter.

Chapter 3 will deal with dynamics of IPW with the method of structural dynamic modification (SDM) and finite element method (FEM). In this chapter, the proposed model considering material removal can assemble the change in mass and stiffness quickly by using geometric judgement conditions, and then the IPW dynamics will be extracted and verified.

Chapter 4 will introduce the dynamics of IPW along the tool path, multiple modes and process damping into the flexible milling systems in which the modal parameters of milling tool and workpiece were considered simultaneously. Afterwards, the third-order updated full-discretization method will be employed to solve the dynamic equation in modal space. Then, the three-dimensional SLD that varies with different modes and cutter location will be presented. Finally, different kinds of frequencies under different dominant modes of milling tool or workpiece will be identified and expounded through the experiments.

Chapter 5 will describe SLE prediction for continuous machining. In this chapter, the discrete element will be applied to construct cutting force model and the dynamic response of the IPW will be taken into account in the model of SLE. The stable machining parameters will be selected from the conservative SLD and the instability induced by continuous cutting will be eliminated. Then multiple radial immersions will be viewed as one-time material removal equivalently. Finally, third updated full-discretization method will be applied again to solve the dynamic equation for SLE, and the proposed model will be verified and illustrated by measurement results and roughness.

Chapter 6 will present the SLD and SLE prediction for micro-milling. In this chapter, a simplified analytical calculation model for micro-milling in shearing zone will be proposed by considering trochoidal tool trajectory and regenerative effect with micro-milling coefficients obtained through calibration experiments. The FRFs at micro-milling point will be determined by using RCSA and EMA. Then two three-dimensional diagrams will be established by combining SLE diagram with the depth of cut as a variation and SLD with the restricted/free overhang length of micro-milling tool as a variation comprehensively. Besides, the dynamic responses in cross and direct directions for both tool and workpiece will be taken into consideration in the predicted model of SLE. Finally, flank micro-milling experiments will be conducted to explain the predicted model of SLE and SLD.

Chapter 7 will draw the conclusion of whole dissertation and present the possible research direction in the future.
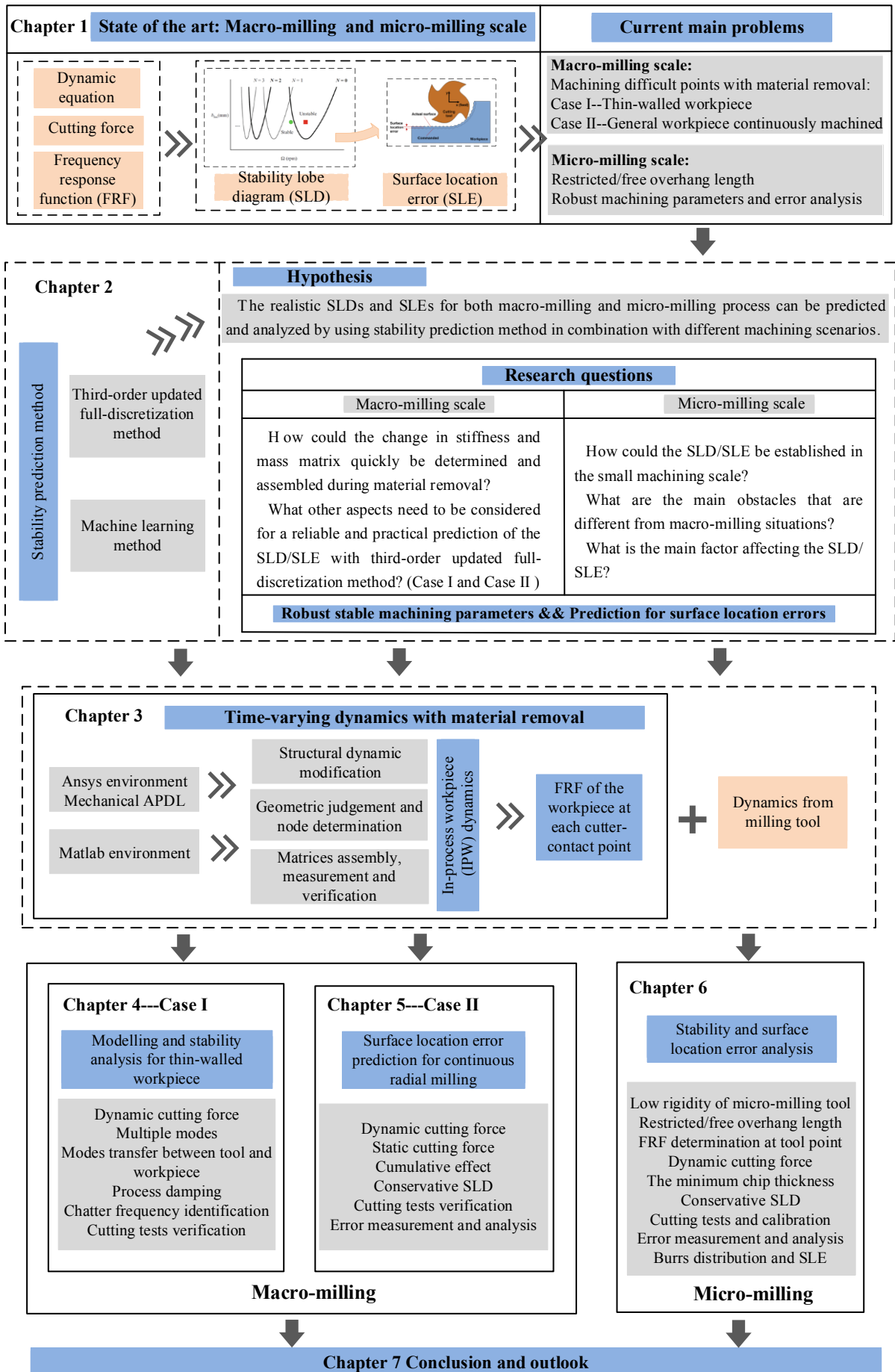
Fig. 14 Research questions and relations of the dissertation

3 Structural dynamic modification for in-process workpiece

During the machining process, the dominant mode of system depends on the response of machine-spindle or workpiece. For the specific machine-spindle, the dynamic change can be neglected. While the dynamic modal parameters of the workpiece will change significantly with continuous material removal, which has a significant impact on the vibration mode of the whole machining process. Determining the initial response of the workpiece in the clamping state and accurately predicting the dynamic response of the IPW can provide an important theoretical basis for the subsequent cutting process.

3.1 Determination for IPW mode shapes

The milling force acting on the workpiece entity would excite the first few mode shapes of workpiece, especially the first three modes, which makes the FRF of the workpiece changeable. Besides, the modal parameters of workpiece would show dynamic changes with the influence of material removal, so obtaining the modal parameters during IPW is the basis for dynamic analysis of workpiece. Here, the SDM method was used to get the dynamics of IPW [93].

The dynamic equation of the workpiece can be written as:

$$\mathrm{M}_w \ddot{\mathbf{q}}_w(t) + \mathrm{C}_w \dot{\mathbf{q}}_w(t) + \mathrm{K}_w \mathbf{q}_w(t) = \mathbf{F}_w(t) \tag{3.1}$$

where M_w, C_w and K_w are the mass matrix, damping matrix, and stiffness matrix of the workpiece respectively; $\mathbf{F}_w(t)$ is the force acting on the workpiece; $\mathbf{q}_w(t) = \begin{Bmatrix} x_w(t) \\ y_w(t) \end{Bmatrix}$.

For the initial workpiece, the undamped homogeneous equation is developed as:

$$\mathrm{M}_w \ddot{\mathbf{q}}_w + \mathrm{K}_w \mathbf{q}_w = \mathbf{0} \tag{3.2}$$

The eigenvalues and eigenvectors are yielded from Eq. (3.2):

$$\Lambda = \begin{bmatrix} \omega_{w1}^2 & & \\ & \ddots & \\ & & \omega_{wm_w}^2 \end{bmatrix}, \ \phi_w = \begin{bmatrix} \varphi_1, \varphi_2, \cdots \varphi_{m_w} \end{bmatrix} \tag{3.3}$$

where m_w is the number of excited modes of workpiece.

The eigenvectors satisfy the following conditions:

$$\phi_w^T \mathrm{M}_w \phi_w = \mathrm{M}_{wq} = \mathrm{I}, \quad \phi_w^T \mathrm{K}_w \phi_w = \mathrm{K}_{wq} = \Lambda \tag{3.4}$$

With the influence of material removal (ΔM_w and ΔK_w), the parametric matrices of initial workpiece would change and the Eq. (3.2) becomes:

$$(M_w + \Delta M_w)\ddot{q}_w + (K_w + \Delta K_w)q_w = 0 \tag{3.5}$$

By modal coordinate transformation of $\mathbf{q}_w = \phi_w \mathbf{\Gamma}_w$ and premultiplying by ϕ_w^T, the Eq. (3.5) becomes:

$$(I + \Delta \hat{M}_w)\ddot{\Gamma}_w + (\Lambda + \Delta \hat{K}_w)\mathbf{\Gamma}_w = 0 \tag{3.6}$$

where $\Delta \hat{M}_w = \phi_w^T \Delta M_w \phi_w$, $\Delta \hat{K}_w = \phi_w^T \Delta K_w \phi_w$

The corresponding characteristic equation of Eq. (3.6) is developed as:

$$[\underbrace{(\Lambda + \Delta \hat{K}_w)}_{\hat{K}_w} - \lambda_m \underbrace{(I + \Delta \hat{M}_w)}_{\hat{M}_w}]\phi_{wm} = 0 \tag{3.7}$$

Similarly to Eq. (3.5), a new transformation with $\mathbf{\Gamma}_w = \phi_{wm}\mathbf{\Gamma_m}$ and premultiplying by ϕ_{wm}^T is applied to the Eq. (3.6), and the new eigenvectors meet the following conditions:

$$\phi_{wm}^T \hat{M}_w \phi_{wm} = M_{wm} = I, \quad \phi_{wm}^T \hat{K}_w \phi_{wm} = K_{wm} = \Lambda_m \tag{3.8}$$

Therefore, the transformation in physical coordinates is obtained as：

$$\mathbf{q}_w = \phi_w \mathbf{\Gamma}_w = \phi_w \phi_{wm}\mathbf{\Gamma}_m = U_w \mathbf{\Gamma}_m \tag{3.9}$$

The new mode shapes of the IPW with material removal can be expressed as

$$U_w = \phi_w \phi_{wm} \tag{3.10}$$
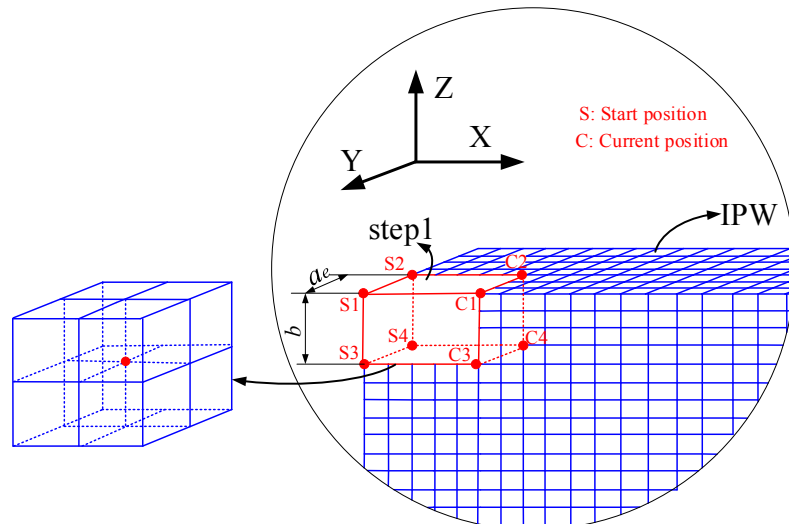
3.2 Obtaining the change in mass and stiffness

Fig. 15 Geometric condition judgement for material to be removed

The change in mass and stiffness was mainly dealt with in Ansys and Matlab environment. With the geometry of the workpiece modeled and analyzed in Ansys, the mapping data extracted from Ansys should be saved. These mapping data included node number on each element, coordinates of each node and equations of each node. In Ansys environment, the workpiece was meshed and the range of axial depth of cut was scanned on the workpiece. In order to get rid of the shear locking effect, the situation that two directions are larger than the third should be avoided during fine-mesh formulation. After the element stiffness matrices were extracted from Ansys, the number of nodes to be removed was judged at each discretization cutter-contact point with axial depth of cut.

According to the initial coordinate of workpiece, the cutter-location and cutter-contact points were determined, which included the discretization numbers along machining path, the axial and radial depth of cut. The cutter-location points along the machining path and cutter-contact points along the axial depth were defined as *steps* (*i=1,2,...steps*) and *stz* (*k=1,2,...stz*) respectively. At the ith step and k^{th} axial depth of cut of the cutter location, the elements of material removal would be identified by geometric conditions. That is, the coordinates of nodes were judged whether they were in the vertex coordinates of the hexahedron S1S2S3S4-C1C2C3C4 (see Fig. 15). The corresponding coordinates (x_{nw}, y_{nw}, z_{nw}) should satisfy the following conditions:

$$\begin{cases} x_{S1orS2orS3orS4} \le x_{nw} \le x_{C1orC2orC3orC4} \\ y_{S1orC1orS3orC3} \le y_{nw} \le y_{S2orC2orS4orC4} \\ z_{S3orS4orC3orC4} \le z_{nw} \le z_{S1orS2orC1orC2} \end{cases} \tag{3.11}$$
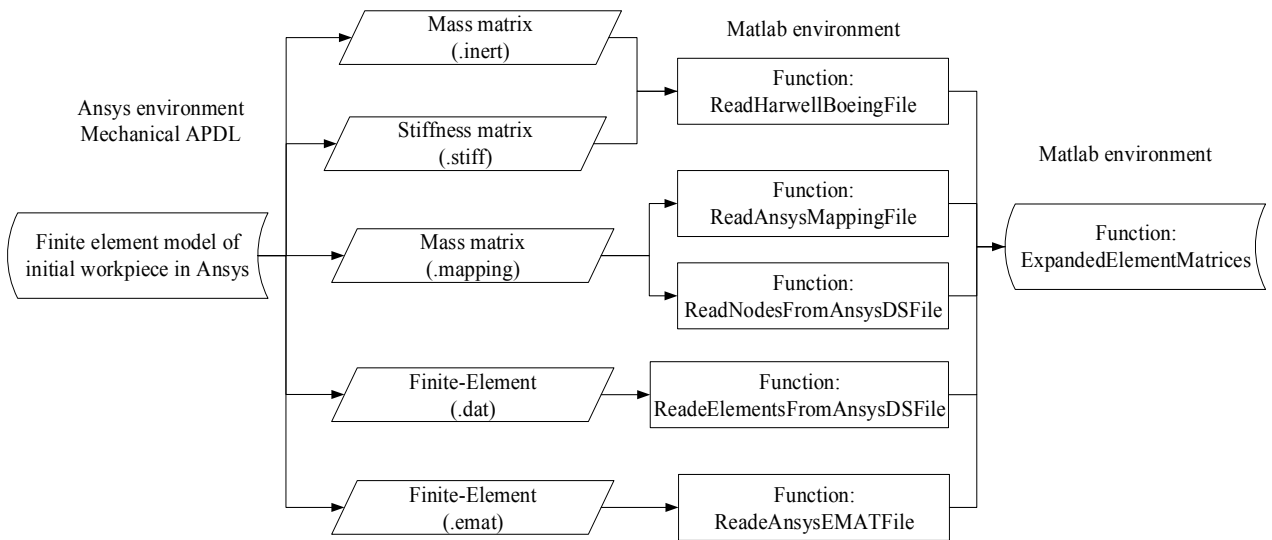

Fig. 16 Procedure for obtaining the element mass and stiffness matrix of the workpiece

In addition to the nodes that satisfied the geometric conditions at the boundary of the hexahedron, eight elements around the node in the hexahedron need to be removed. Then these nodes in hexahedron were saved, and the corresponding elements were assembled the change in mass and stiffness (ΔM_w and ΔK_w) instead of softening the material to be removed, which differs from the method described in Ref [31]. In this case, the change in mass and stiffness (ΔM_w and ΔK_w) would be established easily according to the coordinates.

In the Fourier-domain, Eq. (3.1) becomes:

$$(i\omega)^2 M_w \mathbf{q}_w(\omega) + (i\omega) C_w \mathbf{q}_w(\omega) + K_w \mathbf{q}_w(\omega) = \mathbf{F}_w(\omega) \tag{3.12}$$

In order to decouple the modes in the subsystem of workpiece, the modal transformation is applied as:

$$\begin{cases} \mathbf{q}_w(t) = \phi_w \mathbf{\Gamma}_w(t) \\ \mathbf{q}_w(\omega) = \phi_w \mathbf{\Gamma}_w(\omega) \end{cases} \tag{3.13}$$

Then Eq. (3.12) can be arranged as:

$$-\omega^2 \phi_w^T M_w \phi_w \mathbf{\Gamma}_w(\omega) + (i\omega) \phi_w^T C_w \phi_w \mathbf{\Gamma}_w(\omega) + \phi_w^T K_w \phi_w \mathbf{\Gamma}_w(\omega) = \phi_w^T \mathbf{F}(\omega) \tag{3.14}$$

After mass normalization, the FRF of the workpiece can be written as:

$$\mathbf{H}(\omega) = \frac{\mathbf{q}_w(\omega)}{\mathbf{F}(\omega)} = \frac{\phi_w \Gamma_w(\omega)}{\mathbf{F}(\omega)} = \sum_{r=1}^{m_w} \frac{\{\phi_w\}_r \{\phi_w^T\}_r}{\omega_r^2 - \omega^2 + 2i\zeta_r \omega_r \omega} \tag{3.15}$$

The natural frequency could be extracted from Eq. (3.8), and the mode shapes of IPW could be obtained from U_w. In modal coordinate, mode shapes at different nodes would be used to estimate the FRF for designated excitation point e and displacement point u:

$$\begin{cases} M' = U_w^{-T} [\underbrace{U_w^T (M_w - \Delta M_w) U_w}_{\mathbf{I}}] U_w^{-1} = (\psi_{near}^{-1})^2 \mathbf{I}_{1 \times m_w} \\ K' = U_w^{-T} [\underbrace{U_w^T (K_w - \Delta K_w) U_w}_{\Lambda_m}] U_w^{-1} = (\psi_{near}^{-1})^2 (\Lambda_m)_{1 \times m_w} \\ \omega_r = \sqrt{K'/M'}, \quad r = 1, 2, \cdots \\ H_{ue}(\omega) = \sum_{r=1}^{m_w} \frac{\{U_w^u\}_r \{U_w^e\}_r}{\omega_r^2 - \omega^2 + i2\zeta_r \omega_r \omega} \end{cases} \tag{3.16}$$

where ψ_{near} is the nearest response node of the IPW to the tool point, U_w is the mass normalized mode shape, and ω_r is the natural frequency of the rth mode; M' and K' are the updated mass and stiffness matrices of IPW along the machining direction.

The element mass and stiffness matrix to be removed were preserved with binary conversion, and the change in mass and stiffness matrix, i.e., $\Delta\mathrm{M}_w$ and $\Delta\mathrm{K}_w$, were obtained. It should be noted that the mass and stiffness matrix take negative values in Eq. (3.16). In order to further verify the consistency between the change in mass matrix and the actual removal mass, the difference between the assembled mass matrix, $\sum\Delta\mathrm{M}_w/3$, and the actual volume of material removal, $\rho\mathrm{v}$ (density and volume), should be calculated.

As illustrated in Fig. 16, the main Matlab code for the above process is as follows

```
for i=1:Step
    for y=1:stz+1
        b=(b_st+(y-1)*(b_fi-b_st)/stz);
        InP{y}=[0,55e-3,4e-3; 0,55e-3,(4e-3)-ae; 0,(55e-3)-b,4e-3; 0,(55e-3)-b,(4e-3)-ae];
        CuP{i,y}=[i*INT,55e-3,4e-3; i*INT,55e-3,(4e-3)-ae; i*INT,(55e-3)-b,4e-3; i*INT,(55e-3)-b,(4e-3)-ae];
        SaveNodeMatlab{i,y}=[];
        SaveNodeAnsys{i,y}=[];
        SaveEquation{i,y}= [];
        NumberofNodes= length(Nodes.NodeNumbers);
        Distance{i,y}(1:NumberofNodes,1)= 0;
        for No=1:NumberofNodes
            if ((Nodes.Coordinates(No,1)<=CuP{i,y}(3,1)&&Nodes.Coordinates(No,1)>=InP{y}(1,1))...
                &&(Nodes.Coordinates(No,2)>=CuP{i,y}(3,2)&&Nodes.Coordinates(No,2)<=CuP{i,y}(1,2))...
                &&(Nodes.Coordinates(No,3)<=CuP{i,y}(3,3)&&Nodes.Coordinates(No,3)>=CuP{i,y}(4,3)))
                SaveNodeMatlab{i,y}= [SaveNodeMatlab{i,y};No];
                SaveNodeAnsys{i,y}= [SaveNodeAnsys{i,y}; Nodes.NodeNumbers(No)];
            end
            Distance{i,y}(No)= norm(Nodes.Coordinates(No,:)-CuP{i,y}(4,:));
        end
        SingleEle{i,y}=FindElemsToRemove( SaveNodeMatlab{i,y}, Body.NodeNumbers );
        DeltaM{i,y}=sparse(Di,Di);
        DeltaK{i,y}=sparse(Di,Di);
        for q1=1:length(SingleEle{i,y})
            DeltaM{i,y}=DeltaM{i,y}+ExpandedElements.ElemMass{SingleEle{i,y}(q1)};
        end
        for q2=1:length(SingleEle{i,y})
            DeltaK{i,y}=DeltaK{i,y}+ExpandedElements.ElemStiff{SingleEle{i,y}(q2)};
        end
        [Value{i,y}, Index{i,y}]= min (Distance{i,y});
        NearestNode{i,y}= Nodes.NodeNumbers(Index{i,y});
        [~ , EquationIndex{i,y}] = ismember(NearestNode{i,y},Mapping.vNodeNum);
        EquationNumberX{i,y}= Mapping.vEqnLoc(EquationIndex{i,y});
        EquationNumberZ{i,y}= EquationNumberX{i,y}+2;
        NewM{i,y}=AsEVec'*AsFullM*AsEVec+AsEVec'*(-DeltaM{i,y})*AsEVec;
        NewK{i,y}=AsEVec'*AsFullK*AsEVec+AsEVec'*(-DeltaK{i,y})*AsEVec;
        [NewEVec{i,y}, NewEVal{i,y}]= eigs(NewK{i,y},NewM{i,y});
        NewModalMass{i,y}=NewEVec{i,y}'*NewM{i,y}*NewEVec{i,y};
        NewModalStiff{i,y}=NewEVec{i,y}'*NewK{i,y}*NewEVec{i,y};
        MassInitMod{i,y}= diag( NewModalMass{i,y});
        StiffInitMod{i,y}= diag( NewModalStiff{i,y});
        Psi{i,y}=AsEVec*NewEVec{i,y};
        MassPos{i,y}= (1./Psi{i,y}(EquationNumberZ{i,y},:).^2)'.* MassInitMod{i,y};
        StiffPos{i,y}= (1./Psi{i,y}(EquationNumberZ{i,y},:).^2)'.*StiffInitMod{i,y};
        varfreq{i,y}=sqrt(StiffPos{i,y}./MassPos{i,y})/(2*pi);
    end
end
```

3.3 Verification for IPW at certain point

3.3.1 Dynamic tests

During the impact tests, the capacitive sensor was used as the main signal acquisition apparatus so that no additional mass would be introduced on the measured targets. The measurement tasks were completed by capacitive sensor and data processing system. The gauge type of the capacitive sensor is: Type 5810 (ADE Technologies). The data acquisition and analysis software system is: Type 3560 (Brüel & Kjær) with 6-chanel input module.
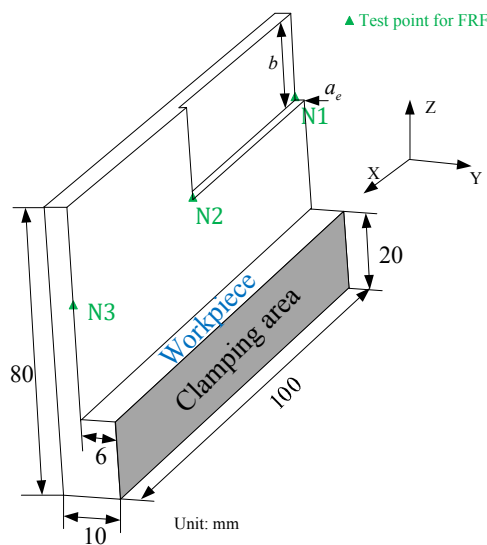

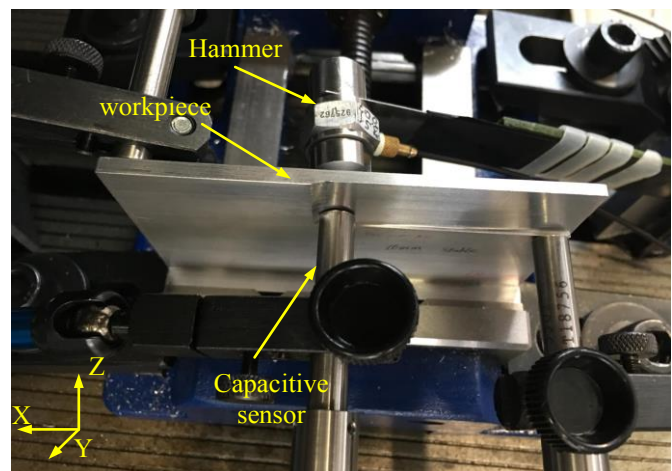Fig. 17 Measurement plan for FRF of workpiece at certain points.

Fig. 18 Experimental setup for impact tests

Table 3 Identified damping ratios and simulated frequencies at N1

Number of modes	Simulated frequencies (Hz)	Assembled frequencies (Hz)	Natural frequencies (Hz)	Damping ratio (%)
1	951	940	973	0.39
2	1585	1640	1608	0.18
3	3334	3337	3317	0.09

The material of workpiece was Aluminum alloy 7075 with the valid geometry parameters being 100 mm×60 mm×4 mm (see Fig. 17), density of 2770 kg/m^3, Young's modulus of 71 GPa and Poisson's ratio of 0.33, and the height clamped by the fixture was 20 mm. Fig. 18 depicts the measurement setup of the workpiece. In terms of the impact tests for initial workpiece, the purpose for that was to identify the damping ratio which was nearly impossible to be extracted by prediction or simulation. As the damping ratio was small, it

could be considered as a constant during the whole process. The identified damping ratios and simulated parameters at N1 in Fig.17 were presented in Table 3.

In order to obtain a larger measurement area, the axial and radial depth of cut for the test points in Fig. 17 were 15 mm and 1 mm respectively. As shown in Figs. 18 and 19, the predicted, simulated and measured frequencies of the workpiece had the same trend of change. The first and second order frequencies of the modified workpiece increased slightly, while the third order decreased gradually. This showed that the simulated frequency of the workpiece was in good agreement with the actual machining condition and the proposed prediction method for IPW dynamics worked well.
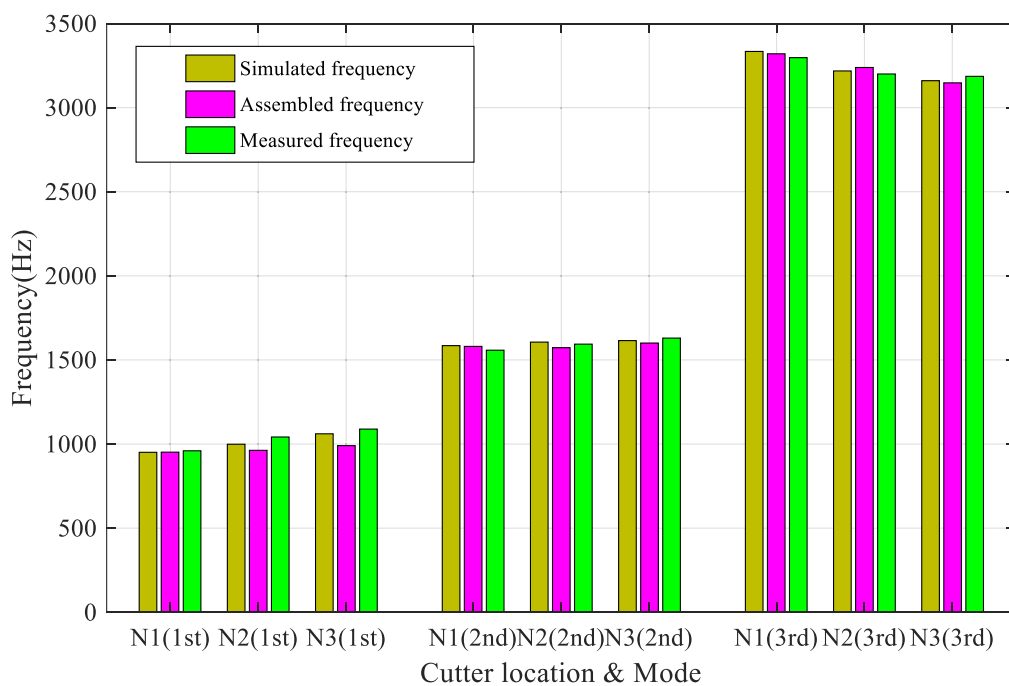

Fig. 19 Frequency change for different cutter location

Mode	Simulation	Experimental result
First		

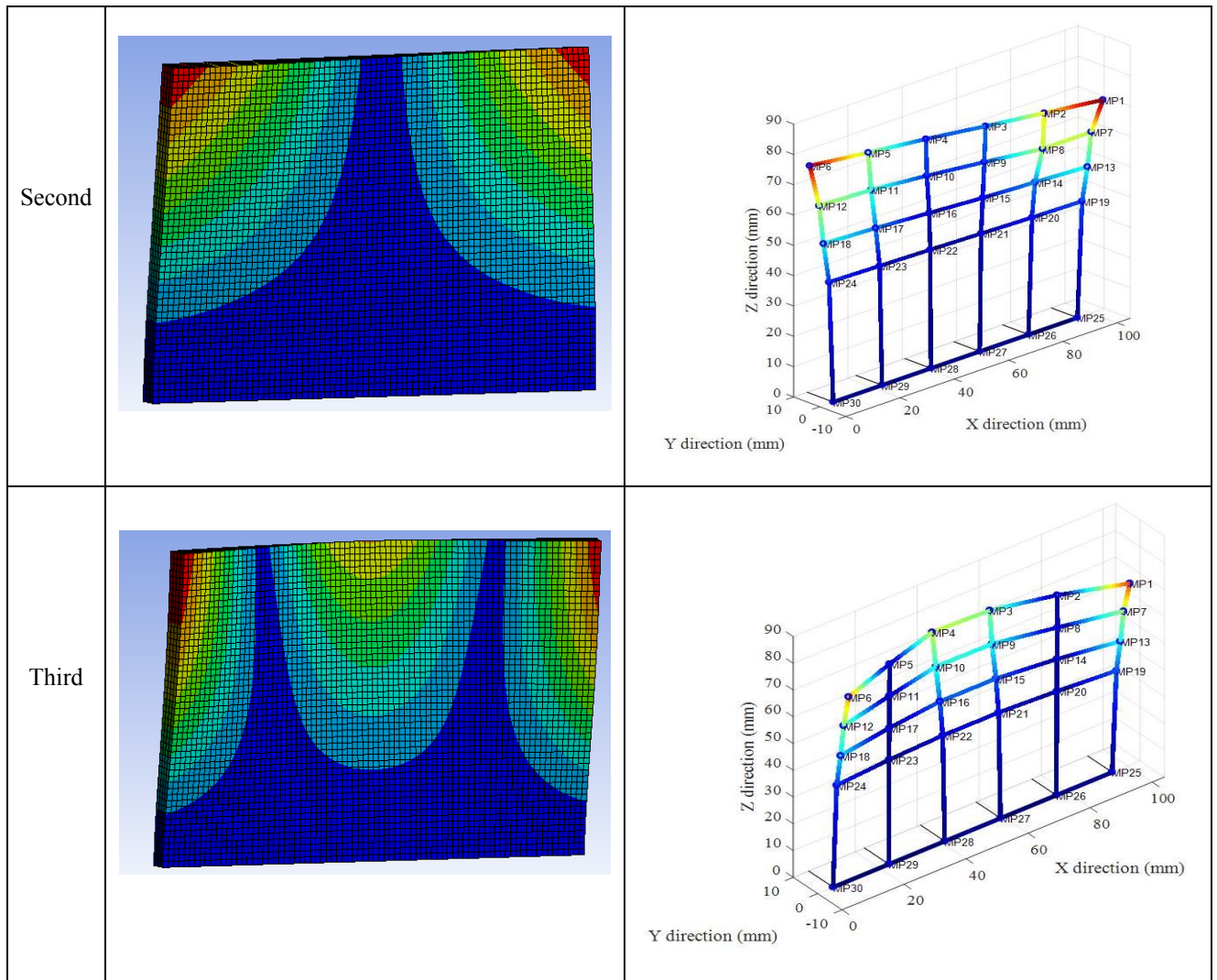|		
Second		
Third		

Fig. 20 Mode shapes comparison between simulation and experiment measurement

In order to reduce the measurement error, two capacitive sensors were applied to collect the FRF of the workpiece. As shown in Fig. 18, one sensor was fixed and the other sensor moved with the measurement point. The ratio of the two sensors was taken as the experimental measurement value. As shown in Fig. 20, it could be seen that the modal deformation of the workpiece with simulation and experiment cases tended to be the same. This means in the actual clamping process, the base of the workpiece was in rigid contact with the fixture, and the workpiece was completely limited at the bottom part. In fact, the damping ratios ζ were not constant but varied with different excitation points. As illustrated in Fig. 21, the damping ratio decreased with the increase of order, but it increased first and then decreased in terms of cutter location from N1 to N3.
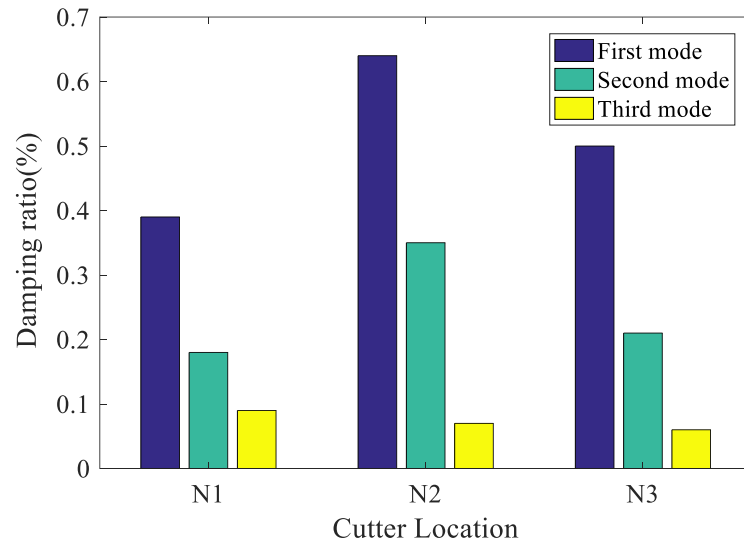
33

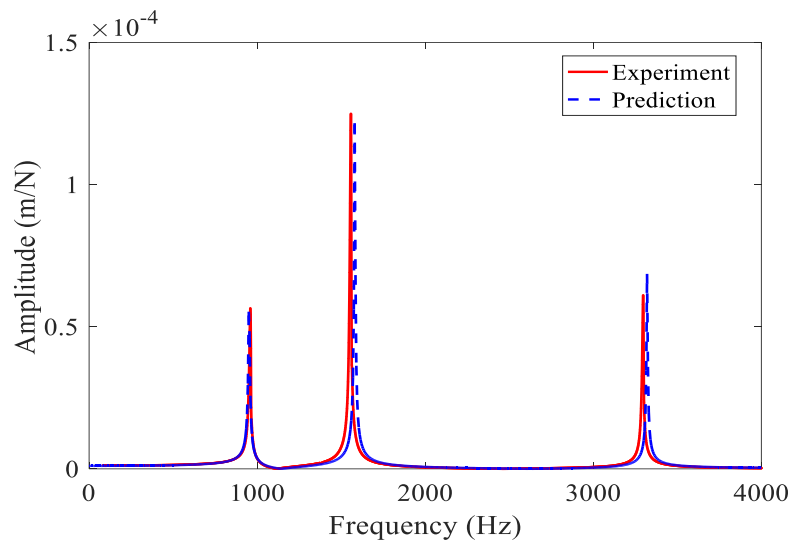Fig. 21 Damping ratio change for different cutter location

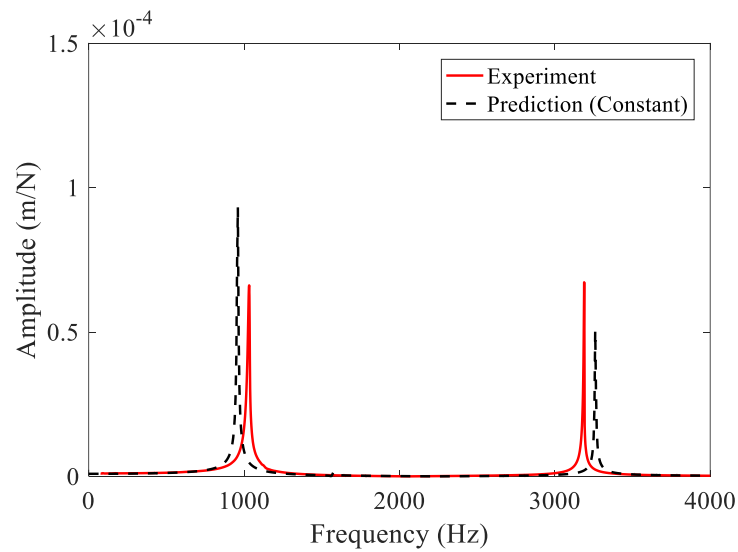Fig. 22 Comparison between measured and predicted FRF at N1

Fig. 23a Comparison between measured and predicted FRF at N2 with constant damping ratio
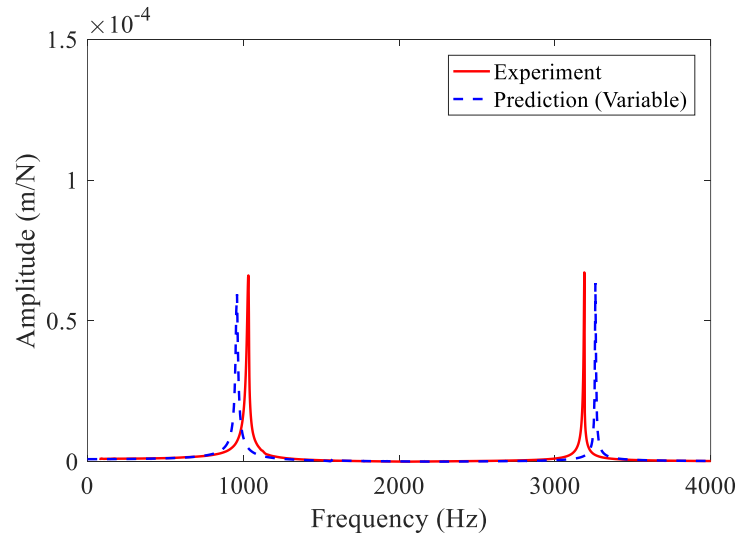
Fig. 23b Comparison between measured and predicted FRF at N2 with variable damping ratio
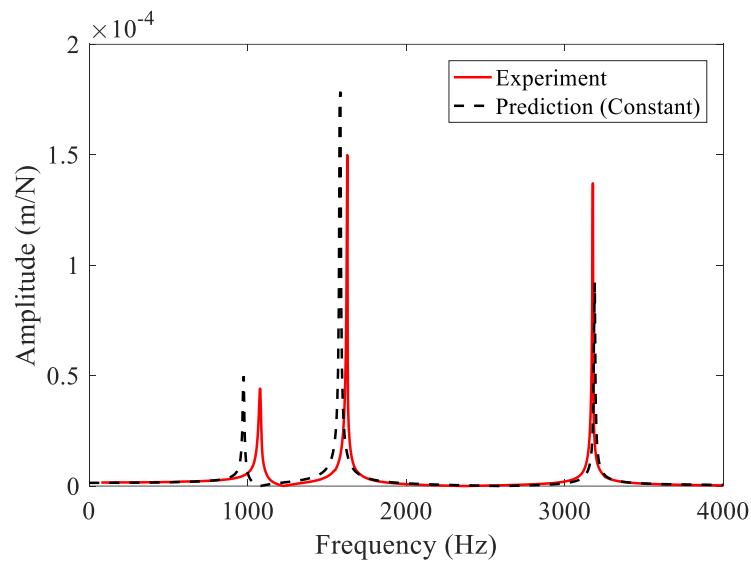

Fig. 24a Comparison between measured and predicted FRF at N3 with constant damping ratio
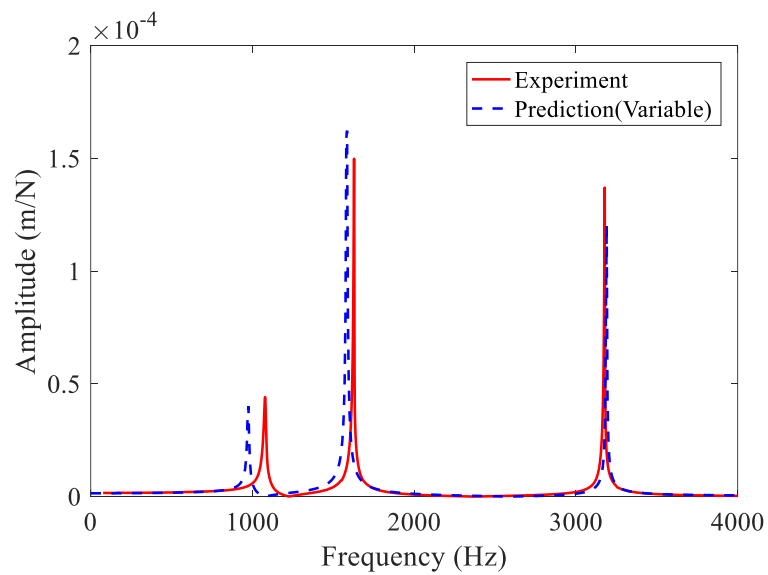

Fig. 24b Comparison between measured and predicted FRF at N3 with variable damping ratio

3.3.2 Analysis for the impact tests

As shown in Figs. 22-24, the FRFs at points N1, N2 and N3 in Fig. 17, i.e. H_{yy}^{N1}, H_{yy}^{N2} and H_{yy}^{N3}, can be obtained with Eq. (3.16), and the maximum frequency error appeared at point N3 with the value of 7.5 %. The frequency error between prediction and experiment mainly caused by the truncation effect of eigenmodes which cannot be determined a priori. Besides, the error from the assembled element stiffness matrix would accumulate with the increase of material removal. In terms of the predicted and measured magnitude, they nearly had the same order of magnitude. The magnitude discrepancy between predicted and measured FRF can be attributed to the damping ratio, and the slight change of damping ratio would have influence on the predicted magnitude. In addition, uncertainty still existed in the actual measured value, which was also an important reason for the inconsistency between the predicted value and the measured value.

In fact, the IPW dynamics is mainly reflected by FRF at the corresponding machining point. Eq. (3.16) shows that, without considering the damping ratio of the workpiece, the FRF at a certain point of the workpiece depends not only on the natural frequency, but also on the mode shapes. In terms of the thin-walled workpiece, the normalized mode shapes become larger when the test points get close to the free end of the workpiece. After the mode shape is squared in Eq. (3.16), its influence on FRF will further increase. Therefore, the natural frequency, mode shapes and damping ratio work together to affect the IPW dynamics. Compared with the experimental results, it can be seen that the method of assembling element stiffness matrix would effectively predict the dynamics of IPW.

3.4 Summary

The method proposed in this chapter mainly used node coordinates of elements to determine material to be removed. The method considering material removal could assemble the change in mass and stiffness quickly by using geometric judgement conditions, and then the IPW dynamics would be extracted. Compared with the experimental results, the assembled model had higher prediction accuracy. Although the fine mesh applied in Ansys environment increased the number of elements and made the calculation time-consuming, the elements refinement can predict the material of thin-walled workpiece to be removed much better. When coarse mesh was employed, additional attention should be paid to whether the elements exceeded the intended boundary or not. Otherwise, the theoretical removal volume of material would be greater than the expected volume, which would cause larger prediction

error. For sculptured surface machining, this method can also be employed to discretize the surface and then determine the material to be removed.

In addition, many conditions in practical machining process were difficult to input or describe in the simulation software, and the boundary conditions set in the simulation environment were not completely consistent with the conditions in practical machining process. Therefore, it was necessary to compare experimental results with simulation. The reason why the experimental results deviated from the simulation was whether the workpiece and fixture were in rigid contact. As the base of workpiece was clamped, the vibration of the thin-walled workpiece above the base accorded with the simulation. The non-rigid contact between workpiece and fixture will be dealt with in Chapter 5.

4 Modelling and stability analysis for thin-walled workpiece

4.1 Modelling of the milling force with process damping

Since the whole machining process mainly involves the dynamic behavior of workpiece and machine tool, the single dynamics of machine tool or workpiece cannot reflect the actual dynamic response of the flexible system completely. In order to analyze the modal characteristics of the workpiece and the milling tool simultaneously, the milling tool is sectioned into *stz* number of differential elements with the height of Δb [7] [34]. Fig. 25 depicts the interaction between milling tool and thin-walled workpiece schematically.
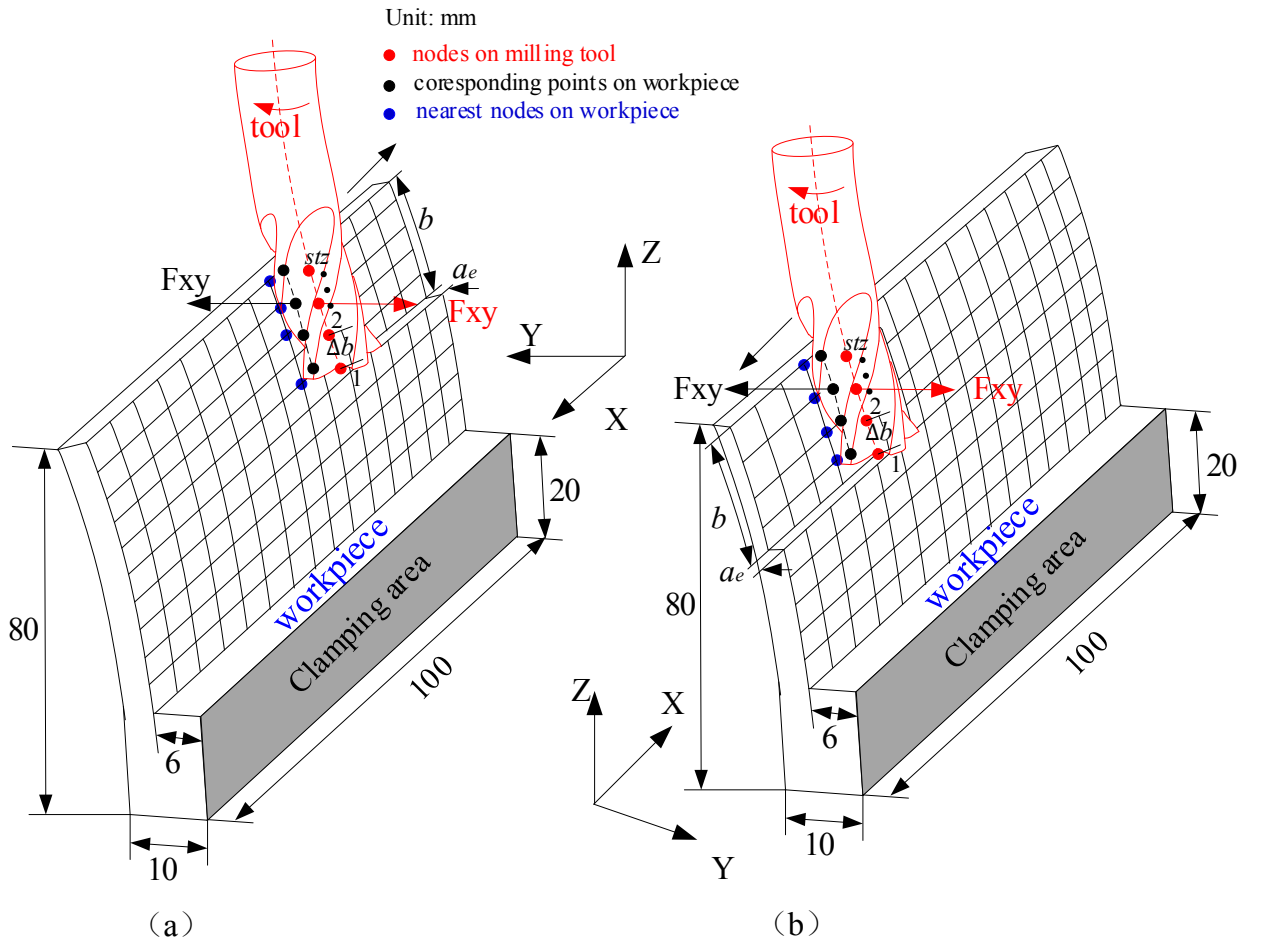

Fig. 25 Dynamic model of flexible milling system: (a) down-milling, (b) up-milling.

As shown in Fig. 26, the relative instantaneous uncut chip thickness for j^{th} tooth is written as:

$$h_j(t) = f_z \sin(\phi_j) + [((\eta_t(t) - \eta_t(t-\tau)) - ((\eta_w(t) - \eta_w(t-\tau))] \tag{4.1}$$

where $\begin{cases} \eta_t = [\sin(\phi_j), \cos(\phi_j)]\mathbf{q}_t(t) \\ \eta_w = [\sin(\phi_j), \cos(\phi_j)]\mathbf{q}_w(t) \end{cases}$, $\mathbf{q}_t(t) = \begin{Bmatrix} x_t(t) \\ y_t(t) \end{Bmatrix}$

Then Eq. (4.1) becomes:

$$h_j(t) = f_z \sin(\phi_j) + [\sin(\phi_j),\ \cos(\phi_j)]\big((\mathbf{q}_t(t) - \mathbf{q}_t(t-\tau)) - (\mathbf{q}_w(t) - \mathbf{q}_w(t-\tau))\big) \tag{4.2}$$

where f_z is the feed per tooth, ϕ_j is the instantaneous angular position; and τ is the time delay between the current tooth j and previous tooth j-1. The subscripts of $x(t)$ and $y(t)$: t and w, represent the displacement of milling tool and workpiece in X and Y direction respectively.

The vibration of workpiece and milling tool is described in the Cartesian coordinate system $(x-y)$, and the possible multiple eigen modes of milling tool and workpiece are defined as:

$$\begin{cases} \mathbf{q}_t(t) = [\mathbf{q}_t^1(t), \mathbf{q}_t^2(t), \cdots \mathbf{q}_t^{m_t}(t)]^{\mathrm{T}} & m_t = 0,1,2,\cdots \\ \mathbf{q}_w(t) = [\mathbf{q}_w^1(t), \mathbf{q}_w^2(t), \cdots \mathbf{q}_w^{m_w}(t)]^{\mathrm{T}} & m_w = 0,1,2,\cdots \end{cases} \tag{4.3}$$

where m_t is the number of excited modes of milling tool.

The angular delay would appear with the helix angle considered, so the instantaneous angular position of jth tooth and k^{th} element is developed as:

$$\phi_j = \phi_j(t, k \bullet \Delta b) = \frac{2\pi\Omega}{60}t + (j-1)\frac{2\pi}{N} - (k-1)\frac{2\tan\beta}{D}\Delta b \quad j = 1,2,\cdots,N;\ \ k = 1,2,\cdots,stz \tag{4.4}$$

where N is the number of flutes, β is the helix angle, and Ω (rpm) is the spindle speed.

During the milling process, most of energy from the spindle-tool is dissipated in the shearing zone above the milling separation point [94], and the ploughing zone below the point also consumes some energy to suppress the amplitude and chatter, which constrains the vibration of workpiece and milling tool. These constraints formed from indentation volume in ploughing zone are the origin of process damping, which adds nonlinear factors to the dynamic equation. The process damping for the jth tooth is proportional to indentation volume and modelled as [37]:

$$\begin{cases} dF_{rpd,j} = K_{pd}dV_j \\ dF_{tpd,j} = \mu dF_{rpd,j} \end{cases} \tag{4.5}$$

where K_{pd} is the indentation coefficient, μ is the frictional coefficient; and dV_j is the incremental indentation volume for the jth tooth of milling tool.

The indentation coefficient is determined by material properties of workpiece, and it satisfies the following equation [95]:

$$K_{pd} = \frac{E}{1.29\rho_1(1-2v)} \tag{4.6}$$

where ρ_1 is the distance across the elastic-plastic deformation zone, V is the Poisson's ratio; and E is the Young's modulus.
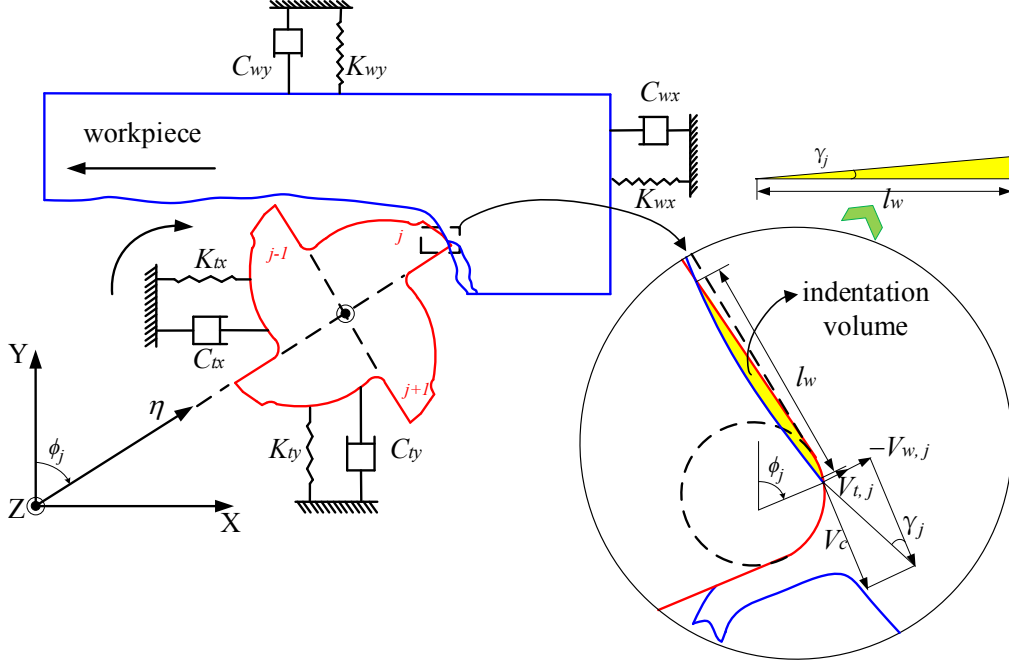

Fig. 26 Simplified model of process damping (up-milling).

With assuming that the flank wear width fully immerses in the ploughing zone, the indentation area in the model of the process damping is simplified as a triangular [40], i.e. the effective orthogonal clearance angle of jth tooth, γ_j, and the flank wear width, l_w, which are used to calculate the indentation area A_j [96]. The indentation area directly affects the interaction between flank face and workpiece when the vibration of milling tool and workpiece in the contact directions is taken into account. The effective orthogonal clearance angle of the jth tooth, γ_j, is developed as:

$$\gamma_j \approx \tan^{-1}\left(\frac{\dot{\eta}_{t,j} - \dot{\eta}_{w,j}}{v_c}\right) \approx \frac{v_{t,j} - v_{w,j}}{v_c} \tag{4.7}$$

$$\mathrm{d}V_j = A_j dz = \frac{1}{2} l_w * l_w \sin(\gamma_j)\,\mathrm{d}z \approx \frac{1}{2} l_w^2 \frac{v_{t,j} - v_{w,j}}{v_c}\,\mathrm{d}z \tag{4.8}$$

where v_c is the cutting speed $v_c = \dfrac{\pi d\Omega}{60}$, $v_{t,j}$ and $v_{w,j}$ are vibration speed of the jth tooth of milling tool and workpiece respectively.

According to the Eq. (4.2), the relative vibration velocity between the tool and workpiece is expressed as:

$$v_{t,j} - v_{w,j} = [\sin(\phi_j), \cos(\phi_j)](\dot{\mathbf{q}}_t(t) - \dot{\mathbf{q}}_w(t)) \tag{4.9}$$

The energy consumed below the separation point is assumed to be dissipated by the viscous damping force of the whole machining process system according to the law of conservation of energy. Then the equivalent process damping coefficients (C_{eqr}, C_{eqt}) in radial and tangential directions are written as:

$$C_{eqr} = \frac{K_{pd} l_w^2}{2v_c}, \quad C_{eqt} = \frac{\mu K_{pd} l_w^2}{2v_c} \tag{4.10}$$

The tangential force ($F_{t,j}$) and radial force ($F_{r,j}$) acting on the jth tooth of the milling tool include the forces in shearing zone and ploughing zone, i.e., the shearing term ($F_{ts,j}$ and $F_{rs,j}$), ploughing term ($F_{tp,j}$ and $F_{rp,j}$) and process damping term ($F_{tpd,j}$ and $F_{rpd,j}$). Therefore, the tangential and radial force can be written as:

$$
\begin{aligned}
\begin{Bmatrix} \mathrm{d}F_{t,j} \\ \mathrm{d}F_{r,j} \end{Bmatrix} &= \begin{Bmatrix} \mathrm{d}F_{ts,j} \\ \mathrm{d}F_{rs,j} \end{Bmatrix} + \begin{Bmatrix} \mathrm{d}F_{tp,j} \\ \mathrm{d}F_{rp,j} \end{Bmatrix} + \begin{Bmatrix} \mathrm{d}F_{tpd,j} \\ \mathrm{d}F_{rpd,j} \end{Bmatrix} = g(\phi_j)\Delta b \left(\begin{Bmatrix} K_t \\ K_r \end{Bmatrix} h_j(t) + \begin{Bmatrix} K_{te} \\ K_{re} \end{Bmatrix} + \begin{Bmatrix} C_{eqt} \\ C_{eqr} \end{Bmatrix}(v_{t,j} - v_{w,j}) \right) \\
&= g(\phi_j)\Delta b \left[\begin{Bmatrix} K_{te} \\ K_{re} \end{Bmatrix} + f_z \begin{Bmatrix} K_t \\ K_r \end{Bmatrix}\sin(\phi_j) + \begin{Bmatrix} K_t \\ K_r \end{Bmatrix} \mathbf{T}_j \left((\mathbf{q}_t(t) - \mathbf{q}_t(t-\tau)) - (\mathbf{q}_w(t) - \mathbf{q}_w(t-\tau)) \right) \right. \\
&\quad \left. + \begin{Bmatrix} C_{eqt} \\ C_{eqr} \end{Bmatrix} \mathbf{T}_j \left((\dot{\mathbf{q}}_t(t) - \dot{\mathbf{q}}_t(t-\tau)) - (\dot{\mathbf{q}}_w(t) - \dot{\mathbf{q}}_w(t-\tau)) \right) \right]
\end{aligned} \tag{4.11}
$$

where K_{te} and K_{re} are the edge force coefficients, K_t and K_r are the cutting force coefficients. $\mathbf{T}_j$ is the transformation matrix, and it defines: $\mathbf{T}_j = [\sin(\phi_j), \cos(\phi_j)]$.

The force on each tooth needs to be projected onto the fixed coordinate system ($x-y$) of the milling tool:

$$\begin{Bmatrix} \mathrm{d}F_{tx} \\ \mathrm{d}F_{ty} \end{Bmatrix} = \sum_{j=1}^{N} \mathbf{W}_j \begin{Bmatrix} \mathrm{d}F_{t,j} \\ \mathrm{d}F_{r,j} \end{Bmatrix} \tag{4.12}$$

where $\mathbf{W}_j$ is the coordinate transformation matrix of the milling tool, and it satisfies:

$$\mathbf{W}_j = \begin{bmatrix} -\cos(\phi_j) & -\sin(\phi_j) \\ \sin(\phi_j) & -\cos(\phi_j) \end{bmatrix}.$$

In order to study the effect of dynamic cutting, the static cutting term and ploughing term are dropped from Eq. (4.11). Substituting Eq. (4.11) into Eq. (4.12) yields:

$$dF_{t,k,xy} = \begin{Bmatrix} dF_{tx} \\ dF_{ty} \end{Bmatrix} = \Delta b C(t) \left(\left(\mathbf{q}_t(t) - \mathbf{q}_t(t-\tau) \right) - \left(\mathbf{q}_w(t) - \mathbf{q}_w(t-\tau) \right) \right)$$

$$+ \Delta b E(t) \left(\left(\dot{\mathbf{q}}_t(t) - \dot{\mathbf{q}}_t(t-\tau) \right) - \left(\dot{\mathbf{q}}_w(t) - \dot{\mathbf{q}}_w(t-\tau) \right) \right) \quad k = 1, 2 \cdots stz \quad (4.13)$$

where $C(t) = \sum_{j=1}^{N} g(\phi_j) \mathbf{W}_j \begin{Bmatrix} K_t \\ K_r \end{Bmatrix} \mathbf{T}_j$, and $E(t) = \sum_{j=1}^{N} g(\phi_j) \mathbf{W}_j \begin{Bmatrix} C_{eqt} \\ C_{eqr} \end{Bmatrix} \mathbf{T}_j$.

For the milling tool, the resultant milling force acting on discrete differential elements can be written as:

$$\mathbf{F}_{t,xy}(t) = \begin{pmatrix} dF_{t,1,xy} \\ \vdots \\ dF_{t,k,xy} \\ \vdots \\ dF_{t,stz,xy} \end{pmatrix} \quad (4.14)$$

The forces acting on the discrete nodes of tool and workpiece are action-reaction forces, so they have opposite directions:

$$\mathrm{F}_{w,xy} = -\mathrm{F}_{t,xy} \quad (4.15)$$

4.2 Developing the 3D stability lobe diagram (SLD) with multiple modes

4.2.1 The comprehensive SLD enveloped during IPW

According to the above description, the dynamic equation of system is written as:

$$\mathbf{M}\ddot{\mathbf{Q}}(t) + \mathbf{C}\dot{\mathbf{Q}}(t) + \mathbf{K}\mathbf{Q}(t) = \mathbf{F}(t) \quad (4.16)$$

where $\mathbf{M} = \begin{bmatrix} \mathrm{M}_t & \\ & \mathrm{M}_w \end{bmatrix}$, $\mathbf{C} = \begin{bmatrix} \mathrm{C}_t & \\ & \mathrm{C}_w \end{bmatrix}$, $\mathbf{K} = \begin{bmatrix} \mathrm{K}_t & \\ & \mathrm{K}_w \end{bmatrix}$, $\mathbf{Q}(t) = [\mathbf{q}_t(t), \mathbf{q}_w(t)]$, and

$\mathbf{F}(t) = [\mathrm{F}_{t,xy}, \mathrm{F}_{w,xy}]^T$. $\mathbf{M}$, $\mathbf{C}$ and $\mathbf{K}$ are the mass matrix, damping matrix and stiffness matrix respectively.

Compared with physical space, the excited modes of tool-workpiece in modal coordinate can be decoupled, so the calculation process would be simplified in modal space [7]. Since the multiple modes of workpiece and tool may be excited simultaneously, Eq. (4.16) is solved in modal coordinates to facilitate the introduction of multiple modes. The modal transformation is defined as:

$$\mathbf{Q}(t)_{2stz \times 1} = U\mathbf{\Gamma}(t) = [U_t, -U_w]\mathbf{\Gamma}(t)_{(m_t + m_w) \times 1} \quad (4.17)$$

The mode shapes of milling tool and workpiece, U_t and U_w, can be defined as:

$$U_t = \begin{pmatrix} u_{x1,1,t} & u_{x1,2,t} & \cdots & u_{x1,m_t,t} \\ u_{y1,1,t} & u_{y1,2,t} & \cdots & u_{y1,m_t,t} \\ \vdots & \vdots & \ddots & \vdots \\ u_{xk,1,t} & u_{xk,2,t} & \cdots & u_{xk,m_t,t} \\ u_{yk,1,t} & u_{yk,2,t} & \cdots & u_{yk,m_t,t} \\ \vdots & \vdots & \ddots & \vdots \\ u_{xstz,1,t} & u_{xstz,2,t} & \cdots & u_{xstz,m_t,t} \\ u_{ystz,1,t} & u_{ystz,2,t} & \cdots & u_{ystz,m_t,t} \end{pmatrix}_{2stz \times m_t} , \; U_w = \begin{pmatrix} u_{x1,1,w} & u_{x1,2,w} & \cdots & u_{x1,m_w,w} \\ u_{y1,1,w} & u_{y1,2,w} & \cdots & u_{y1,m_w,w} \\ \vdots & \vdots & \ddots & \vdots \\ u_{xk,1,w} & u_{xk,2,w} & \cdots & u_{xk,m_w,w} \\ u_{yk,1,w} & u_{yk,2,w} & \cdots & u_{yk,m_w,w} \\ \vdots & \vdots & \ddots & \vdots \\ u_{xstz,1,w} & u_{xstz,2,w} & \cdots & u_{xstz,m_w,w} \\ u_{ystz,1,w} & u_{ystz,2,w} & \cdots & u_{ystz,m_w,w} \end{pmatrix}_{2stz \times m_w} \tag{4.18}$$

Eq. (4.16) becomes:

$$\begin{cases} \ddot{\mathbf{\Gamma}}_t(t) + 2\zeta_t \omega_t^2 \dot{\mathbf{\Gamma}}_t(t) + \omega_t^2 \mathbf{\Gamma}_t(t) = U_t^T \mathbf{F}_{t,xy}(t) \\ \ddot{\mathbf{\Gamma}}_w(t) + 2\zeta_w \omega_w^2 \dot{\mathbf{\Gamma}}_w(t) + \omega_w^2 \mathbf{\Gamma}_w(t) = -U_w^T \mathbf{F}_{t,xy}(t) \end{cases} \tag{4.19}$$

By Cauchy transformation, the Eq. (4.19) is written as:

$$\dot{\mathbf{\Theta}}(t) = \mathbf{R}_1 \mathbf{\Theta}(t) + \mathbf{R}(t)\mathbf{\Theta}(t) + \mathbf{O}(t)\mathbf{\Theta}(t-\tau) \tag{4.20}$$

where $\mathbf{\Theta}(t) = \begin{pmatrix} \mathbf{\Gamma}_t(t) \\ \mathbf{\Gamma}_w(t) \\ \dot{\mathbf{\Gamma}}_t(t) \\ \dot{\mathbf{\Gamma}}_w(t) \end{pmatrix}_{2(m_t+m_w)\times 1}$, $\mathbf{R}_1 = \begin{pmatrix} \mathbf{0} & \mathbf{I} \\ -\omega_{rd}^2 & -2\zeta\omega_{rd} \end{pmatrix}_{2(m_t+m_w)\times 2(m_t+m_w)}$, $\omega_{rd} = \begin{pmatrix} \omega_t \\ \omega_w \end{pmatrix}$,

$\mathbf{R}(t) = \begin{pmatrix} \mathbf{0} & \mathbf{0} \\ \begin{bmatrix} U_t^T \\ -U_w^T \end{bmatrix}\Delta bC(t) & \begin{bmatrix} U_t^T \\ -U_w^T \end{bmatrix}\Delta bE(t) \end{pmatrix}_{2(m_t+m_w)\times 2(m_t+m_w)}$, and $\mathbf{O}(t) = \begin{pmatrix} \mathbf{0} & \mathbf{0} \\ -\begin{bmatrix} U_t^T \\ -U_w^T \end{bmatrix}\Delta bC(t) & \mathbf{0} \end{pmatrix}_{2(m_t+m_w)\times 2(m_t+m_w)}$;

ω_{rd} is the natural frequency matrix, ω_t is the natural frequency of milling tool and ω_w natural frequency of workpiece.

As the process damping effect is considered, the state-space equation contains two periodic-coefficient matrices $\mathbf{R}(t)$ and $\mathbf{O}(t)$. Based on the updated full-discretization method proposed in Chapter 2 and Ref [9], the method can be modified to solve the state space Eq. (4.20) with multiple modes. First, the third order Newton interpolation polynomials were used to approximate the state terms $\mathbf{\Theta}(t)$ and delayed terms $\mathbf{\Theta}(t-\tau)$, and then the periodic-coefficient matrices $\mathbf{R}(t)$ and $\mathbf{O}(t)$ were obtained by adopting the first order Newton interpolation polynomials, which matches well with the SDM method in the following section.

Based on the proposed dynamic model and calculation method of IPW, the three-dimensional SLD was established and the whole process was summarized in Fig. 27.

Step 1. Define the cutter-location points along the machining path as *steps* (*i=1,2,...steps*) and cutter-contact points along the axial depth as *stz* (*k=1,2,...stz*);

Step 2. Analyze the initial workpiece with the finite element software and obtain the element mass and stiffness matrices;

Step 3. Determine the elements to be removed at the ith step and k^{th} depth of cut and then assemble the variable matrices ΔM_w and ΔK_w;

Step 4. Find the nearest node of the IPW from the tool point and extract the mode shapes and natural frequency from tool-workpiece contact zone;

Step 5. Iterate over entries in cell array within for loops and establish SLD by using the updated full-discretization method.
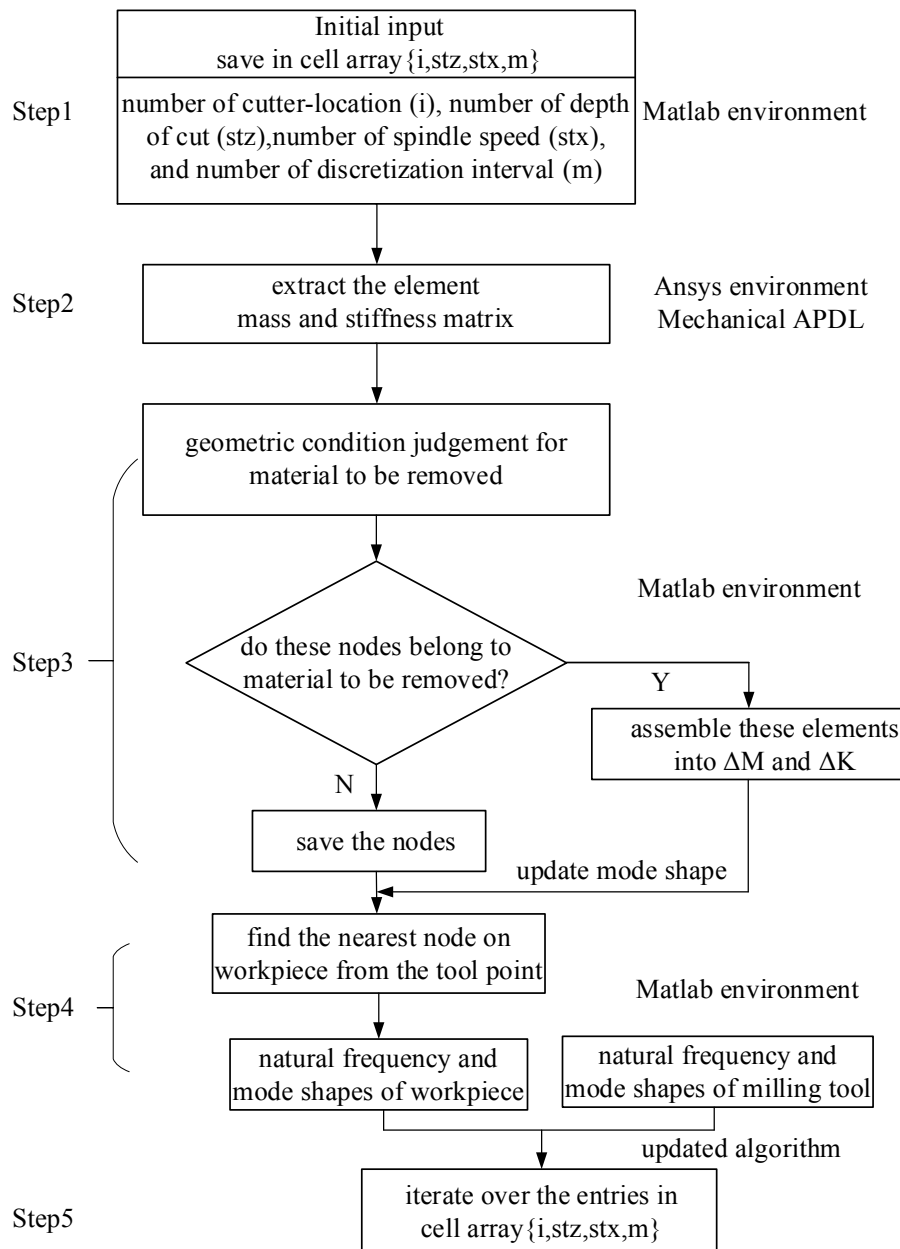
Fig. 27 Procedure for developing three-dimensional SLD of IPW

It could be seen that the nodes of the milling tool did not necessarily coincide with the nodes of the workpiece from Fig. 25. Therefore, it was necessary to determine the nearest node from the differential element of the tool point. In Step 4, the nearest node on the workpiece from the tool point (x_{tp}, y_{tp}, z_{tp}) would be identified:

$$\min\left(\left\|(x_{nw}, y_{nw}, z_{nw}) - (x_{tp}, y_{tp}, z_{tp})\right\|\right) \tag{4.21}$$

The index of the nearest node could be found in the mapping coordinate, and then the mode shape of this node was determined with considering material removal effect.

Since the dynamics of the machine tool and workpiece was required for the analysis of flexible system, the hammer tests were performed for tool point and workpiece respectively [7]. For the milling tool, the direct response of X and Y direction was regarded as the FRF of the rotational tool system, and the cross response was ignored. The impulse hammer was applied from feed and normal directions with the tool discretized equidistantly in Fig. 28. When the tool point was excited at coordinate 1, the displacements were measured at the following three points in two directions. The response in feed direction and normal direction were presented in Figs. 29 and 30 respectively. The identification of modal parameters was mainly based on oscillator model of machine tool and evolutionary algorithm from Ref [97], [98], and the modal parameters identified in feed and normal directions were given in Tab. 4. As the tool-spindle was approximated to a symmetric system, the measured response of tool point along in X and Y directions were pretty close to each other. According to the test results, the frequency around 3100Hz and 3800Hz were the most flexible modes, i.e., these two modes of cutting tool, which were most likely to show the chatter and used for the prediction of the dynamic equation.
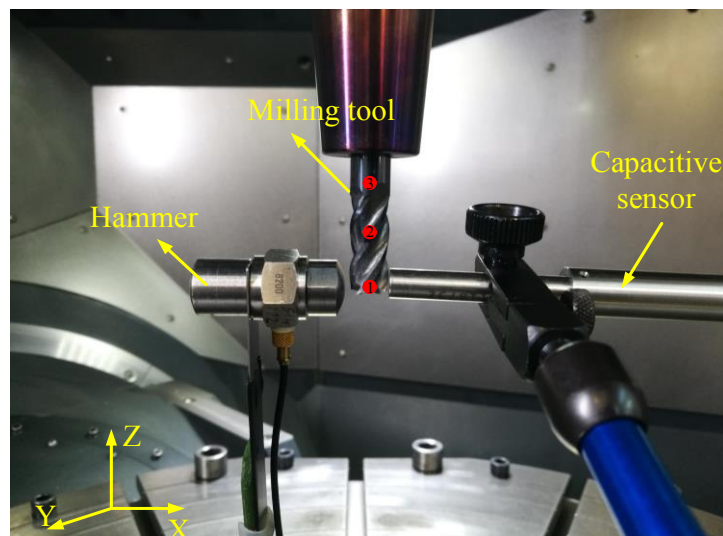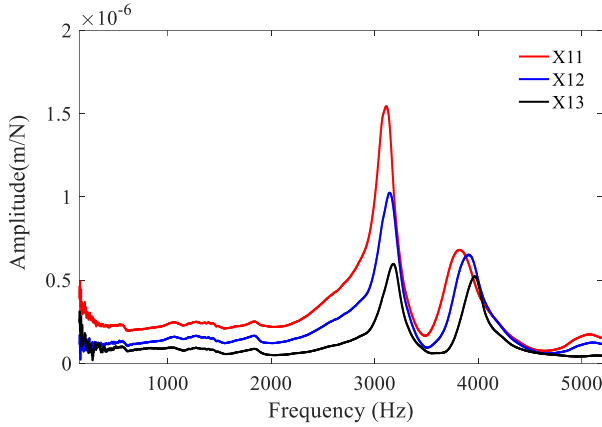

Fig. 28 Measurement for FRF along the Z axis.

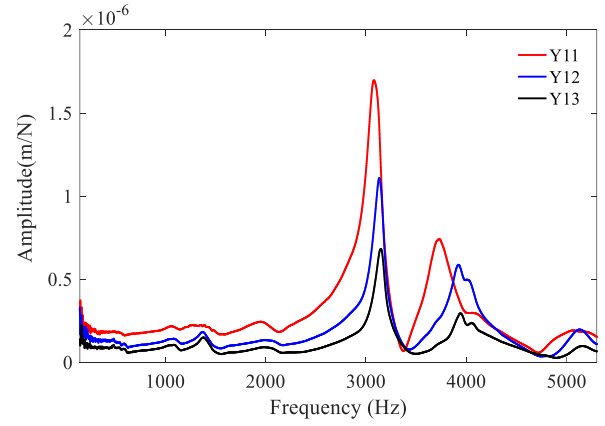Fig. 29 Measured FRF in feed direction

Fig. 30 Measured FRF in normal direction

Table 4 Modal parameters of milling tool in feed and normal directions

Directions	Number of modes	Natural frequencies (Hz)	Damping ratio (%)	Normalized mode shape size($1/\sqrt{kg}$)
Feed direction	1	3122	2.5	[2.56 1.70 0.98]
	2	3814	2.8	[1.24 1.15 0.95]
Normal direction	1	3165	2.1	[2.83 1.82 1.13]
	2	3873	2.6	[1.35 1.07 0.54]
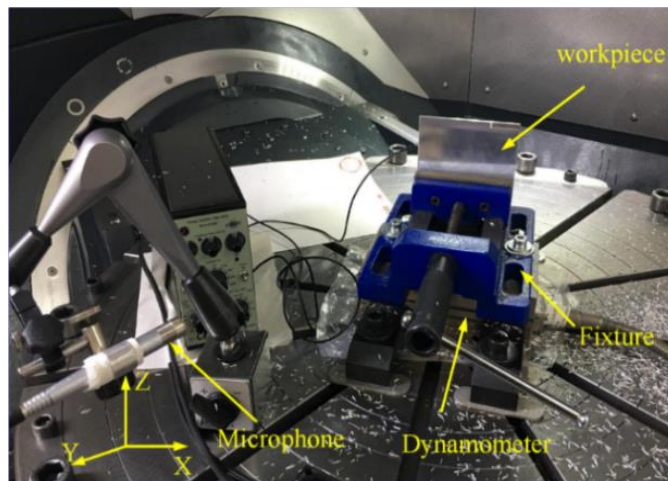
Fig. 31 Machining setup

In order to verify the proposed model, up milling tests were carried out on a five-axis milling machine tool (DMU80 monoBLOCK by DMG MORI Co., Ltd.). The milling tool was a four-fluted carbide end mill with diameter of 10 mm. The free tool overhang length for machining is 40 mm, and the helix angle of the milling tool was 30°. As shown in Fig. 31,

with the microphone set at the vertical position in the direction of the tool path, the workpiece was mounted on the dynamometer (KISTLER 9257B) by the fixture, and the dynamometer was fixed on the working table.

Before developing the SLD, the cutting coefficients should be calibrated by slotting. The linear cutting force model was employed to calibrate the cutting force coefficients [34], and the fitting line of cutting force was obtained by linear regression procedure. In order to display the results in the first quadrant, the absolute value of mean force was used to calculate the fitting results. The feed per tooth were set from 0.04 mm to 0.20 mm with the increment 0.04 mm (See Tab. 5). Then the cutting force coefficients would be determined from the slope and intercept in Fig. 32: K_t=8.9×10^8 Pa, K_r=2.4×10^8 Pa, K_{te}=2.1×10^3 N/m, and K_{re}=3.05×10^3 N/m. The measured value of the flank wear width was 80 μm, and the indentation coefficient is K_{pd}=1×10^{13} N/m^3 [38]. The scanning range of axial depth of cut was from 0 mm to 6 mm, and the spindle speed was set from 2500 rpm to 5500 rpm with the feed per tooth 0.04 mm/tooth. The discretization number for cutter-location, depth of cut, spindle speed and time delay are: 20, 30, 40 and 40 respectively.

Table 5 Machining parameters for milling force coefficients identification

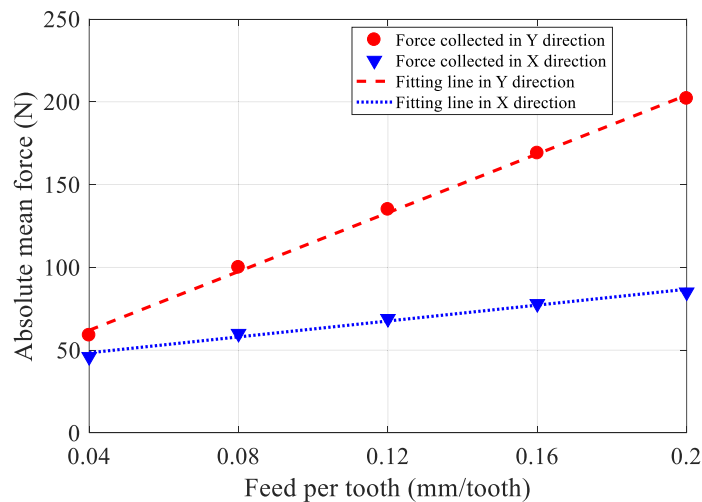| Spindle speed (rpm)	Axial depth of cut (mm)	Feed per tooth (mm)	Mean force in x direction (N)	Mean force in y direction (N)
5000	1	0.04	46	59
5000	1	0.08	60	100
5000	1	0.12	69	135
5000	1	0.16	78	169
5000	1	0.20	85	202

Fig. 32 Fitting results of cutting force coefficients

It should be noted that the calibration of cutting force coefficients needs to be carried out under the condition of stable milling. Therefore, the workpiece with larger geometric dimensions or small free overhang length was selected to improve the rigidity of workpiece clamped in the fixture. Besides, the smaller axial depth of cut was employed to ensure the smooth machining process.

Along the tool path, the mode shapes of workpiece were different from position to position, which led to the different dynamic response. As the vibration modes of workpiece along tool path were unknown, it was nearly impossible to identify which modes would be excited before machining, which led us to consider the first three mode shapes simultaneously. Then the modified third-order updated full discretization method was applied to scan all the machining steps, spindle speeds and axial depth of cut to establish the three-dimensional SLD. Figs. 33-35 illustrated three three-dimensional SLDs: with material removal and process damping, without material removal and without process damping.
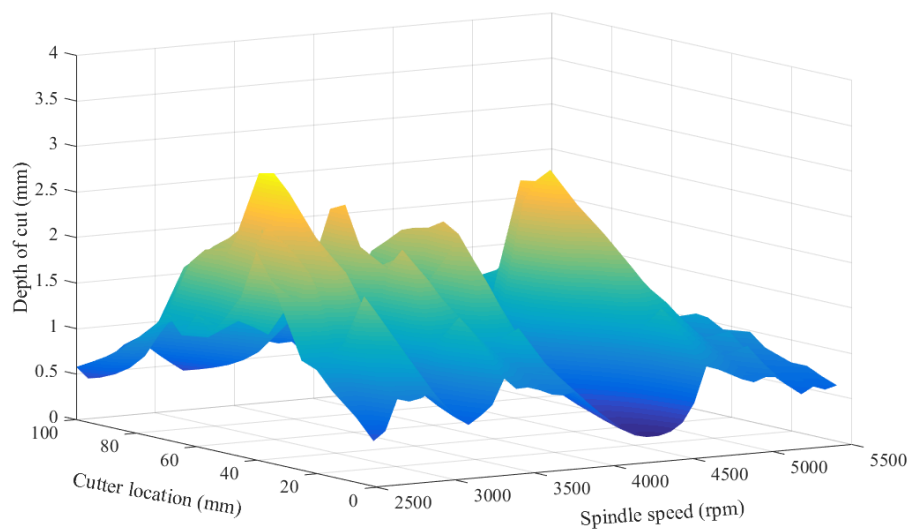

Fig. 33 Comprehensive three-dimensional SLD with material removal and process damping
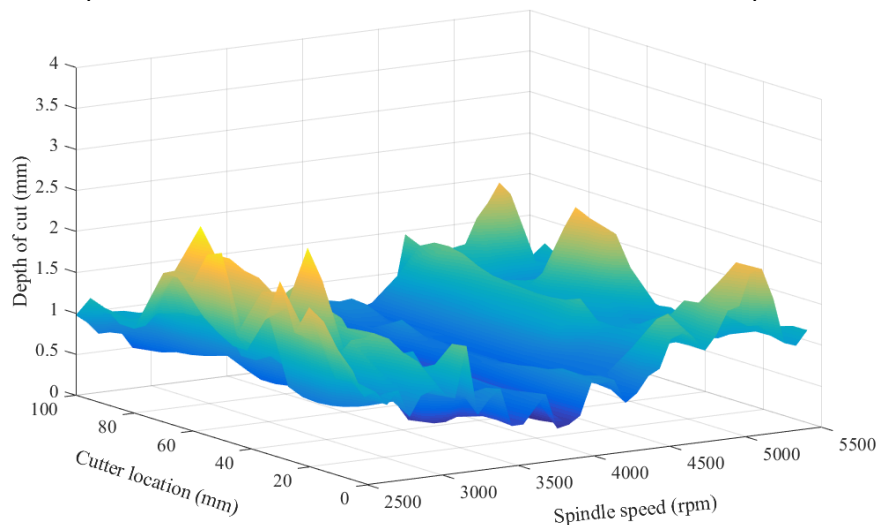

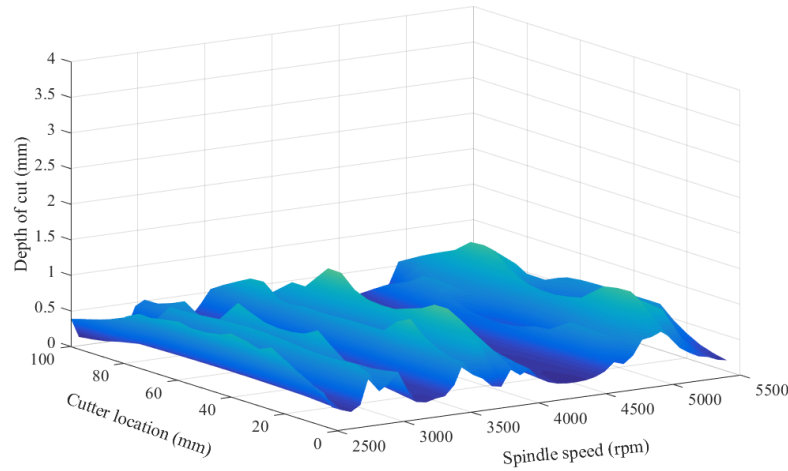Fig. 34 Three-dimensional SLD without material removal

Fig. 35 Three-dimensional SLD without process damping

It should be noted that unstable islands would appear in the SLD with the helix angle considered, which causes inconvenience for the construction of three-dimensional SLD. Therefore, a new function was introduced in Matlab, and the larger critical value of depth of cut was selected as the stability boundary to eliminate the influence of unstable islands. Because the critical depth of cut dominated by the workpiece was smaller, the axial depth of cut needs smaller discrete scanning value. Once the process damping was considered, the critical depth of cut would become larger. Owing to the use of cell arrays, too many discrete values would slow down the calculation time, while too few discrete values may miss the critical value. The SLD developed with multiple modes of the machining system simultaneously is equivalent to the SLD established with multiple single mode envelopment of the machining system separately [18]. The mode shapes only expressed the relative relations of coordinates, so the mode shapes of milling tool can be enlarged proportionally. Nevertheless, the maximum mode shapes of the milling tool should not exceed the mode shapes of the workpiece employed in the calculation. As a result, "holes" in the final 3D-SLD can be avoided due to the lack of critical value. When the milling tool dominated the machining process, the normalized mass mode shapes obtained by measurement must be applied.

4.2.2 Frequencies during machining process

The stable frequencies of the machining process contained the damped natural frequency (f_d , in Hz) of system, the spindle frequency (f_{sp} , in Hz) and the tooth passing frequency (f_{tp} , in Hz). These frequencies were associated with free vibration and forced vibration, and they would always appear during the processing. They can be defined as:

$$f_d = \frac{\omega_r}{2\pi}\sqrt{1-\xi^2} \qquad f_{sp} = \frac{k\Omega}{60}, \; k=1,2,3,\cdots \qquad f_{tp} = \frac{kN\Omega}{60}, \; k=1,2,3,\cdots \tag{4.22}$$

where ω_r is the undamped natural frequency.

In the actual milling process, the runout of the milling tool was inevitable. According to the research of Insperger [99], [100], the chatter frequencies can be divided into three kinds with runout effect: quasi-periodic chatter (f_h, in Hz), period one frequency (f_{p1}, in Hz) and period doubling frequency (f_{p2}, in Hz). The quasi-periodic chatter corresponded to Hopf bifurcation, period one frequency corresponded to saddle-node bifurcation and period doubling frequency corresponded to flip bifurcation. These frequencies can be written as:

$$f_h = f_c + \frac{k\Omega}{60}, \; k=0,1,2,3,\cdots \quad f_{p1} = \frac{k\Omega}{60}, \; k=1,2,3,\cdots \quad f_{p2} = \frac{\Omega}{120} + \frac{k\Omega}{60}, \; k=0,1,2,3,\cdots \tag{4.23}$$

where f_c is the chatter frequency.

It is worth noting that the period one frequency is as equal as the spindle frequency. Therefore, the frequency spectrum cannot completely reflect the occurrence of chatter when only the spindle frequency appears. In this case, chatter needs to be comprehensively determined with the assistance of experimental results. Otherwise, this kind of frequency should be viewed as spindle frequency.

4.3 Cutting tests and discussion

As shown in Figs. 36 and 37, the two-dimensional SLDs along the tool path at 3500 rpm and 5000 rpm were intercepted from the comprehensive three-dimensional SLDs (Fig. 33) respectively.
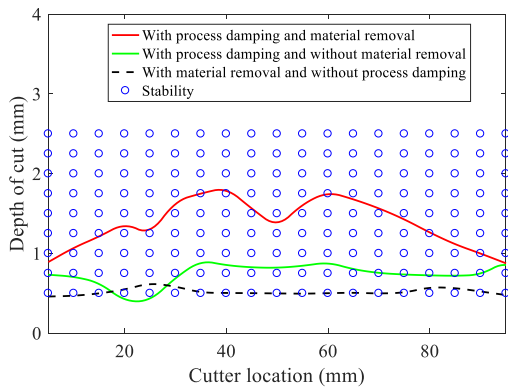

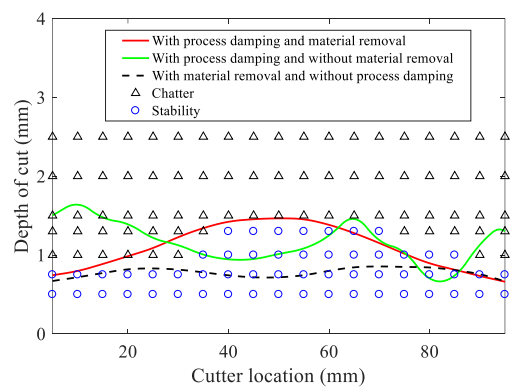Fig. 36 SLD at the spindle speed of 3500 rpm   Fig. 37 SLD at spindle speed of 5000 rpm

As given in Fig. 36, it should be noted that the process was still stable when the axial depth of cut was greater than the maximum critical value of 2 mm at the spindle speed of 3500 rpm. At this spindle speed, the feed velocity was 9.33 mm/s, and the fundamental frequency was 58.33 Hz. During the machining process, it is uncertain which mode of the system would be excited, so the process of signal acquisition was divided into two steps. The first step was to observe the machining state of the workpiece when it was processed to the middle position, i.e. from N1 to N2 along X direction (Fig. 17), and then the rest of the material was removed, i.e. from N2 to N3 along X direction, which can not only determine whether the chatter occurred but also check whether the machining signal was collected. Compared with the spectrum of cutting force, the spectrum of sound signal contains more frequency components and more possible chatter frequencies could be found. Therefore, the microphone was used to collect the sound signal. However, there is still some other noise in the sound signal, especially when the chatter is not severe, which brings a great challenge to chatter identification. It is not suitable for all machining situation to determine whether the chatter occurs only by depending on the frequency in the sound spectrum. If the chatter frequency was identified strictly as defined in Eq. (4.23), the chatter frequency meeting the definition could be found even during stable machining. When the adjacent frequencies were very close to each other, the noise frequency and chatter frequency were more difficult to distinguish. If the sound signal was filtered directly by using the function of 'smooth' in Matlab, it was likely to remove some chatter frequencies as well; if the chatter frequencies were identified directly, the workload was large and the uncertainty was high. Therefore, the spectrum cannot be used as the only indicator of the chatter occurrence during the validation process for SLD, and chatter occurrence needs to be further judged comprehensively with the assistance of surface topography of workpiece.

Figs. 38 and 39 display the sound signal and the corresponding spectrum collected during the machining process at the spindle speed of 3500 rpm and depth of cut of 16 mm. It can be seen from the time domain that the sound signal was relatively stable and there was no obvious fluctuation. The spectrums for the three stages in Fig. 39 were derived from partial time-domain signal of three machining stages in Fig. 38 with the fast Fourier transform respectively (same as Fig. 47, the interval of sampling time was 3.05×10^{-5}s). In the spectrum, the grid interval in X direction was set according to the fundamental frequency of the spindle speed. Each grid represented twice the spindle speed. When the frequency value was located on the grid line or in the middle of a single grid, the frequency was the harmonic frequency of the spindle speed. There were no period doubling frequency and Hopf bifurcation frequency

in the spectrum. Since the period one frequency was as same as that of the spindle speed, it was necessary to use the experimental results to determine whether the chatter occurs or not. As shown in Fig. 40, the surface topography of the machined workpiece (measured by nanofocus®) was regular and no vibration marks appeared. Only some regular grooves linked to the helix angle can be observed, but they did not belong to chatter marks. Therefore, there was no chatter occurrence along the tool path, when the axial depth of cut was 16 mm.
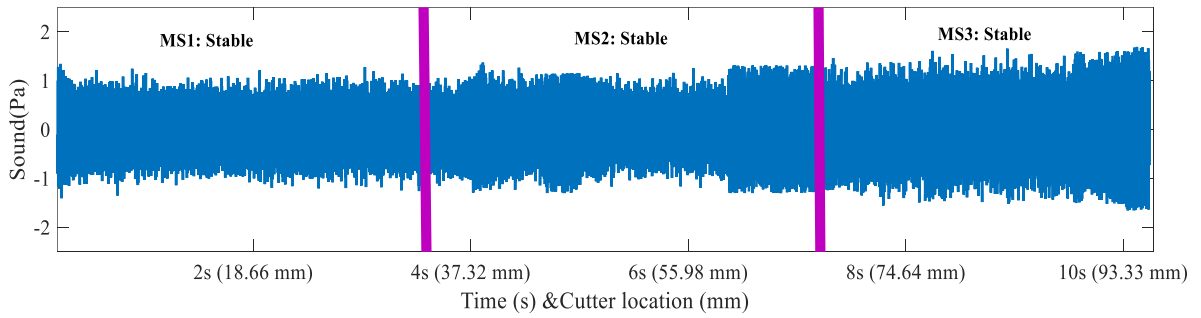
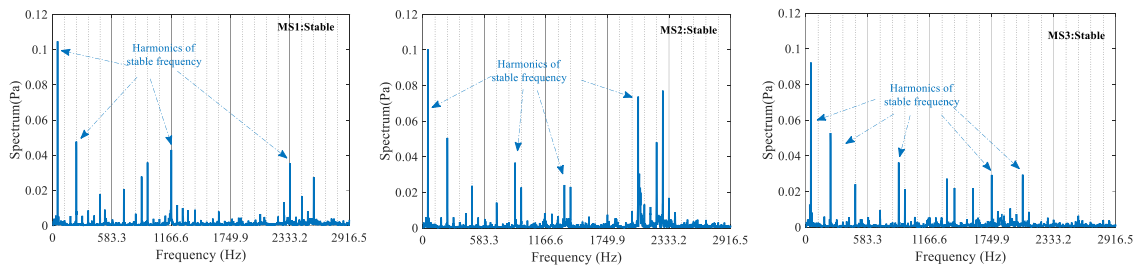Fig. 38 Measured sounds for the machining parameter (3500 rpm, 16 mm)

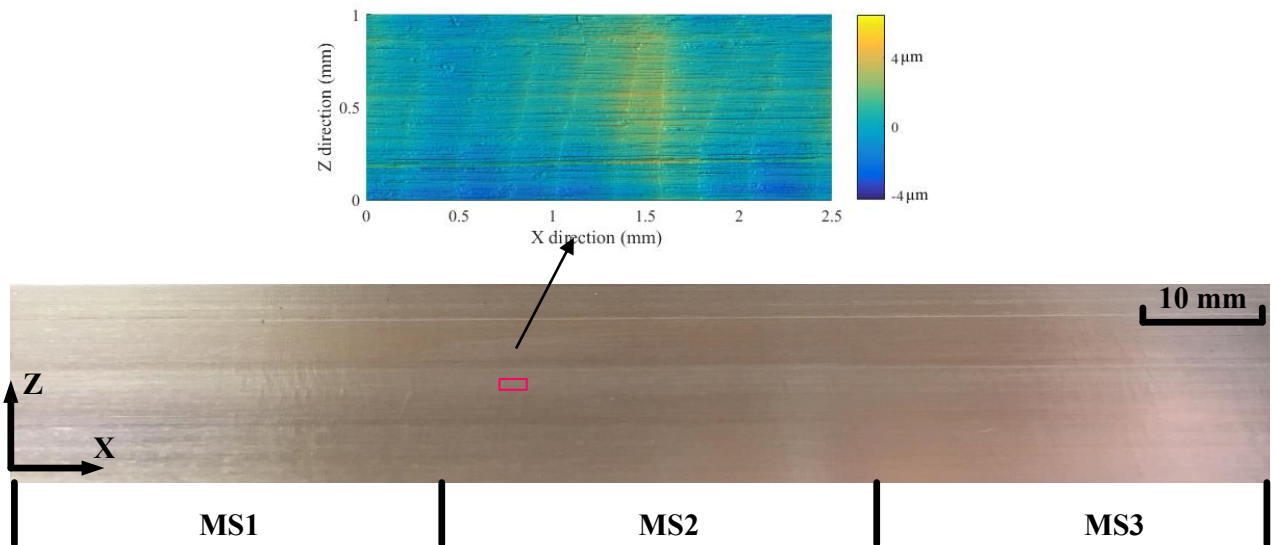Fig. 39 Frequency spectrum for the machining parameter (3500 rpm, 16 mm)

Fig. 40 Surface topography of workpiece for the machining parameter (3500 rpm, 16 mm)

The modal characteristics of the workpiece in this situation did not affect the stability of the system. Therefore, the SLD only considering the modal characteristics of the tool was established, as presented in Fig. 41.
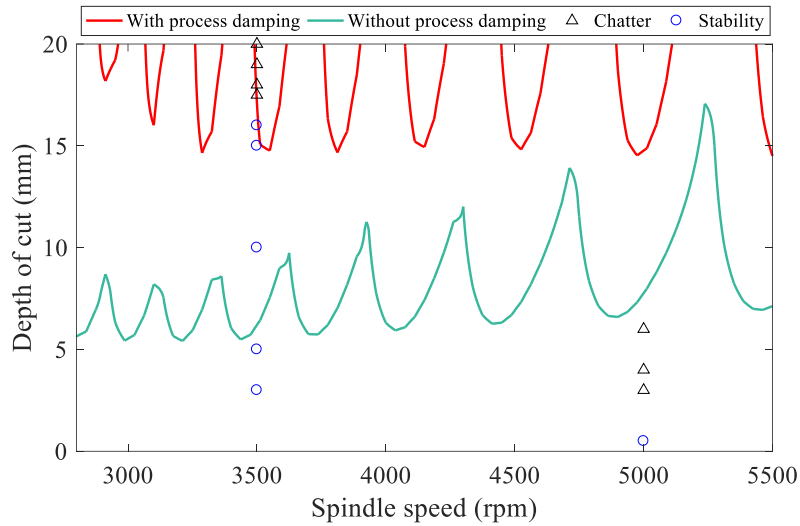
Fig. 41 SLD with only considering modes of milling tool

The SLD considering process damping at 3500 rpm was in good agreement with the experimental results. Figs. 42 and 43 present the sound signal and spectrum from 60 mm to 80 mm at spindle speed of 3500 rpm and depth of cut of 20 mm. Compared with depth of cut of 16 mm, the sound signal in time domain showed irregular distribution, and the surface topography of the machined workpiece was irregular with large chatter grooves appearing (see Fig. 44). The frequency spectrum demonstrated that period doubling frequency and Hopf bifurcation frequency appeared, and the Hopf bifurcation frequency was the dominant frequency. The Hopf bifurcation frequency was very close to the first order frequency of the milling tool instead of the third order of workpiece. Besides, the stability did not change along the tool path, which indicated that the modes of the workpiece did not work and the mode of milling tool was indeed stimulated.
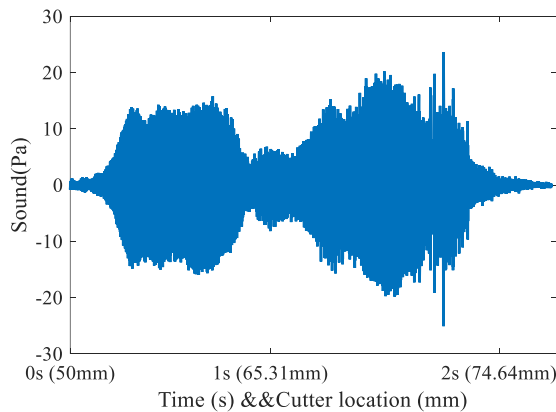

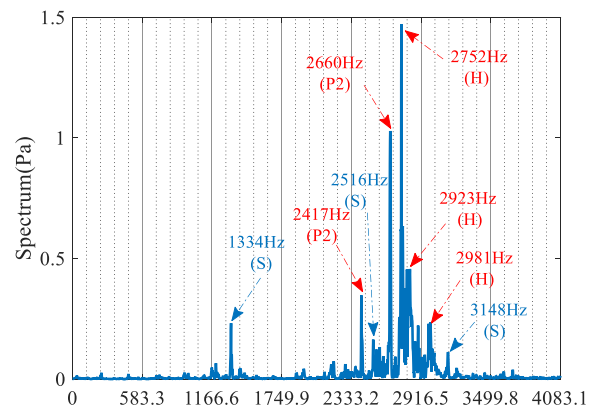Fig. 42 Measured sounds for machining parameter (3500 rpm, 20 mm)

Fig. 43 Frequency spectrum for machining parameter (3500 rpm, 20 mm). H: Hopf bifurcation frequency, P2: Period doubling frequency, S: Harmonics of stable frequency
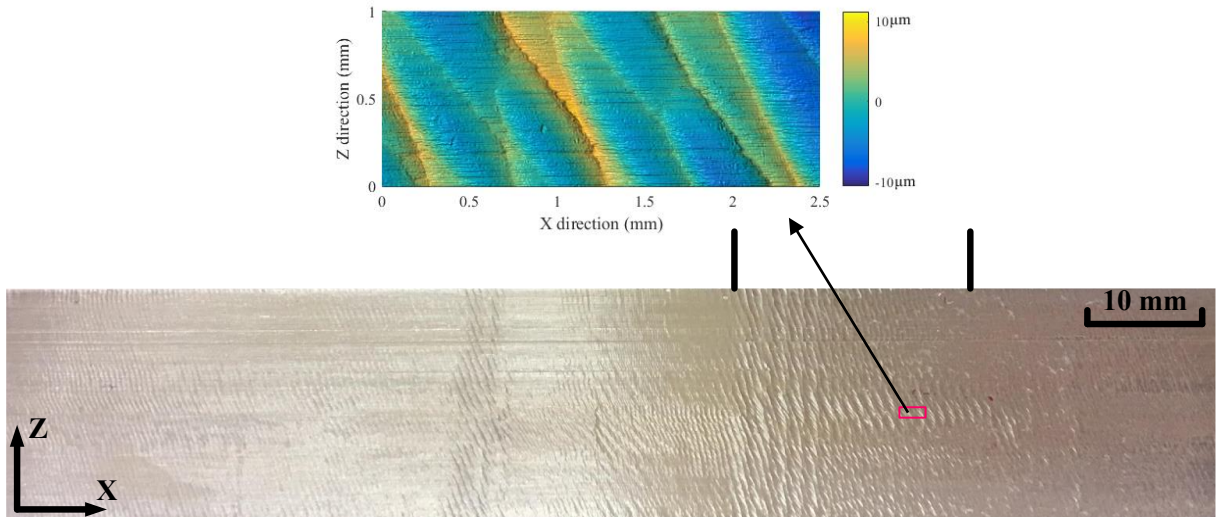
Fig. 44 Surface topography of workpiece for the machining parameter (3500 rpm, 20 mm)

When the milling tool dominated the machining process, the Euler integration can be employed to analyze the displacement of the tool point in the direction of X and Y. The distribution of the sampling point was obtained by the Poincare section [1], which could simulate the bifurcation at a certain machining parameter from the SLD. To improve the efficiency of calculation, only the ploughing force, static and dynamic cutting force were involved to simulate the displacement of the tool point. The simulated result at spindle speed of 3500 rpm and depth of cut of 20 mm was illustrated in Fig. 45. According to the displacement simulation of the milling tool, the sampling points were elliptically distributed in the X and Y directions among [-0.5 mm, 0.5 mm], which was a typical feature of Hopf bifurcation, and the simulation result was in good agreement with the experimental results. The axial depth of cut accorded with the SLD only considering the first two modes of the milling tool, which further verified that the modes of the milling tool played a dominant role in this situation.
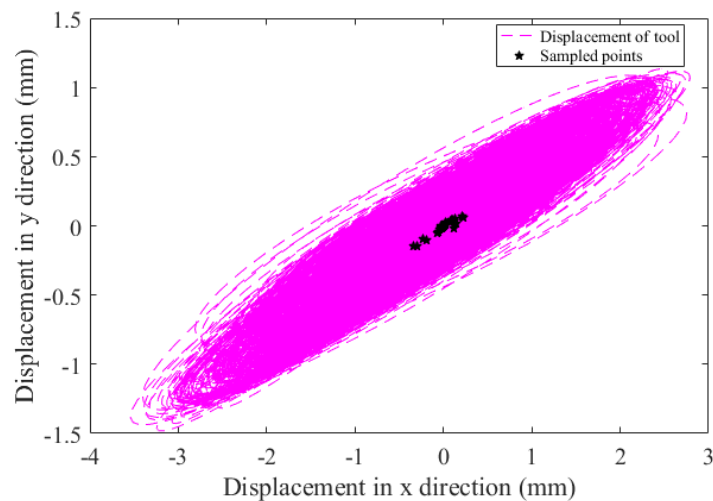

Fig. 45 Poincare section for the machining parameter (3500 rpm, 20 mm)

The experimental results were obviously inconsistent with the SLD only considering the modal characteristics of milling tool at spindle speed of 5000 rpm, which indicated that the modes of milling tool did not dominate the machining process any more. Figs. 46 and 47 display the sound signal and spectrum at spindle speed of 5000 rpm and axial depth of cut of 1 mm. At this spindle speed, the feed velocity was 13.33 mm/s, and the fundamental frequency was 83.33 Hz. The sound signal fluctuated greatly when the milling tool cut in and out of the workpiece in time domain, and the sound signal was relatively flat in the middle part of the workpiece. From the spectrum, it can be seen that the period doubling frequency appeared in the cut-in and cut-out parts, and the chatter frequencies were very close to the first and second order frequency of workpiece. As given in Fig. 48, the corresponding surface topographies of the machined workpiece were shown, and they matched well with the machining spectrum. That demonstrated the modes of workpiece dominated the machining at these two parts. There were no Hopf bifurcation frequency and period doubling frequency in the middle part of the workpiece, which was consistent with the actual machining results as well.
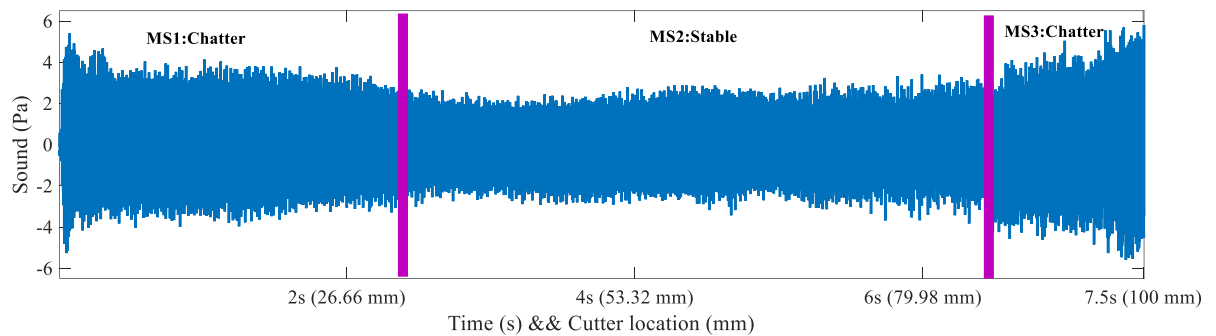

Fig. 46 Measured sounds for the machining parameter (5000 rpm, 1 mm)

The amplitude of the spectrum in Fig. 47 was much lower than that in Fig. 42, which was due to the smaller axial depth of cut. While the amplitude of the spectrum in Fig. 47 was higher than that in Fig. 39 because of the occurrence of chatter. The comprehensive SLD in Fig. 33 was generated by considering the five modes of milling tool and workpiece simultaneously. The minimum value of the axial depth of cut at each discrete spindle speed was used to envelope the SLD for every mode. Therefore, the comprehensive SLD was a conservative diagram. Although the comprehensive SLD would limit the critical depth of cut, it can ensure the processing quality.
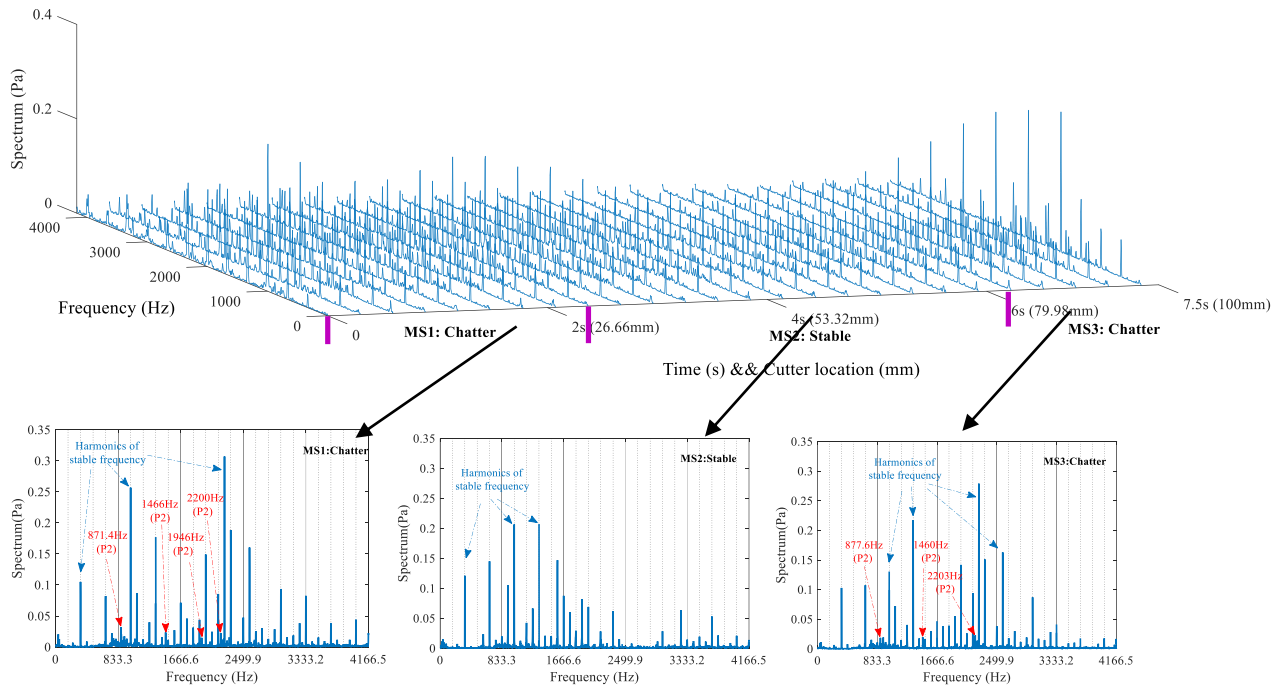
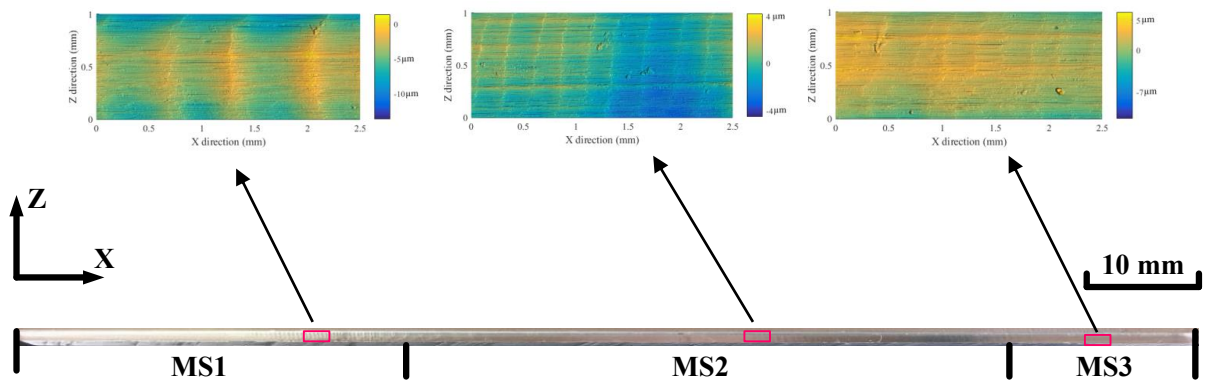Fig. 47 Frequency spectrum for the machining parameter (5000 rpm, 1 mm). P2: Period doubling frequency

Fig. 48 Surface topography of workpiece for the machining parameter (5000 rpm, 1 mm)

As shown in Figs. 49-52, two-dimensional SLDs were intercepted from Figs. 33-35 at cutter locations 20mm, 40mm, 60mm and 80mm, respectively. Although the specific values of the three SLDs were different, they basically had the same upward and downward trend. It can be seen that the depth of cut of SLDs considering process damping and material removal was larger than that without considering process damping. The prediction of comprehensive SLD with process damping and material removal was inaccurate at some points of cut-in and cut-out position, but it was closer to the experimental results than the SLD without considering material removal.
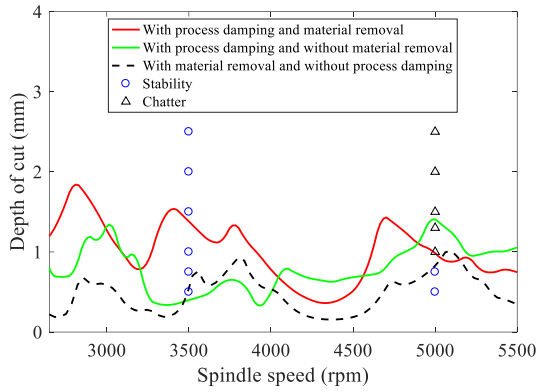
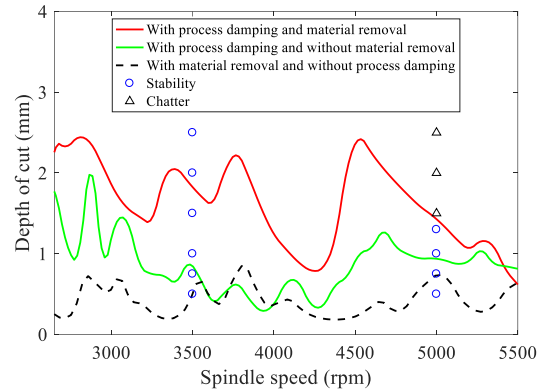Fig. 49 Two-dimensional SLDs at cutter locations of 20mm

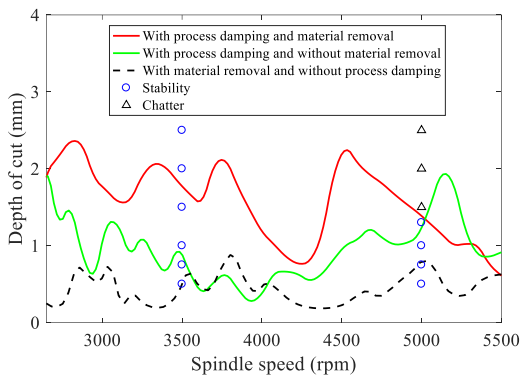Fig. 50 Two-dimensional SLDs at cutter locations of 40mm

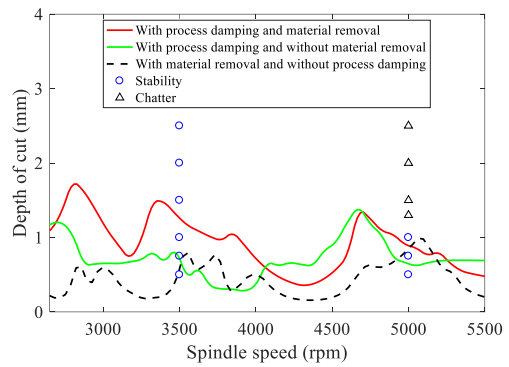Fig. 51 Two-dimensional SLDs at cutter locations of 60mm

Fig. 52 Two-dimensional SLDs at cutter locations of 80mm

As shown in Figs. 49-52, when the process damping was ignored, the critical depth limit of SLD became smaller. While the process damping was considered, the critical depth limit of SLD became larger. The behavior of process damping was similar to the limit cycle oscillation [38]; that was, the process damping would increase with the axial depth of cut synchronously to suppress the chatter. With the further increase of the axial depth of cut, the critical value would be exceeded. The limit cycle would bifurcate from the original equilibrium point and change the stability of the system. Compared with spindle speed of 5000 rpm, the input energy of cutting process at 3500 rpm was relatively small. Coupled with the consumption of vibration energy by process damping, the vibration mode of thin-walled workpiece was not stimulated, so the machining process at this stage was mainly dominated by the milling tool. When the spindle speed increased, the input energy increased as well. Once the multiple modes of thin-walled workpiece were excited, these modes would play a leading role. As the first mode of thin-walled workpiece was relatively small, therefore, the corresponding critical depth of cut was small as well, which would affect the final envelope result. That was why the experimental results were in good agreement with the comprehensive SLD in Fig. 37 at spindle speed of 5000 rpm.

4.4 Summary

In this chapter, a multi-mode model in four spatial dimensions was developed with considering the process damping between milling tool and workpiece, and SDM and FEM were used together to determine the IPW dynamics. Then the mode shapes of in-process thin-walled workpiece and milling tool were introduced to the dynamic equation. Finally, the comprehensive three-dimensional SLD along the tool path was obtained and validated by experimental tests. The proposed model was analyzed in a rigorous framework, and the conclusions can be summarized as follows:

The process damping had the speed dependent property (especially at low spindle speed region), which showed the limit cycle oscillation during the milling process and was further confirmed from the experiment results. During the stability prediction, considering the process damping could improve the critical depth of cut and prediction accuracy. Process damping could consume part of the energy generated by cutting vibration, and it could improve the machining efficiency for weak rigidity workpiece and difficult-to-machine materials. Therefore, process damping is a favorable factor in milling process, and it should be considered in the flexible dynamic model.

In the milling process, especially for the flexible system, the dominant modes of the thin-walled workpiece and milling tool were uncertain. Although the first mode of the workpiece was relatively lower, the modes of the thin-walled workpiece were not necessarily in the dominant state. During the experiments, the modes of milling tool and workpiece as the dominant modes appeared respectively with corresponding chatter frequencies. The SLDs with the proposed model could predict the stability accurately. Especially when the workpiece dominated the machining process, the comprehensive SLD considering material removal was closer to the experimental results. That meant the continuous dynamic change caused by the material removal and cutter position had important effects on the machining stability.

Considering the multiple modes effect would establish a more conservative and reliable comprehensive three-dimensional SLD. Although the material removal efficiency may be limited, stable parameters derived from the conservative SLD can guarantee the stability of the whole machining process.

5 Surface location error prediction for continuous radial milling

5.1 The model of SLE under stable milling process

The dynamics of workpiece would become more and more obvious with material removal during continuous milling. Since process damping effect is not significant in high-speed cutting [34], it is neglected in the milling force model. As illustrated in Fig. 53b, there is no material left along the feed direction, and the SLE in X direction is more difficult to determine than that in Y direction. Therefore, only the SLE in Y direction is considered.

5.1.1 Milling force establishment under stable milling process
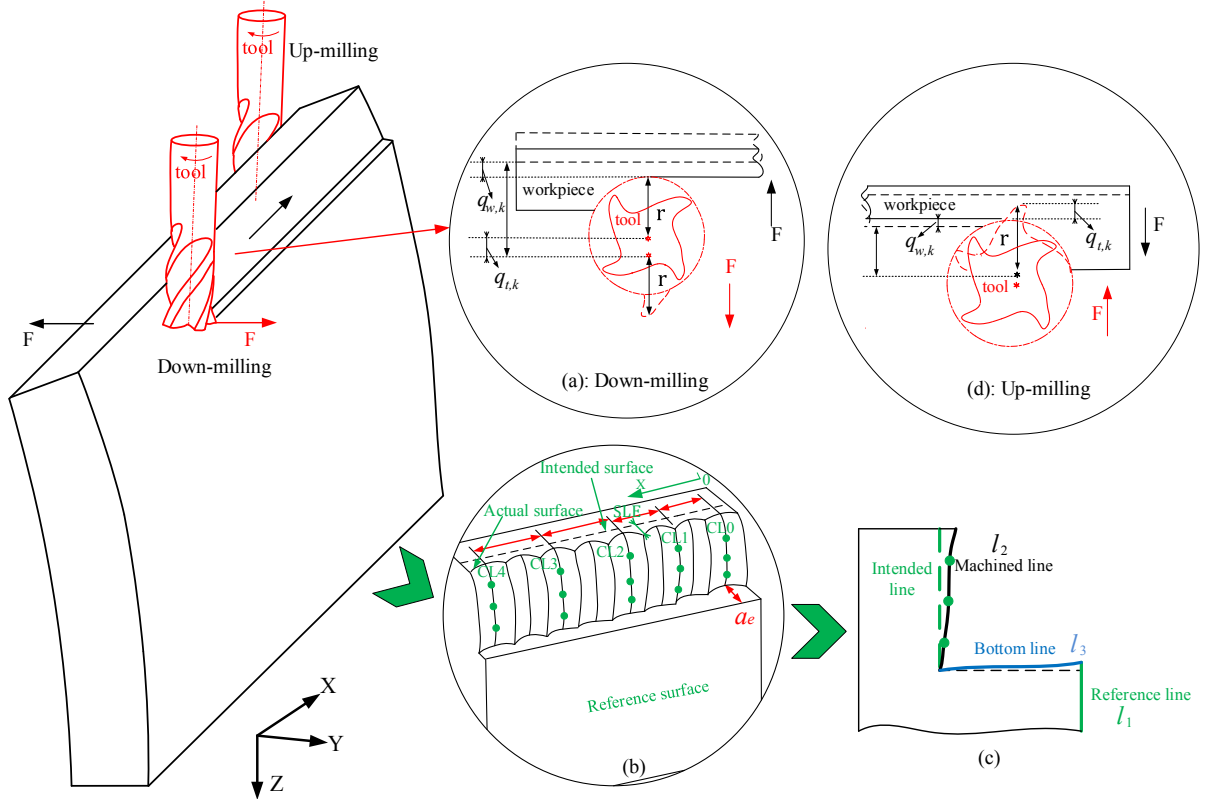
Fig. 53 Schematic model of milling process

As shown in Fig. 54, the tangential force ($F_{t,j}$) and radial force ($F_{r,j}$) for the jth tooth are composed of the shearing terms ($F_{ts,j}$ and $F_{rs,j}$) and ploughing terms ($F_{tp,j}$ and $F_{rp,j}$), and these forces can be written as:

$$\begin{Bmatrix} \mathrm{d}F_{t,j} \\ \mathrm{d}F_{r,j} \end{Bmatrix} = \begin{Bmatrix} \mathrm{d}F_{ts,j} \\ \mathrm{d}F_{rs,j} \end{Bmatrix} + \begin{Bmatrix} \mathrm{d}F_{tp,j} \\ \mathrm{d}F_{rp,j} \end{Bmatrix} = g(\phi_j)\Delta b \left(\begin{Bmatrix} K_t \\ K_r \end{Bmatrix} h_j(t) + \begin{Bmatrix} K_{te} \\ K_{re} \end{Bmatrix} \right) \tag{5.1}$$

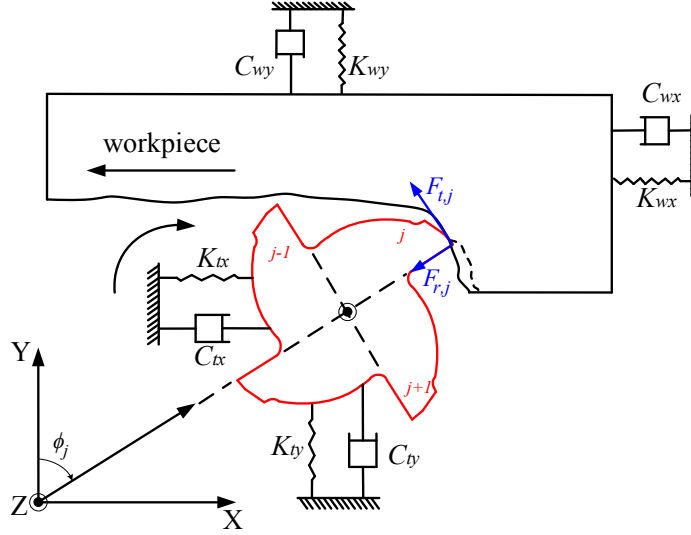Fig. 54 Two degree of freedom model of milling force (up-milling)

After substituting Eqs. (4.1) and (5.1) into Eq. (4.12), the force acting on each slice becomes:

$$dF_{t,k,xy} = \begin{Bmatrix} dF_{t,k,x} \\ dF_{t,k,y} \end{Bmatrix} = b_k A(t) + b_k B(t) + b_k C(t)\left(\left(\mathbf{q}_t(t) - \mathbf{q}_t(t-\tau)\right) - \left(\mathbf{q}_w(t) - \mathbf{q}_w(t-\tau)\right)\right), \quad k = 1, 2 \cdots stz \qquad (5.2)$$

where $\qquad A(t) = \sum_{j=1}^{N} g(\phi_j)\mathbf{W}_j \begin{Bmatrix} K_{te} \\ K_{re} \end{Bmatrix} \qquad , \qquad B(t) = \sum_{j=1}^{N} g(\phi_j)\mathbf{W}_j \begin{Bmatrix} K_t \\ K_r \end{Bmatrix} \sin(\phi_j) f_z \qquad , \qquad$ and

$$C(t) = \sum_{j=1}^{N} g(\phi_j)\mathbf{W}_j \begin{Bmatrix} K_t \\ K_r \end{Bmatrix} [\sin(\phi_j), \cos(\phi_j)].$$

5.1.2 SLE at the contact zone of milling tool

If multiple modes are coupled in Eq. (4.16), the modal coordinate transformation will be employed to decouple these modes. By Cauchy transformation, the Eq. (4.16) is written as:

$$\dot{\mathbf{\Theta}}(t) = \mathbf{R}_1 \mathbf{\Theta}(t) + \mathbf{R}(t)(\mathbf{\Theta}(t) - \mathbf{\Theta}(t-\tau)) + \mathbf{R}_2 \qquad\qquad (5.3)$$

where $\quad \mathbf{\Theta}(t) = \begin{pmatrix} \mathbf{\Gamma}_t(t) \\ \mathbf{\Gamma}_w(t) \\ \dot{\mathbf{\Gamma}}_t(t) \\ \dot{\mathbf{\Gamma}}_w(t) \end{pmatrix}_{2(m_t+m_w)\times 1} \quad , \quad \mathbf{R}_1 = \begin{pmatrix} \mathbf{0} & \mathbf{I} \\ -\omega_{rd}^2 & -2\zeta\omega_{rd} \end{pmatrix}_{2(m_t+m_w)\times 2(m_t+m_w)} \quad , \quad \omega_{rd} = \begin{pmatrix} \omega_t \\ \omega_w \end{pmatrix} \quad ,$

$\mathbf{R}_2 = \begin{pmatrix} \mathbf{0} \\ \begin{bmatrix} U_t^T \\ -U_w^T \end{bmatrix} \Delta b(A(t)+B(t)) \end{pmatrix}_{2(m_t+m_w)\times 1}$, and $\mathbf{R}(t) = \begin{pmatrix} \mathbf{0} & \mathbf{0} \\ \begin{bmatrix} U_t^T \\ -U_w^T \end{bmatrix} \Delta b C(t) & \mathbf{0} \end{pmatrix}_{2(m_t+m_w)\times 2(m_t+m_w)}$.

As the static force is included in force model of the dynamic equation, then Eq. (2.6) becomes

$$\mathbf{x}(t) = e^{\mathbf{A}_0(t-ih)}\mathbf{x}(ih) + \int_{ih}^{t} e^{\mathbf{A}_0(t-s)}\mathbf{B}(s)[\mathbf{x}(s) - \mathbf{x}(s-T)]ds + \int_{ih}^{t} e^{\mathbf{A}_0(t-s)}\mathbf{f}(s)ds \tag{5.4}$$

Consequently, Eq. (5.4) can be rearranged equivalently as

$$\mathbf{x}(ih+h) = e^{\mathbf{A}_0h}\mathbf{x}(ih) + \int_0^h e^{\mathbf{A}_0s}[\mathbf{B}(ih+h-s)[\mathbf{x}(ih+h-s)-\mathbf{x}(ih+h-s-T)]ds + \int_0^h e^{\mathbf{A}_0s}\mathbf{f}(ih+h-s)ds \tag{5.5}$$

By the method of first-order interpolation, the term of $\mathbf{f}$ ($ih+h-s$) can be written as

$$\mathbf{f}(ih+h-s) \approx \mathbf{f}_{i+1} + \frac{(\mathbf{f}_i - \mathbf{f}_{i+1})s}{h} \tag{5.6}$$

Then the mapping relation between current period and immediate previous period can be developed as

$$\mathbf{x}_{i+1} = \mathbf{P}_i \begin{bmatrix} (\mathbf{F}_0 + \mathbf{M}_{11}^i)\mathbf{x}_i + \mathbf{M}_{12}^i\mathbf{x}_{i-1} + \mathbf{M}_{13}^i\mathbf{x}_{i-2} \\ +\mathbf{M}_{1,(n+1)}^i\mathbf{x}_{i-n} + \mathbf{M}_{1,n}^i\mathbf{x}_{i-n+1} + \mathbf{M}_{1,(n-1)}^i\mathbf{x}_{i-n+2} \\ +\mathbf{M}_{1,(n-2)}^i\mathbf{x}_{i-n+3} + \mathbf{G}_i \end{bmatrix} \tag{5.7}$$

where $\mathbf{G}_i = \mathbf{F}_1\mathbf{f}_{i+1} + \mathbf{F}_2\dfrac{(\mathbf{f}_i - \mathbf{f}_{i+1})}{h}$

Based on the third-order updated full-discretization method [9], Eq. (5.3) could be decoupled and solved. The stability and SLE of the system could be extracted from the fixed point of the steady-state vector [32], [47]. Finally, the SLE becomes:

$$f_{SLE} = (\mathbf{I} - \mathbf{\Phi})^{-1}\mathbf{G} \tag{5.8}$$

where $\mathbf{G} = \mathbf{M}_{n,c}\mathbf{G}_n + \sum_{i=1}^{n-1}(\mathbf{M}_n\mathbf{M}_{n-1}\cdots\mathbf{M}_{i+1}\mathbf{M}_{i,c}\mathbf{G}_i)$, and $\mathbf{I}$ is the identity matrix.

The relative displacement between tool and workpiece at contact zone is the main cause of SLE. As illustrated in Fig. 53(a), the relative displacement of the kth slice for the down milling can be expressed as:

$$q_r(b_k) = q_{r,k} = q_{t,k} + q_{w,k} \quad k = 1, 2, \cdots, stz \tag{5.9}$$

where $q_{t,k}$ is the displacement of the milling tool for the kth slice, $q_{w,k}$ is the displacement of the workpiece for the kth slice, and $q_{r,k}$ is the relative displacement for the kth slice.

From the perspective of FRF, the sum of displacement responses of tool and workpiece constitutes the relative FRF, i.e. $H_{r,k}(\omega)$. Then Eq. (5.9) becomes:

$$H_{r,k}(\omega) = \frac{q_{r,k}}{F} = \frac{q_{t,k}}{F_{t,k,xy}} + \frac{-q_{w,k}}{-F_{w,k,xy}} = H_{t,k}(\omega) + H_{w,k}(\omega) \quad k = 1, 2, \cdots, stz \tag{5.10}$$

where $H_{t,k}(\omega)$ is the FRF of the milling tool, and $H_{w,k}(\omega)$ is the FRF of the workpiece.

Eq. (5.9) is the expansion form of Eq. (4.17) in physical coordinates. Eq. (5.10) is the expansion form of Eqs. (4.17) and (5.9) in frequency domain, which considers the dynamics of milling tool and workpiece comprehensively.

5.2 Exclusion of unstable machining parameters

5.2.1 Unstable parameters caused by regenerative effect

Considering multiple vibration modes of milling tool and workpiece can reflect the practical state of the system. When chatter occurs, the system may be dominated either by multiple modes of milling tool or workpiece. In order to obtain stable parameters, dynamic characteristics of milling tool and workpiece need to be taken into account at the same time. In fact, it is necessary to introduce the mode shapes of the IPW along the toolpath when the modal vibration of the workpiece is considered. In order to obtain a more conservative SLD and improve the computational efficiency, the maximum mode shapes of a certain mode are extracted and regarded as the mode shapes of the whole workpiece. Meanwhile, the minimum frequency at each cutter location from IPW is needed to construct the SLD as well. Without loss of generality, the maximum mode shapes and minimum frequencies of the workpiece are defined as follows：

$$\Psi_i = \max\left\{\psi_{i,1},\ \psi_{i,2},\cdots\psi_{i,m_w}\right\},\ \ \omega_i = \min\left\{\omega_{i,1},\ \omega_{i,2},\cdots\omega_{i,m_w}\right\} \tag{5.11}$$

where i is the discrete step of the workpiece along the tool path.

5.2.2 Unstable parameters caused by cumulative effect

With respect to continuous milling, each immersion would generate a SLE, which is viewed as a small perturbation of equilibrium limit cycle. The small perturbation accumulates continuously, and the cumulative value is the cumulative surface location error (CSLE). Due to the non-linear characteristics of the SLE, the CSLE may converge to a specific value. Otherwise, the CSLE diverges, which will destabilize the limit cycle. This depends on the initial condition, i.e. radial depth of cut a_e. According to the definition of CSLE [101], the final value is the stable fixed point after iterations, and the CSLE can be written as

$$\begin{cases} SLE = f(a_e/\mathrm{D}),\ SLE_{n+1} = f(\dfrac{a_e}{D}+\dfrac{SLE_n}{D}) \\ \qquad CSLE = f(\dfrac{a_e}{D}+\dfrac{CSLE}{D}) \end{cases} \tag{5.12}$$

5.3 SLE analysis during stable machining stage

5.3.1 Effect of clamping system on frequency of workpiece

The mode shapes of the milling tool were obtained by means of experimental measurements, and three measuring points were set equidistantly along the tool length. Frequency responses of three points were measured in feed direction and normal direction respectively with the cross response ignored, and then the relative size of mode shape were obtained with the assistance of capacitive sensor. These mode shapes could be seen in Tab 4. According to the axial depth of cut, the mode shapes at the corresponding discrete points were interpolated within the range of these three measuring points, and the geometric dimensions and physical properties of the workpiece were shown in Tab 6. Fig. 55 (a) depicts the dynamic tests and removal of thickness for the workpiece. As the first mode of the workpiece was the bending mode, the start edge of the workpiece was chosen as the dynamic test zone where the frequencies of the first two modes could be identified. There were two tap zones in the workpiece: T1 and T2. Then the impact tests were applied in the workpiece to obtain the damping ratio of removal of 8 mm and 12 mm of thickness, and the damping ratio were 3% and 2.5% respectively. The average value of the frequency in the two zones were regarded as the experimental frequency in Table 7, and the FRF of T2 was showed in Fig. 55 (b).
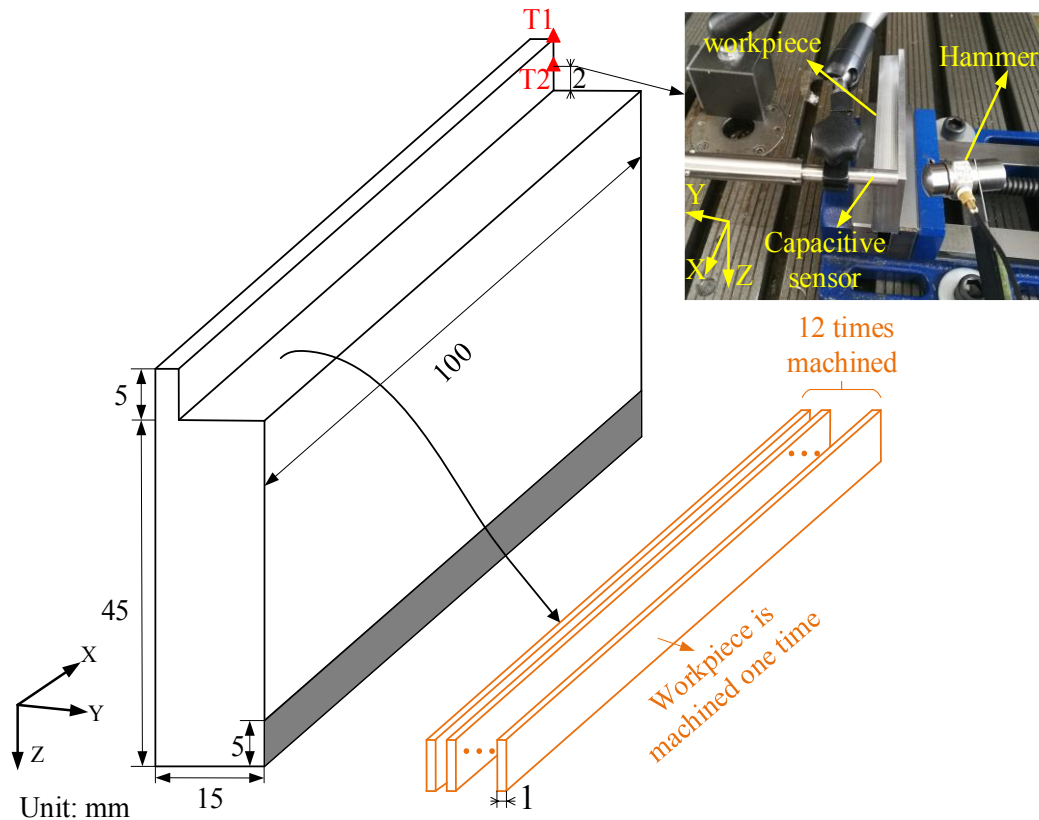

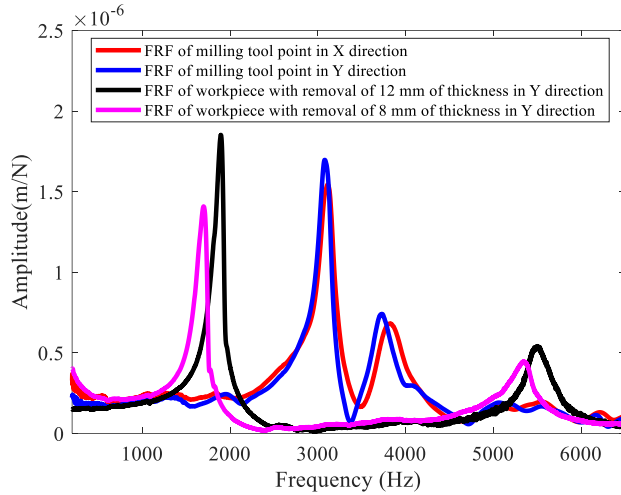Fig. 55 (a) Tap zone for workpiece

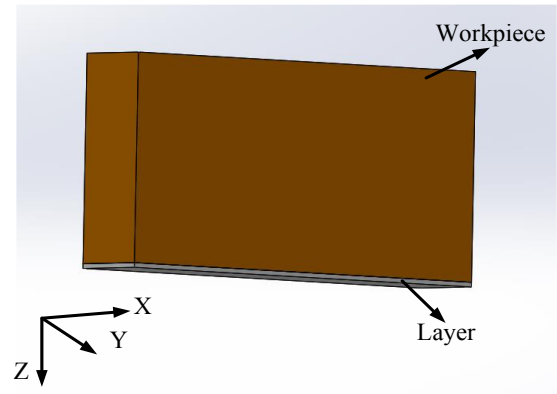Fig. 55 (b) Measured FRF for workpiece and milling tool

Fig. 56 Modified model of workpiece

Table 6 Physical properties of workpiece

Material	Geometry parameters	Clamping height	Density	Young's modulus	Poisson's ratio
Aluminum alloy 2007	100×40×15 mm	5 mm	2850 kg/m³	71 GPa	0.33

As shown in Tab 7, it can be seen that there was a large frequency difference between the simulation and experimental measurement of the workpiece. Since the workpiece did not have a base at the bottom, the clamping part was not rigid contact with the fixture, which was the main reason for the large error. Flexible contact between workpiece and fixture would bring in translational and rotational effects [102]. Therefore, a contact layer with thickness of 1 mm was added at the bottom of the workpiece to modify the free vibration in the simulation environment (see Fig. 56). The orthotropic parameters of the thin layer were applied to simulate the natural frequency, so the Young's modulus in X and Z directions for the layer (E_x and E_z) were needed. The Young's moduli, E_x and E_z, were determined by the following steps:

Step 1. The Young's modulus in Y direction was a fixed value of 0.1 GPa, and the initial Young's modulus in X and Z directions (E_x and E_z) were given with different value.

Step 2. Construct frequency function determined by optiSLang in Ansys environment: $f_n = f(E_x, E_z)$.

Step 3. When the frequency error between the experimental measurement, f_m, and the result of function, f_n, satisfied $\left|\frac{f_n - f_m}{f_m}\right| \leq 5\%$, the iteration of Young's modulus stopped.

From the above iteration, Young's Modulus in X and Z direction were $E_x = 0.34$ GPa and $E_z = 0.31$ GPa respectively. Figs. 57 and 58 depict the results of modification and experiment, and the modification matched well with the practical machining condition. As illustrated in Fig. 55 (b), the difference between the first and second order frequency of the milling tool was small, while the difference between the first and second order frequency of the workpiece was large. The amplitude of the first mode was higher than that of the second mode in terms of the workpiece. Therefore, a conservative SLD would be developed with three frequencies considered: the first two modes of the milling tool and the first mode of the workpiece. Although the dominant modes of the tool-workpiece system were not known, the parameters selected from the conservative SLD could ensure the stability of the machining process.

Table 7 Natural frequency of workpiece under different conditions

| Machining distance in radial direction	Axial depth of cut	The first order (Simulation under rigid contact/ Experiment/ Modification)	The second order (Simulation under rigid contact/ Experiment/ Modification)
0 mm	5 mm	5874 Hz/1579 Hz/1617 Hz	7793 Hz/5023 Hz/4868 Hz
4 mm	5 mm	6178 Hz/1611 Hz/1686 Hz	8050 Hz/5156 Hz/4965 Hz
8 mm	5 mm	6522 Hz/1715 Hz/1762 Hz	8323 Hz/5281 Hz/5053 Hz
12 mm	5 mm	6929 Hz/1898 Hz/1851 Hz	8729 Hz/5494 Hz/5220 Hz
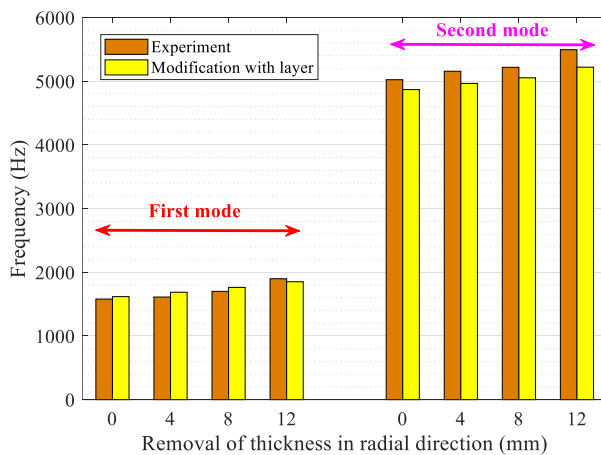
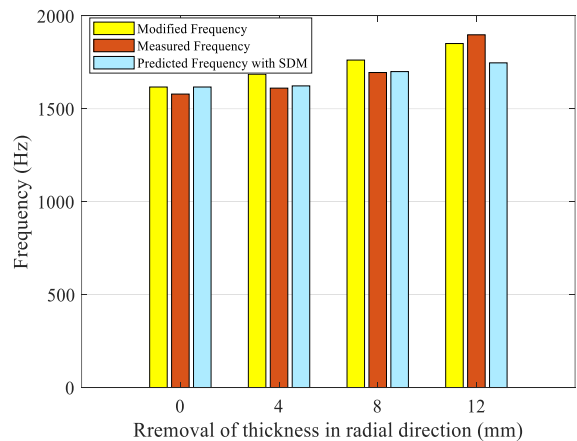Fig. 57 Frequency comparison between experiment and modification

Fig. 58 Frequency change of first mode for different removal of thickness

5.3.2 Experiment verification and measurement

To validate the proposed model, cutting tests were conducted on the machine tool (DMU80 monoBLOCK by DMG MORI Co., Ltd.). As shown in Fig. 59, a four-fluted carbide end mill with diameter of 10 mm was used, and the free overhang length of milling tool was 40 mm. Prior to establishing SLD, the full immersion was selected to calibrate the cutting force coefficients. In the experiment, the linear model of mean cutting force, which takes the feed per tooth as the independent variable, was applied to calibrate the cutting force coefficients [34]. The spindle speed of 6600 rpm and the axial depth of cut of 1 mm were selected when the work of calibration was conducted. The feed per tooth were from 0.01 mm to 0.09 mm with the increment of 0.02 mm, and the cutting forces were collected by the dynamometer (KISTLER 9257B). Finally, the four cutting force coefficients could be determined: K_t=1.03×10^9 Pa, K_r=5.15×10^8 Pa, K_{te}=12.3×10^3 N/m, K_{re}=21.3×10^3 N/m. With respect to down milling, the cutting tooth moves from unmachined surface to machined surface, i.e., from cut-in to cut-out, and the instantaneous uncut chip thickness decreases. From this point of view, the machined quality with down milling is better than that of up milling. As the distance between the machined surface and the reference surface needed to be measured in the experiment, down milling was selected with the start and exit angle: $\begin{cases} \phi_s = \arccos(2a_e/D - 1) \approx 143° \\ \phi_e = \pi = 180° \end{cases}$.

The radial immersion ratio should be less than 50%, which ensures that the response of the workpiece was mainly in normal direction. Here, the radial immersion ratio of 10% was employed, and the feed per tooth was 0.1 mm/tooth. The cutter locations were defined as number of five along the toolpath for this machining experiment.
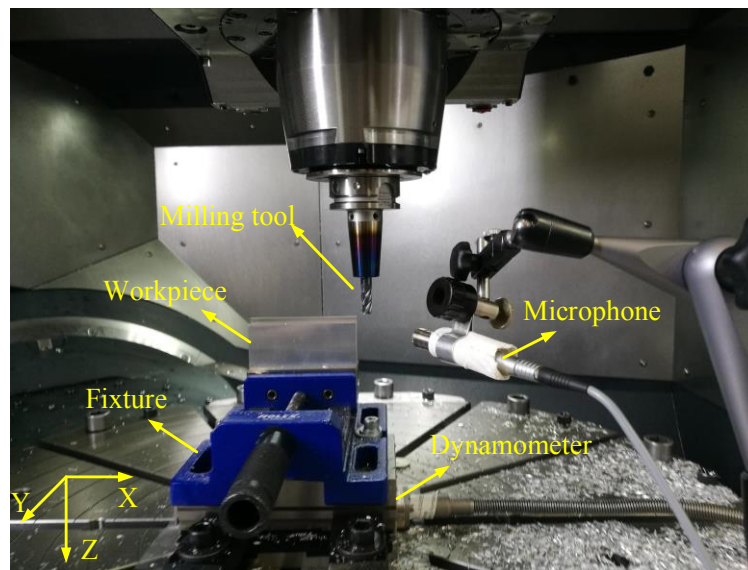

Fig. 59 Experimental setup for milling

When the frequency of the workpiece changes, the SLD changes with it as well. As can be seen from Fig. 60, the Lobe 1 was the main lobe of the SLD in the spindle speed range from 10000 rpm to 15000 rpm, and Lobe 2 appeared suddenly with the increase of frequency of workpiece. It should be noted that Fig. 60 (a) was developed with considering the maximum first mode shape of the workpiece, i.e. Fig. 60 (a) was a conservative SLD. In fact, the dominant modes between the workpiece and the tool were unknown. Fig. 60 (b) showed that once the milling tool was the dominant mode during the cutting process, the critical depth of cut would increase. Therefore, the best spindle speed range can be obtained from frequency domain perspective [1]:

$$\Omega_{best} = \frac{\omega_{rd} \bullet 60}{2\pi(N_f + 1) \bullet N} \qquad N_f = 0, 1, 2, \cdots \tag{5.13}$$

where N_f is the ordinal number of lobe.

Based on the best spindle speed from Eq. (5.13) and the conservative SLD, the axial depth of cut of 5 mm was selected with spindle speed range from 11500 rpm to 12400 rpm.
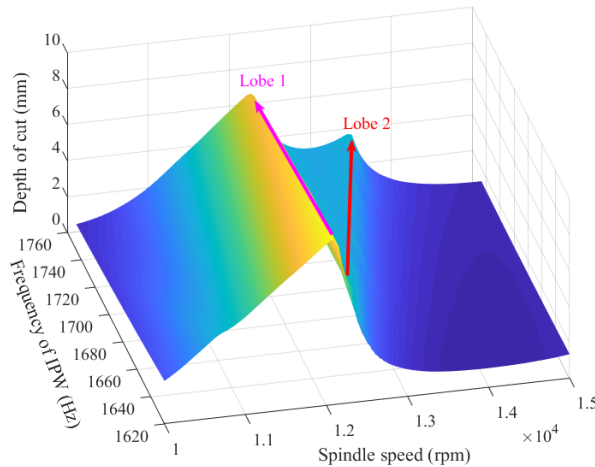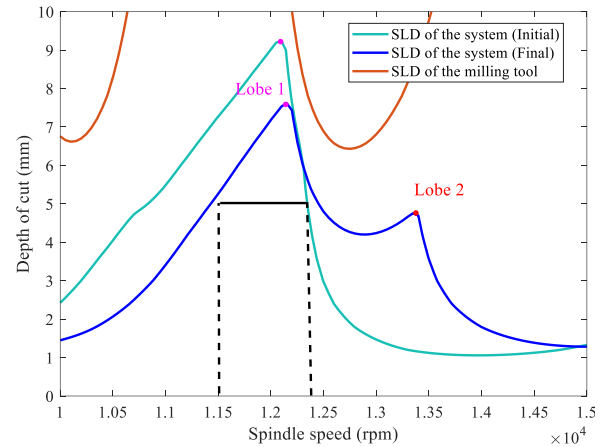

Fig. 60 (a). Three-dimensional conservative SLD

Fig. 60 (b). SLDs for considering dynamics of workpiece and milling tool

If the IPW dynamics was applied to construct the equation of SLE and solved the equation with the multi-dimensional bisection method [103], though the position-dependent CSLE with convergence would be obtained, the calculation efficiency was much lower. What was needed here was which radial immersion would cause instability during continuous milling process. In order to simplify the equation, the average frequency and mode shape of IPW were used as the modal parameters of workpiece. Here, the spindle speeds of 12100 rpm, 12250 rpm and 12400 rpm, and the axial depth of cut of 5 mm were selected as the experimental machining parameters. Then the continuous machining models of CSLE for the removal of 8 mm and

12mm of thickness at 12250 rpm were constructed respectively, and the same way was employed to develop the model for the rest spindle speeds. As shown in Figs. 61 and 62, the calculated results appeared in the form of point clouds. The triangle at the lower left of the figure was the area where variable, $\frac{a_e}{D} + \frac{CSLE}{D}$, was less than or equal to 0, and it was not the bifurcation among [0, 0.04] [58]. It can be seen that when the radial immersion was around 10%, all the corresponding cumulative errors showed convergence, and there was no bifurcation or bistable regions. That is to say, when the radial immersion was 10%, the SLE generated by continuous milling was a fixed convergence value. In this case, the instability caused by the continuous radial immersion was excluded. Once the SLE converges, it means the SLE caused by each immersion does not destroy the convergence of the system. Therefore, the SLE calculated by equivalent one immersion could be viewed as the CSLE at the radial immersion of 10%.
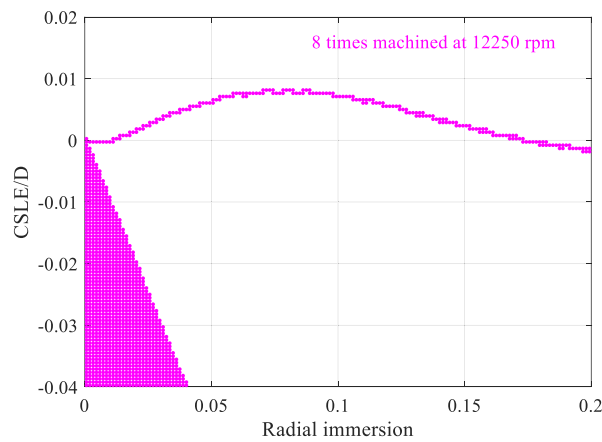

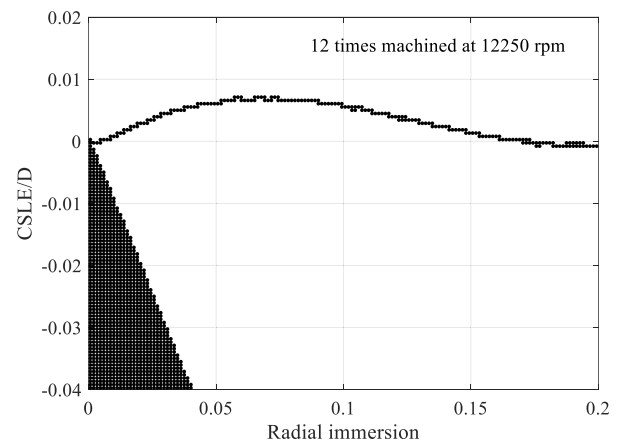Fig. 61 CSLE for 8 times machined at 12250 rpm   Fig. 62 CSLE for 12 times machined at 12250 rpm

In order to show how Figs. 61 and 62 were computed, the main programs in Matlab environment were added as follows.

Code #1   % from reference [103]

```
ax=[];
ax(1).val=linspace(0,0.2,20);% horizontal coordinate
ax(2).val=linspace(-0.04,0.04,20);% vertical coordinate
% constant parameters for CSLE
par=[];
par.spsd=spindle speed;
par.dia=tool diameter;
…
[H]=CumulativeSurface(ax,par)  % call the function of 'CumulativeSurface'
```

68

Code #2

```
function [H]=CumulativeSurface(ax,par)

H=zeros(1,length(ax(2,:)));

for kax=1:size(ax,2)

    if ((ax(1,kax)+ax(2,kax))<1)&&((ax(1,kax)+ax(2,kax))>0)

        H(kax)= GenerateSLE( (ax(1,kax)+ax(2,kax)), par.spsd)-ax(2,kax)*par.dia;

        % the function of 'GenerateSLE' can be developed from reference [9]

    end

end
```

In order to ensure the stability of the whole machining process, the force and sound signals were collected by dynamometer and microphone. These signals would be analyzed in frequency domain to identify whether chatter occurred or not. The spindle speed of 12250 rpm and the axial depth of cut of 5 mm were selected to validate the stable machining process. As the radial depth of cut was 1 mm, the workpiece was machined 12 times resulting in the removal of 12 mm of thickness in radial direction. For the spindle speed of 12250 rpm, the fundamental frequencies of the spindle speed and tool passing frequency were 204.2 Hz and 816.8 Hz respectively. As shown in Figs. 63 and 64, the force signal and the sound signal were smooth and regular in time domain, and the chatter frequency was not found except for the harmonics of stable frequency in frequency domain. Besides, the roughness could be measured to further show no chatter occurred. Similarly, the same way was used to verify other machining parameters of the experiment.
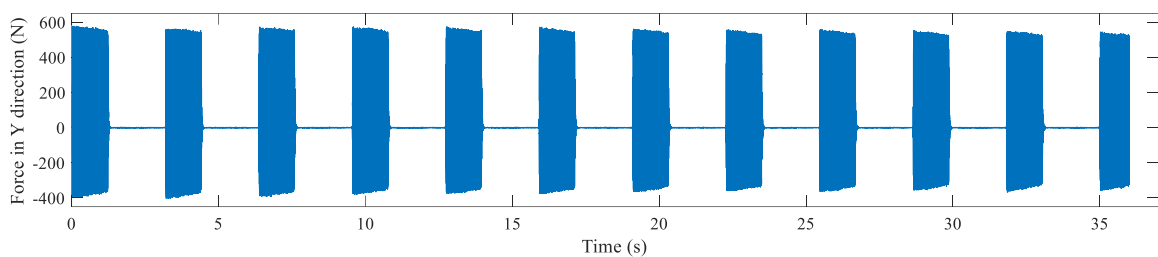

Fig. 63 (a). Force signal collected at spindle speed of 12250 rpm
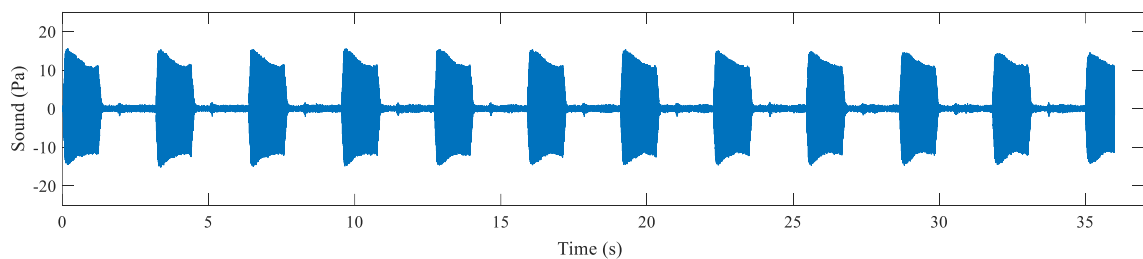

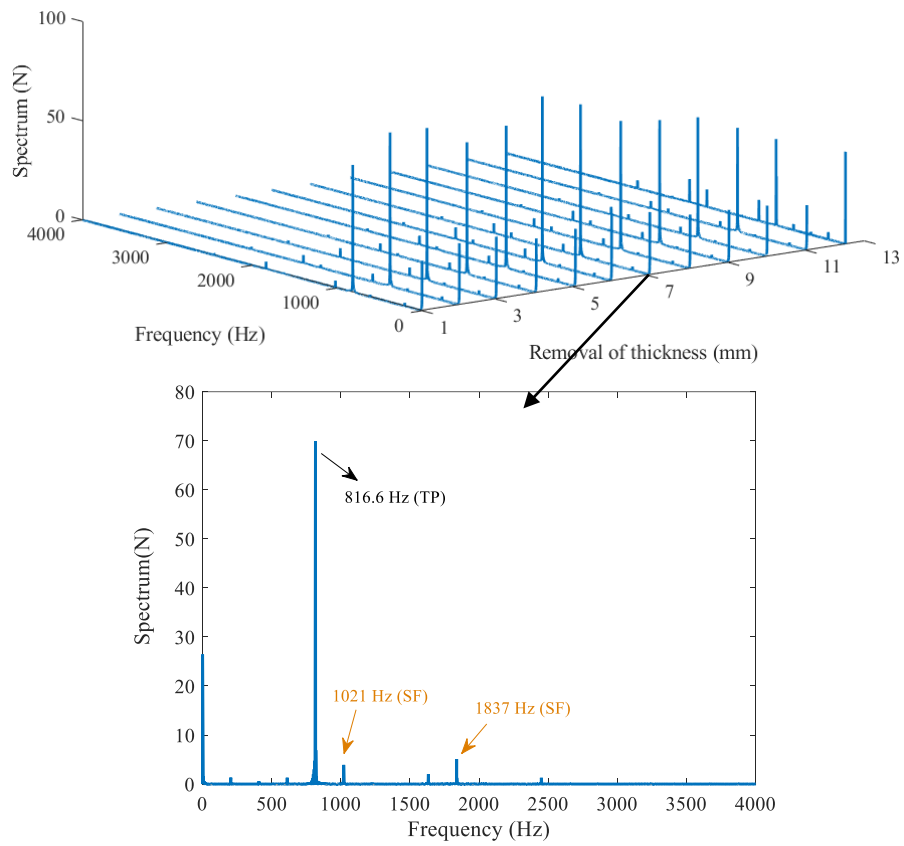Fig. 63 (b). Sound signal collected at spindle speed of 12250 rpm

Fig. 64 (a) Frequency spectrum of milling force. TP: Tool passing frequency and its harmonics, SF: Spindle frequency and its harmonics
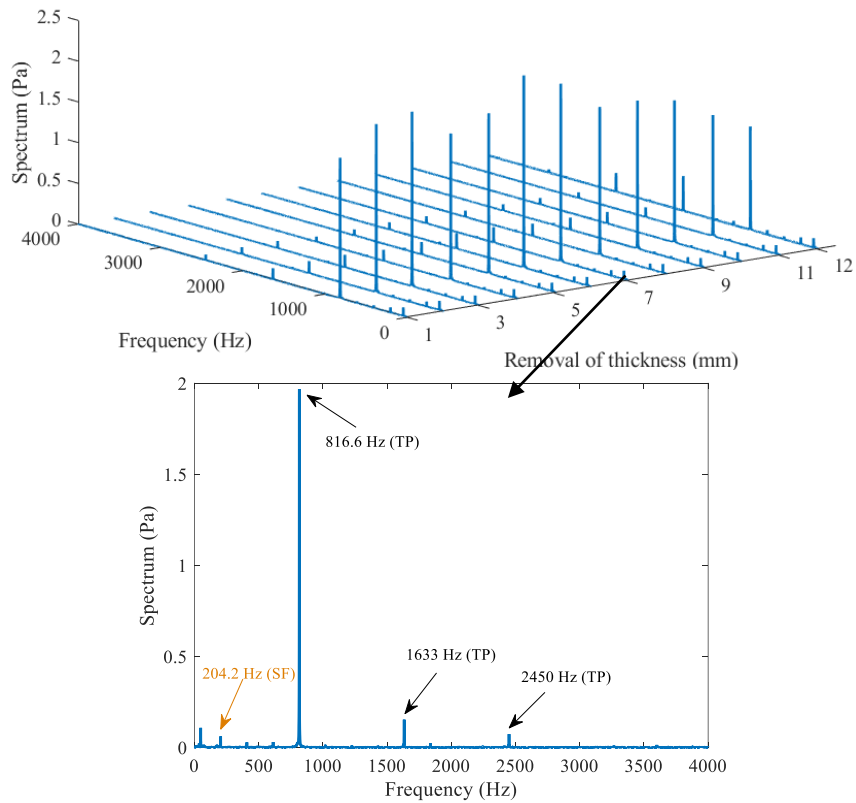

Fig. 64 (b) Frequency spectrum of sound. TP: Tool passing frequency and its harmonics, SF: Spindle frequency and its harmonics

5.3.3 SLE from the milling tool

SLE comes from the interaction of workpiece and tool, and its distribution depends on the mode shapes of tool and workpiece. When the rotation-free model of the spindle was used, the error distribution along the axial direction depended on the mode shapes of tool and workpiece at the discrete nodes. Along the feed direction, the mode shapes of workpiece mainly determined the variation of SLE. In the process from rough to fine machining, the stiffness of the workpiece was larger at the initial stage, and the mode of the tool played a leading role under this condition. The stiffness of the workpiece decreased gradually with the material removal, and the dominant mode may shift from tool to workpiece. In the cutting tests, the thickness of the workpiece went through 15 mm to11 mm, 7 mm to 3 mm. When the thickness became smaller, the amplitude of the FRF of workpiece was more obvious. Therefore, the distribution of CSLE was analyzed when the thickness of workpiece was 7 mm and 3 mm, and the influence of FRF of workpiece on SLE was studied.

When only the frequency response of the milling tool was considered, the theoretical CSLE between 11500 rpm and 12400 rpm did not change significantly, and the CSLE along the axial direction of the tool did not vary a lot for a specific spindle speed. This indicated the CSLE caused by forced frequency was smaller in the range of these spindle speeds. As shown in Fig. 65, the CSLE belonged to the undercut situation, so these errors could be eliminated by suitable removal of thickness.
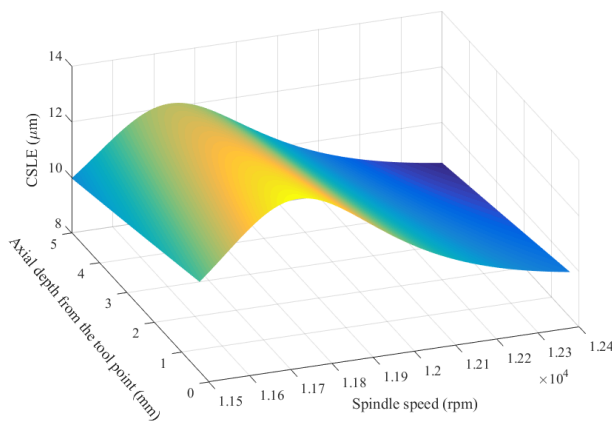
Fig. 65 CSLE distribution with only considering
dynamics of milling tool
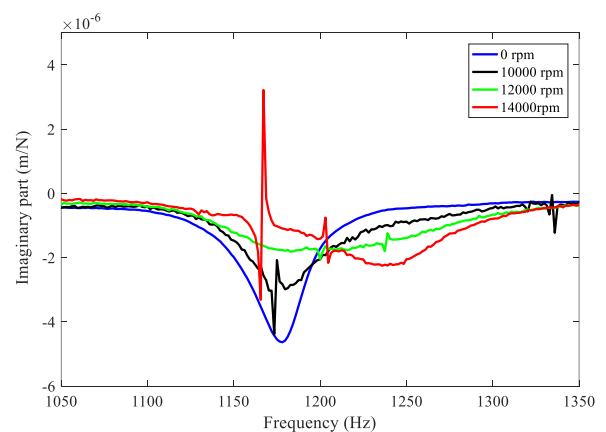
Fig. 66 FRF change of dummy with different
rotational speeds

As the dynamic response of the spindle is difficult to be determined by a prediction model, it is qualitatively analyzed by the experimental measurement. As shown in Fig. 66, the dynamic response at different rotational spindle speeds was obtained. It should be noted that the contact stiffness of the bearings would change with the increase of spindle speed, which would affect the response of the tool holder. In order to get the frequency response of the experimental machine tool in the running condition, the dummy was clamped in the tool

holder for response tests with free tool overhang length of 70mm. It can be seen from the experiment results that the natural frequency of dummy decreased gradually with the increase of spindle speed, i.e. the CSLE from the tool would change a little bit in practical machining process.

5.3.4 SLE from the in-process workpiece

For the stage from rough to fine machining, the effect of material removal was not negligible, which affects FRF of the workpiece through frequency and mode shapes. In this case, the number of meshed elements were 3420 with coarse mesh in Ansys, and the corresponding error, $\left| \dfrac{\sum \Delta M_w / 3 - \rho v}{\rho v} \right|$, did not exceed 5% for both removal of 8 mm and 12 mm of thickness. Through the above frequency verification, SDM method could effectively predict IPW dynamics, and the mode shape of the workpiece was obtained by SDM method [104].
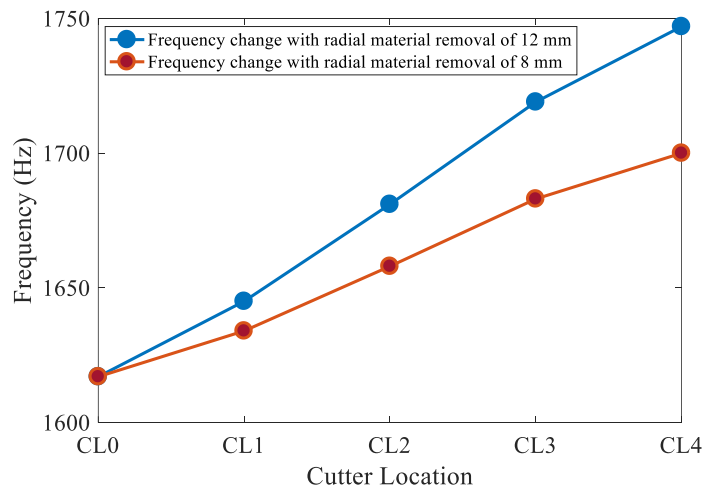

Fig. 67 Frequency change for different radial machining times
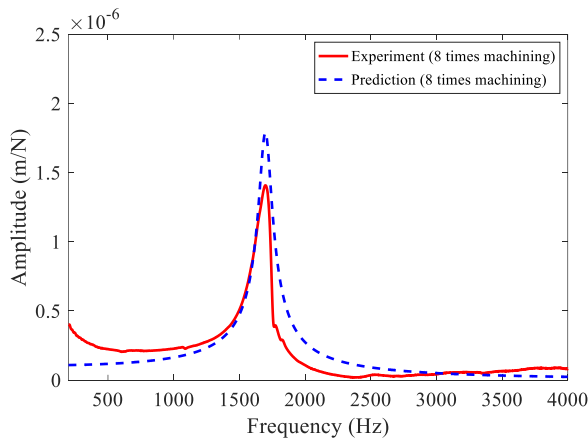

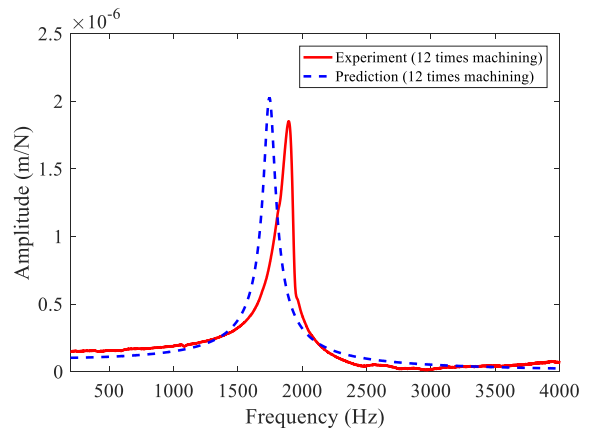Fig. 68 (a). FRF comparison for removal of 8 mm of thickness

Fig. 68 (b). FRF comparison for removal of 12 mm of thickness

The experimental results (see Figs. 67 and 68) showed that though the natural frequency and mode shape of the workpiece increased during the material removal process, the change of the mode shape was greater than the change of frequency, which leads to the amplitude increase of FRF of the workpiece. With obtaining the IPW dynamics during material removal, 8 and 12 times machined of the workpiece were considered as removal of 8 mm and 12 mm of thickness for one time. The offset error of workpiece caused by IPW dynamics was regarded as SLE of workpiece.

The increase in frequency made the eigenvalue of the dynamic equation relatively smaller. That is, the stability boundary became larger. In addition, the change of the mode shape in Y direction for removal of 8 mm and 12 mm of thickness was not much different. That was the reason why the SLE decreased when the number of cutting times increased.

(a)

(b)

(c)

(d)
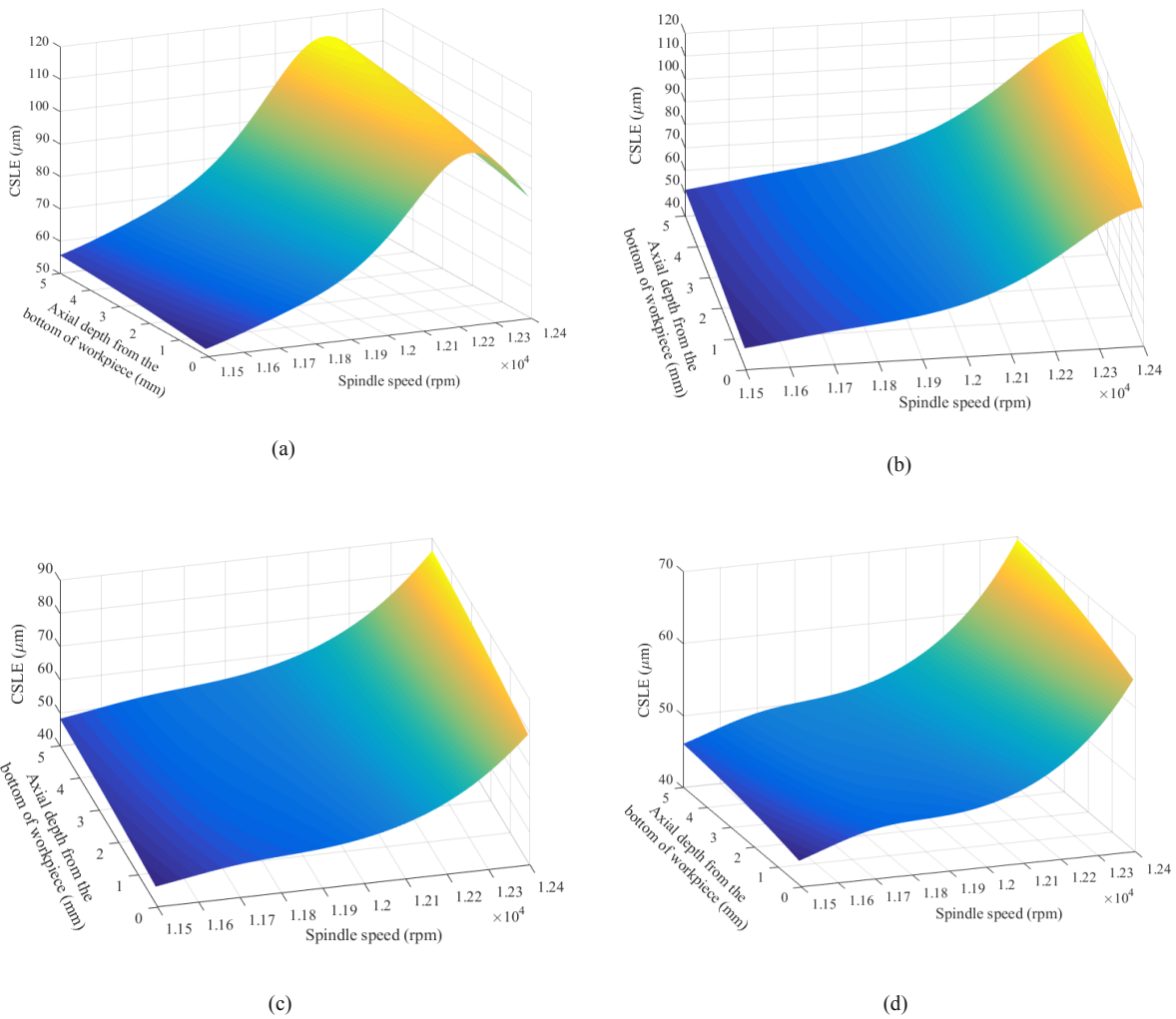
Fig. 69. (a) CSLE distribution for 8 times machined at CL1. (b) CSLE distribution for 8 times machined at CL2. (c) CSLE distribution for 8 times machined at CL3. (d) CSLE distribution for 8 times machined at CL4.

(a)

(b)

(c)

(d)
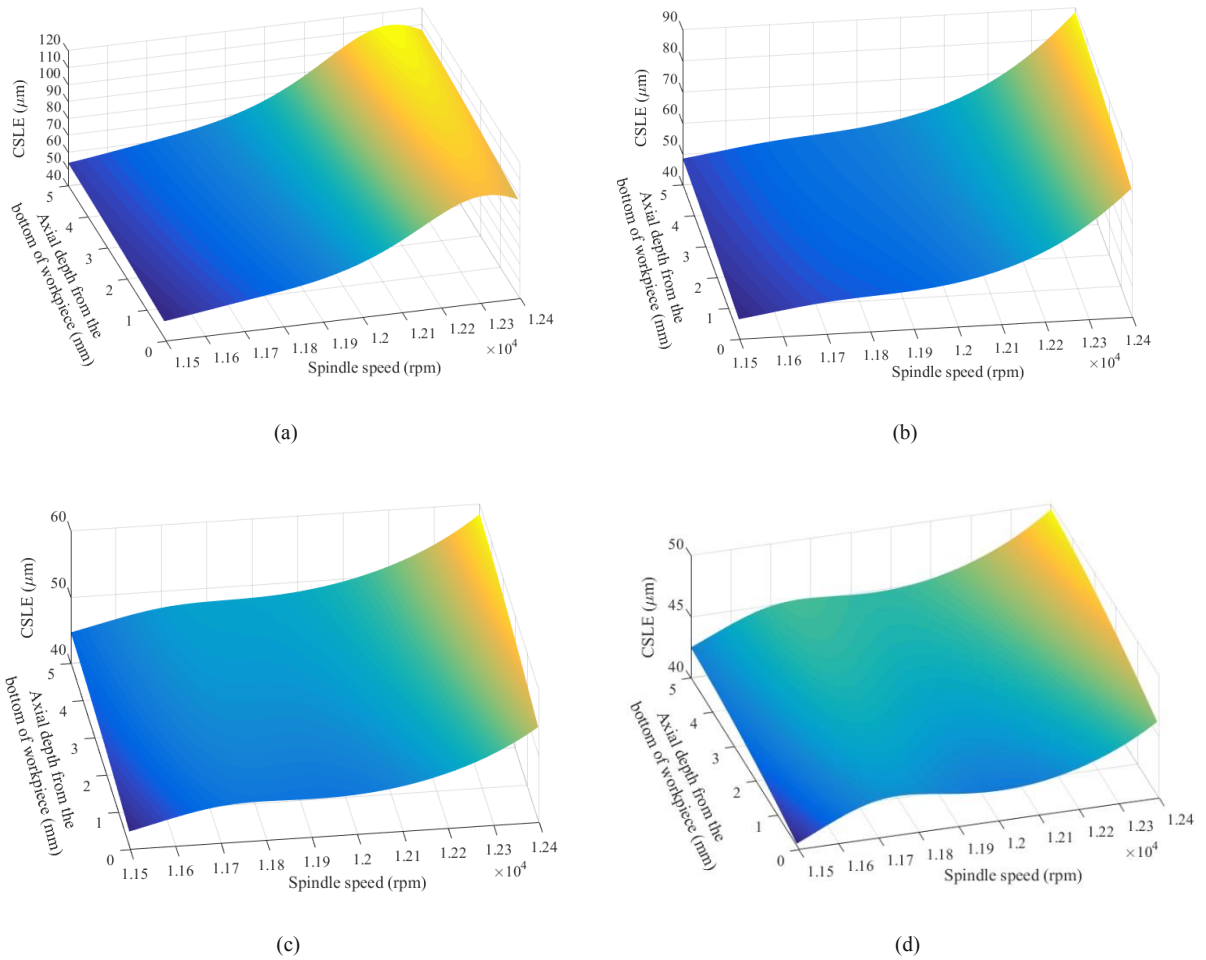
Fig. 70. (a) CSLE distribution for 12 times machined at CL1. (b) CSLE distribution for 12 times machined at CL2. (c) CSLE distribution for 12 times machined at CL3. (d) CSLE distribution for 12 times machined at CL4.
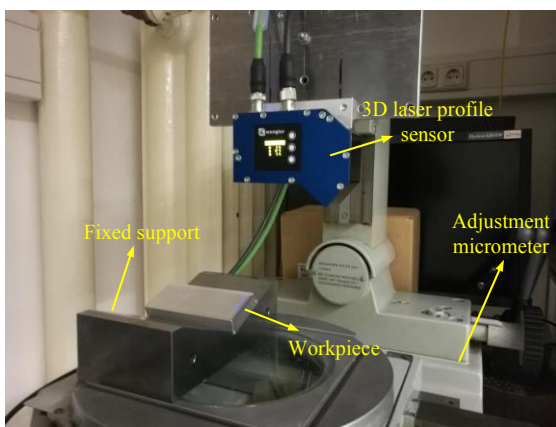
Fig. 71. Setup for scanning the profile of machined surface.
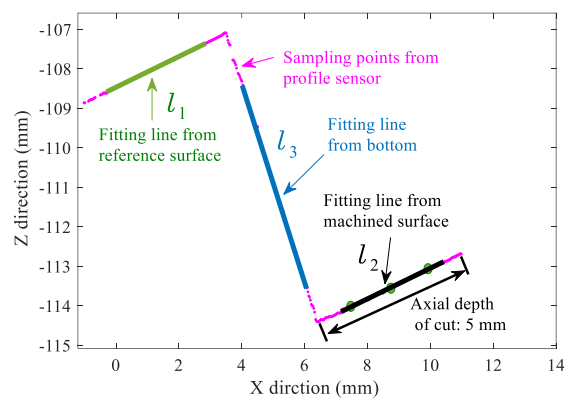
Fig. 72. Fitting lines for CSLE measurement

The CSLE of the workpiece presented dynamic changes with the material removal, and the distribution of CSLE at different cutter locations and spindle speeds was illustrated in Figs. 69 and 70. Due to the existence of measurement error and uncertainty, the machining parameters

74

corresponding larger CSLE were selected for verification. The machining parameters selected for validation were as follows: 12100 rpm with 8 and 12 times machined (12100-8 and 12100-12), 12250 rpm with 12 times machined (12250-12), and 12400 rpm with 8 times machined (12400-8). The 3D laser profile sensor (MLWL131 from Wenglor) was applied to obtain the contour of the machined workpiece at different cutter locations with three straight lines defined as follows (see Figs. 71 and 72):

$$\begin{cases} l_1 : y = k_1 x + p_1 \\ l_2 : y = k_2 x + p_2 \\ l_3 : y = k_3 x + p_3 \end{cases} \tag{5.14}$$

where l_1 is the fitting line from the reference surface, l_2 is the fitting line from machined surface, and l_3 is the fitting line from bottom, k_1, k_2 and k_3 are the corresponding slopes of l_1, l_2 and l_3 respectively; p_1, p_2 and p_3 are the corresponding intercepts of l_1, l_2 and l_3 respectively.

On the basis of three straight lines, the angle between two straight lines is defined as:

$$\theta = \arctan \left| \frac{k_a - k_b}{1 + k_a * k_b} \right| \tag{5.15}$$

where k_a and k_b represent the slopes of two different straight lines.

Three angles were calculated to evaluate the measurement error and deformation of workpiece during continuous radial immersion. These three angles were: the angle $\angle A$ calculated by l_1 and l_2, the angle $\angle B'$ calculated by l_1 and l_3, and the angle $\angle C'$ calculated by l_2 and l_3. In order to show the variation of angle A′ and angle B′, the two angles were redefined as:

$$\begin{cases} \angle B = 90° - \angle B^{'} \\ \angle C = 90° - \angle C^{'} \end{cases} \tag{5.16}$$

These three angles worked together ($\angle A$, $\angle B$ and $\angle C$), and one of the three angles was equal to the sum of the rest two angles. The measurement ranges of the CSLE mainly focused on the cutter locations from CL1 to CL4 (see Fig. 53(b)). The CSLE measured from Fig. 72 can be written as:

$$\begin{cases} \text{CSLE} = (n * a_e - d_h) \\ d_h = \left| \dfrac{y_m - k_1 x_m - p_1}{\sqrt{1 + k_1^2}} \right| \end{cases} \tag{5.17}$$

where n is the machining times, d_h is the distance between sampling point from machined surface and l_1, and (x_m, y_m) are the coordinates selected from the scanning data of machined surface.

For the CSLE distribution along axial direction of milling tool, the change tendency between the predicted and the measured result was not completely consistent. That means the mode shapes for simulation were not completely same with the mode shapes in practical milling process during the complex interaction between milling tool and workpiece. In general, the predicted tendency of simulation matched well with the measured results in terms of the four groups of machining parameters (12100-8, 12100-12, 12250-12 and 12400-8). With respect to the same machining conditions, the CSLE at the end of workpiece was smaller than that at the start of workpiece. Figs. 73-75 presented the simulation and measurement results respectively. For the machining parameters of 12100-8, the maximum error of angle ($\angle$A or $\angle$C) at CL0, CL1 and CL2 was nearly greater than 1°, which results in a relative large CSLE near CL1 (28 mm) and CL2 (51 mm). The maximum error of angle ($\angle$A or $\angle$C) at CL1 and CL3 was greater than 1° in terms of machining parameters of 12100-12, leading to a relative large CSLE near CL1 (28 mm) and CL3 (74 mm). With respect to the machining parameters of 12250-12, the maximum error of angle ($\angle$A or $\angle$C) at CL2 and CL4 was around 1°, and it made the CSLE a little bit large near CL2 (51 mm) and CL4 (97 mm). For the machining parameters of 12400-8, the maximum error of angle ($\angle$A or $\angle$C) at CL0 and CL1 was more than 1°. As a result, the CSLE near CL1 (28 mm) was larger.
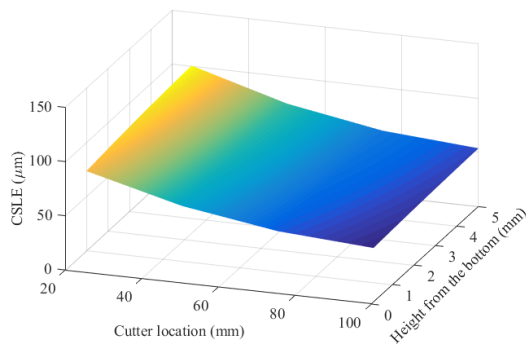
(a)
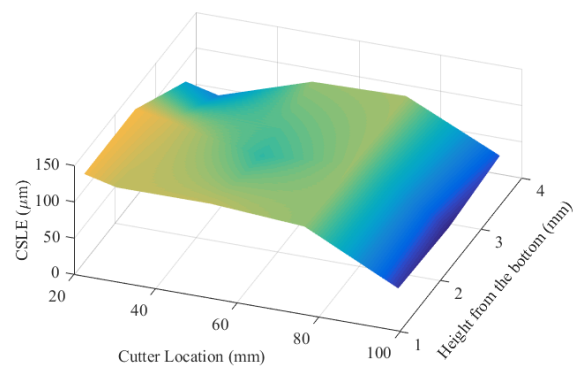
(a)
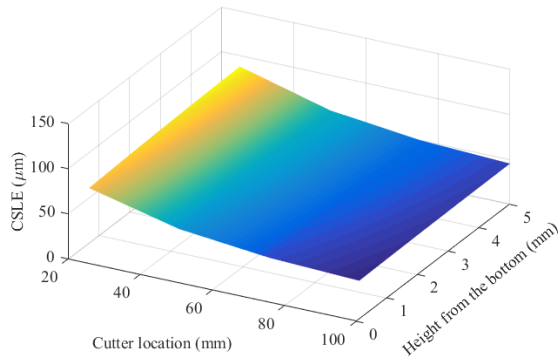
(b)
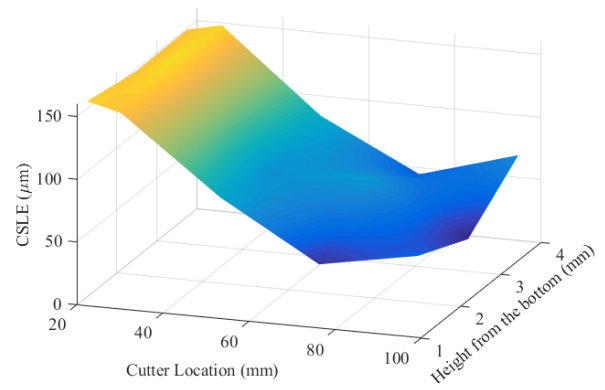
(b)
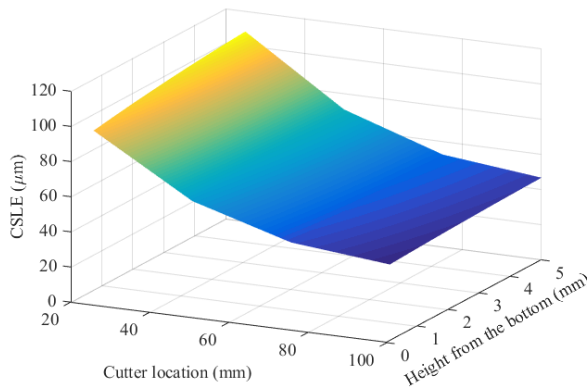
(c)
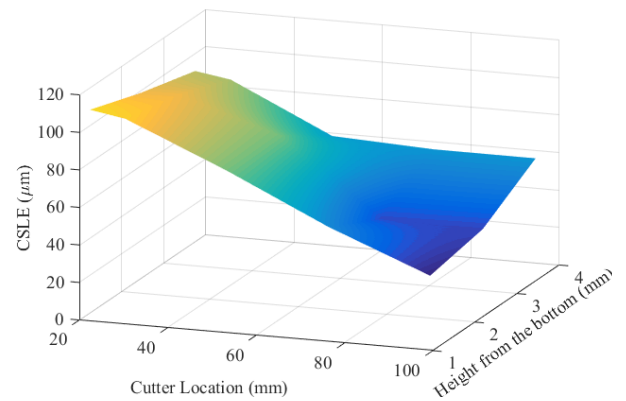
(c)
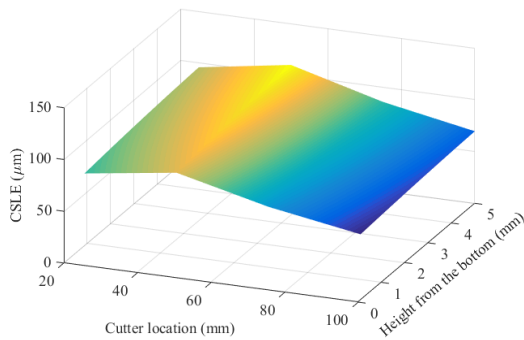
(d)
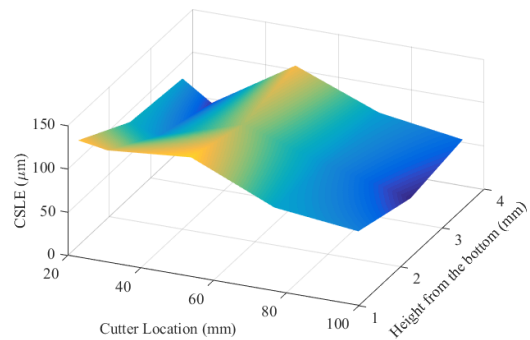
(d)

Fig. 73. (a) Prediction of CSLE along the tool path with the parameter of 12100-8. (b) Prediction of CSLE along the tool path with the parameter of 12100-12. (c) Prediction of CSLE along the tool path with the parameter of 12250-12. (d) Prediction of CSLE along the tool path with the parameter of 12400-8.

Fig. 74. (a) Measurement of CSLE along the tool path with the parameter of 12100-8. (b) Measurement of CSLE along the tool path with the parameter of 12100-12. (c) Measurement of CSLE along the tool path with the parameter of 12250-12. (d) Measurement of CSLE along the tool path with the parameter of 12400-8.
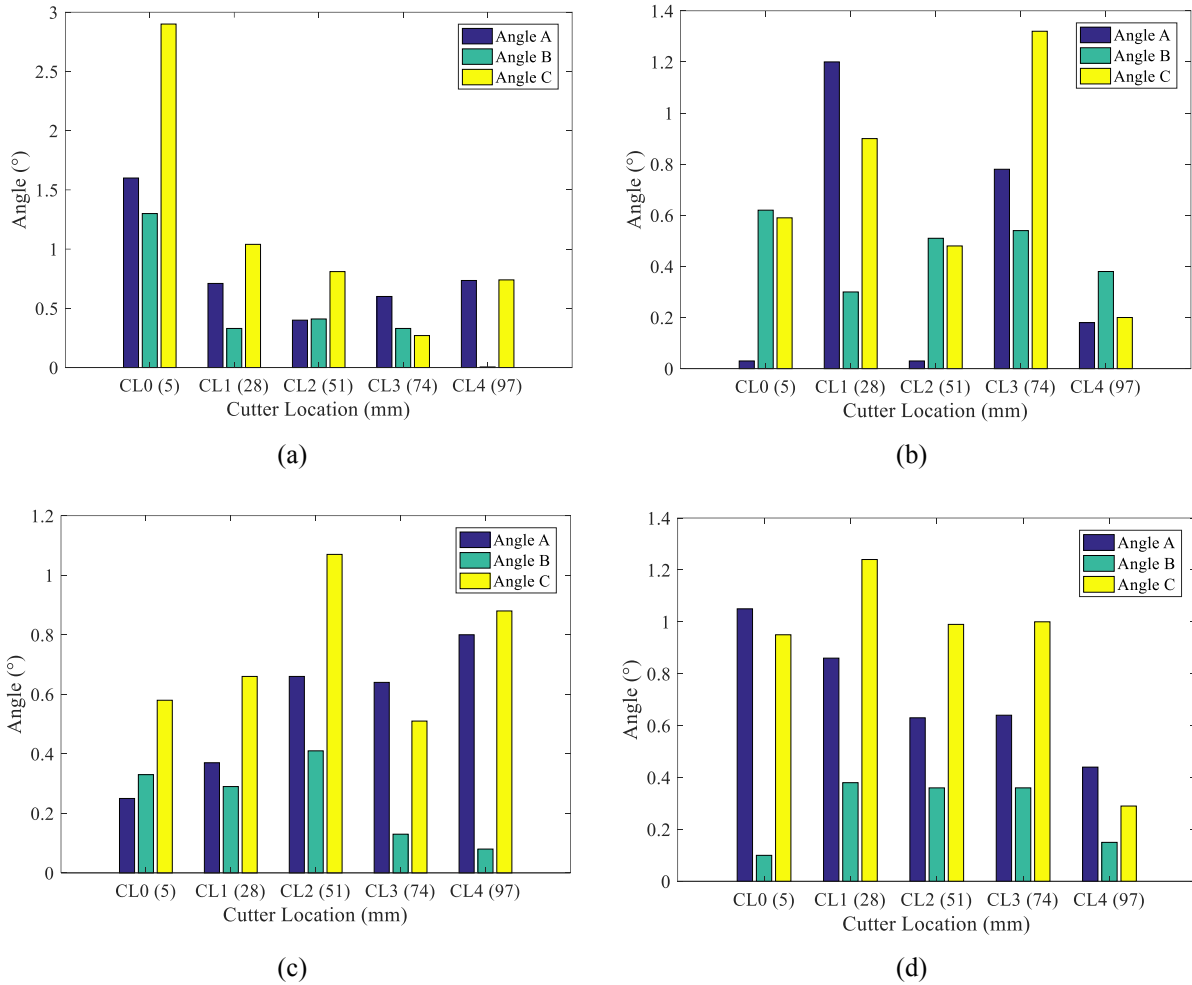
Fig. 75. (a) Measured angle along the tool path with the parameter of 12100-8. (b) Measured angle along the tool path with the parameter of 12100-12. (c) Measured angle along the tool path with the parameter of 12250-12. (d) Measured angle along the tool path with the parameter of 12400-8.

5.3.5 The roughness at different cutter locations

Table 8 Roughness measured at CL0-CL1 and CL3-CL4 with different spindle speeds

	CL0-CL1				CL3-CL4			
Spindle speed (rpm)	12100		12250	12400	12100		12250	12400
Cutting times	8	12	12	8	8	12	12	8
Rt (μm)	5.0	4.8	4.6	4.1	4.1	4.1	4.3	4.0
Ra (μm)	0.83	0.89	0.93	0.74	0.85	0.80	0.90	0.70
Rt/Ra	6.02	5.39	4.95	5.54	4.8	5.13	4.78	5.71

Roughness could show the local profile of workpiece. Here, the roughness average (Ra), maximum height of the profile (Rt), and the ratio between Rt and Ra were employed to

characterize the machined surface [15]. Before measurement, ultrasonic vibration device was used to remove burrs and impurities on the machined surface of workpiece. In fact, the roughness was related to the feed per tooth, and the measurement was based on the feed per tooth, 0.1 mm/tooth. The contact measurement was employed with the roughness instrument. The measuring length was 2.5mm, and the number of consecutive samples was five. As shown in Tab. 8, the Ra was not very large, and the ratio Rt/Ra basically maintained around 5, which indicated that the machined surface consistency was relatively good.

The roughness value changed slowly from the start of the workpiece to the end of workpiece, and the roughness at the end of the workpiece was smaller than that of start. For 8 times machined at spindle speed of 12100 rpm, the Ra increased slightly, but the ratio Rt/Ra decreased significantly. For 8 times machined at spindle speed of 12400 rpm, although both the Rt and Ra declined, the ratio between Rt and Ra grew a little. That was because the relative variation of Rt was smaller than that of Ra. The consistency of the whole measurement results was good. That is, the roughness at the end of the workpiece was smaller than that at the start of the workpiece. Although there were uncertainties during the measurement process, the roughness in Tab. 8 were obtained through five consecutive samples. Therefore, the variation of roughness could be mainly attributed to the dynamics change of the workpiece. The results of the roughness further expounded the dynamic effects from workpiece, which matches well with the results of CSLE.

5.3.6 The static deformation of the workpiece

Fig. 76 presented the cutting force simulated with the cutting force coefficients, and then the average cutting force in Y direction was obtained with the value of 102 N. The average cutting force in Y direction from the dynamometer was 98 N. The error between the simulation and experiment was 4%. That means the simulated value of 102 N could be employed in the deformation calculation in Ansys. When only the static deformation caused by cutting force was considered, the deformation of the workpiece can be simulated in Ansys. As illustrated in Figs. 77, the simulation results showed that the static deformation of the workpiece remained around 40 μm.

Therefore, there is no direct relationship between CSLE and static deformation, which further verifies that CSLE is mainly caused by excitation frequency. That is, the CSLE has a strong dependence on spindle speed.
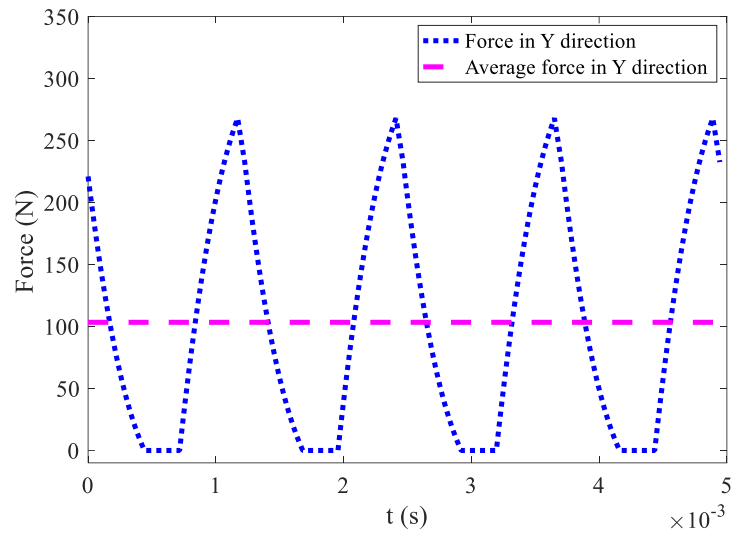
Fig. 76. Milling force simulated with cutting force coefficients in Y direction.
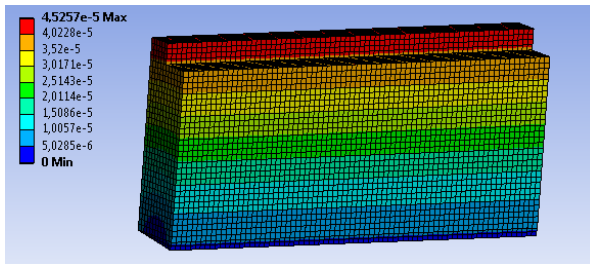
Fig. 77 (a). Deformation simulated for 8 times machined in Ansys
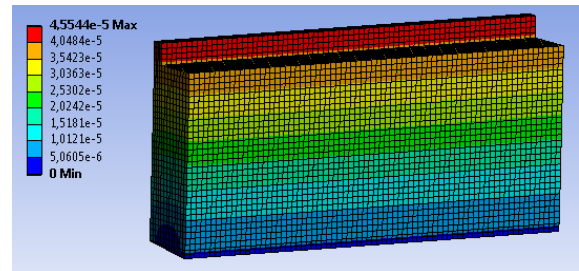
Fig. 77 (b). Deformation simulated for 12 times machined in Ansys

5.4 Summary

In this chapter, the milling force model was constructed by discrete elements of milling tool, and a two degree of freedom model considering the dynamics of both the workpiece and milling tool was established. On the basis of impact tests of the workpiece, the clamping conditions of workpiece were offset and modified in Ansys. With using the minimum frequency and maximum mode shape at each cutter location, the conservative SLD was obtained, and the instability caused by the cumulative effect of improper radial immersion was excluded. Then the stable machining parameters would be selected from the SLD with convergent radial immersion. By means of SDM and FE analysis, multiple immersions was equivalent to one immersion with same material removal, and finally equivalent dynamic CSLE of workpiece was obtained. The experiment showed that the frequency of the IPW along the tool path increased slowly and the CSLE decreased gradually during the continuous material removal, which was further verified by the roughness at the start and end of the workpiece respectively. The conclusions can be drawn as follows:

The clamping condition was an important factor for the dynamics of the workpiece. Different clamping conditions would make the workpiece show different modal characteristics, which leads to a large difference from the simulation in Ansys. The simulation process should be as close as possible to the actual machining process, which is an important premise to obtain the accurate prediction. Therefore, the dynamic tests should be employed on the workpiece before the simulation so that the modification and offset can be added in the Ansys simulation.

During the process of continuous material removal, the dynamic change of the workpiece was more significant than that of the tool, so more attention should be paid to the dynamic change of the workpiece. Under the given machine tool, the dynamic change of the workpiece affected not only the trend of SLD, but also the distribution of CSLE.

The proposed model can predict the distribution of CSLE effectively with the conservative SLD. Meanwhile, the dynamics of workpiece was the main source and main factor of CSLE, which must be considered. Besides, the proposed model can provide theoretical support for the selection of stable parameters and error control in the continuous immersion machining process.

It should be noted that both the bottom and flank of workpiece in contact with the milling tool would deform during continuous immersion, which affects the final measurement results of CSLE in turn. The maximum angle error ($\angle$A or $\angle$C) at different cutter locations always corresponded to the larger error between predicted and measured results, which matches well with the experiment results.

The CSLE of workpiece reflects the error during continuous stable machining process, and it mainly involves the spindle speed, axial and radial depth of cut. Different machining parameters were employed in terms of different requirements. The maximum material removal rate was taken as the goal to select machining parameters for rough machining while machining parameters were selected with the aim of higher machining accuracy for fine machining, which can reduce the machining cost and avoid the blindness of parameter selection. During continuous machining, the IPW dynamics had a great influence on CSLE and stability of machining system. Therefore, it is an important research direction to improve the limit of axial depth of cut and reduce the CSLE by modifying the structures of workpiece.

6 Stability and surface location error analysis for micro-milling

6.1 Mechanical modelling of micro-milling force

The process of workpiece and micro-milling tool interaction is dynamic, and the model can be simplified as a two degree of freedom system for both micro-milling tool and workpiece as shown in Fig. 78.
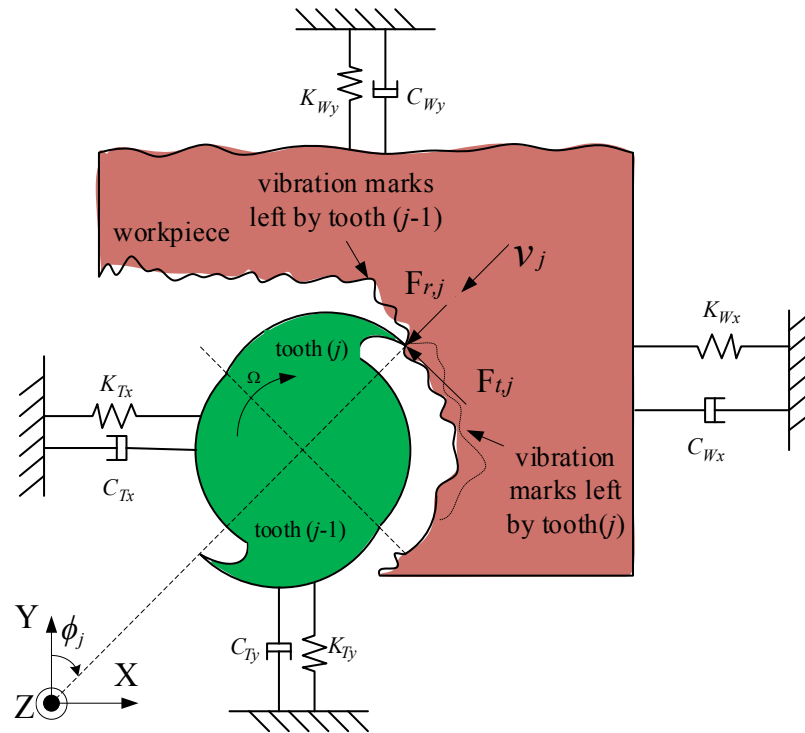
Fig. 78. Dynamic model of micro-milling

In the micro-milling process, the ratio of feed per tooth to radius is much larger than that of the macro case, and macro model is no longer applicable in this case. The actual trajectory of the tool point is trochoidal when the micro-milling tool rotates and keeps feeding continuously. After the cutter tooth contacted with the workpiece, the plastic deformation of the workpiece started to accumulate until to the critical thickness, and then the chips are formed. In order to make the calculation of thickness much easier, the model will be simplified in shearing zone with four assumptions:

- There is no obvious runout during the micro-milling process.

- The elastic deformation is negligible because it will fully recover to its original position.

- The effects of angular delay and process damping are ignored due to the small depth of cut and overlapped area.

- The instantaneous uncut chip thickness is larger than $0.3\,r_e$ (r_e is the radius of cutting edge), minimum cutting thickness so that the chips can be formed according to the work of Malekian et al. [105].

As shown in Fig. 79, plastic deformation is increased in the ploughing zone, and the chips are produced in the shearing zone where the instantaneous uncut chip thickness is larger than the minimum cutting thickness. The instantaneous uncut chip thickness of each tooth in shearing zone can be divided into two parts: the static part and dynamic part (vector of previous tooth, v_{j-1}, and vector of current tooth, v_j). Then the instantaneous uncut chip thickness in coordinate of micro-milling tool is written as:

$$h_j(t) = h(\phi_j(t)) = [\max \left| \overline{C_j F_j} - \overline{C_j F}_{j-1} \right| + v_{j-1} - v_j] g(\phi_j(t))$$
$$\approx [\overline{C_j F_j} - \overline{C_j F}_{j-1} + v_{j-1} - v_j] g(\phi_j(t))$$

(6.1)

where

$$v_j = -x \sin\phi_j - y \cos\phi_j$$

(6.2)
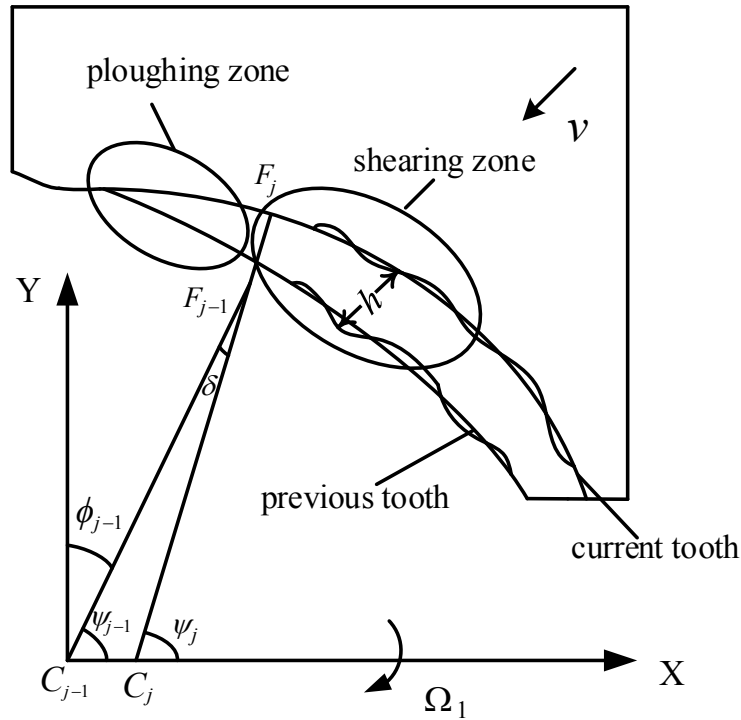
Fig. 79. Simplified chip thickness calculation in micro-end milling

In order to calculate analytical solution of the instantaneous uncut chip thickness, the position of tool point without dynamic displacements for tool and workpiece in X and Y direction is:

$$\begin{cases} x_t = x_f + r\sin(2\pi\Omega_1 t - \dfrac{2\pi j}{N}) \\[2mm] y_t = r\cos(2\pi\Omega_1 t - \dfrac{2\pi j}{N}) \\[2mm] x_f = Nf_z\Omega_1 t \end{cases} \tag{6.3}$$

where r is the tool radius, Ω_1 is the spindle speed (rps), t is the time, j is the ordinal number of tool teeth and N is number of teeth.

As shown in Fig. 79, in the triangle $\Delta\, C_{j-1}C_jF_{j-1}$, the geometric relation between previous trajectory and current trajectory according to sine theorem can be given as

$$\frac{\Delta x_f}{\sin\delta} = \frac{\overline{C_{j-1}F_{j-1}}}{\sin(\pi - \psi_j)} = \frac{r}{\sin(\pi - \psi_j)} \tag{6.4}$$

$$\Delta x_f = \overline{C_{j-1}C_j} = \Omega_1 f_z N(t_1 - t_0) \tag{6.5}$$

where δ is rotation angle between previous tooth and current tooth.

From Fig. 79, the geometric conditions are as follows:

$$\begin{cases} \psi_k = (1 + \dfrac{4j}{N})\dfrac{\pi}{2} - 2\pi\Omega_1 t_k \\[2mm] \omega t_j = \omega t_{j+1} + \delta - \dfrac{2\pi}{N} \\[2mm] \phi_j = \dfrac{\pi}{2} - \psi_j \end{cases} \tag{6.6}$$

where ψ is the tool cutting angle (counterclockwise), ϕ is also the tool cutting angle (clockwise), and ω is the angular frequency.

Then substituting Eqs. (6.5) and (6.6) into equation (6.4) yields:

$$\Delta x_f = \frac{f_z N}{2\pi}(\frac{2\pi}{N} - \delta) \tag{6.7}$$

$$\sin\delta = \frac{\Delta x_f \cos\phi_j}{r} = \frac{f_z}{r}\cos\phi_j - \frac{N\cos^2\phi_j}{2\pi r^2}f_z^2 \tag{6.8}$$

Due to the high spindle speed and the small size of micro-milling tool, the distance in feed direction is very short with a small rotation angle:

$$\begin{cases} \sin\delta \approx \delta \approx \dfrac{f_z}{r}\cos\phi_j \\[2mm] \cos\delta = \dfrac{\sqrt{r^2-(f_z\cos\phi_j)^2}}{r} \end{cases} \tag{6.9}$$

Then Eq. (6.7) can be rewritten as:

$$\Delta x_f = f_z(1-\frac{f_z N\cos\phi_j}{2\pi r}) \tag{6.10}$$

According to the cosine theorem from Fig. 79, there is:

$$\begin{cases} (\overline{C_j F_j})^2 = r^2 = (\Delta x_f)^2 + (\overline{C_j F}_{j-1})^2 - 2\Delta x_f\left|\overline{C_j F}_{j-1}\right|\cos(\pi-\psi_j) \\[2mm] \overline{C_j F}_{j-1} = -\Delta x_f\sin\phi_j + \sqrt{r^2-(\Delta x_f\cos\phi_j)^2} \end{cases} \tag{6.11}$$

Substituting Eqs. (6.9), (6.10) and (6.11) into Eq. (6.1) yields:

$$\begin{aligned} h_j &= [r-(-\Delta x_f\sin\phi_j+\sqrt{r^2-(\Delta x_f\cos\phi_j)^2})+v_{j-1}-v_j]g(\phi_j) \\ &= [r-r\cos\delta+\Delta x_f\sin\phi_j+v_{j-1}-v_j]g(\phi_j) \\ &\approx [\underbrace{f_z\sin\phi_j}_{\substack{\text{conventional}\\\text{part}}}+\underbrace{r-\sqrt{r^2-(f_z\cos\phi_j)^2}}_{\text{about 0}}-\underbrace{\frac{N}{2\pi r}f_z^2\sin\phi_j\cos\phi_j}_{\substack{\text{Modification}\\\text{part}}}+\underbrace{v_{j-1}-v_j}_{\substack{\text{dynamic}\\\text{part}}}]g(\phi_j) \end{aligned} \tag{6.12}$$

The instantaneous cutting force for j^{th} tooth is:

$$\begin{cases} F_{r,j} = K_r b h(\phi_j) \\ F_{t,j} = K_t b h(\phi_j) \end{cases} \tag{6.13}$$

6.2 Dynamics determination of micro-milling tool point

With the properties of low stiffness and high brittleness of micro-milling tool, EMA cannot be carried out on any part of the micro-milling tool. However, the direct and cross receptances of spindle-machine can be obtained by EMA, and a theoretical calculation for micro-milling tool and coupling algorithm between micro-milling tool and spindle-machine is needed. Therefore, the method combining RCSA with EMA on holder-spindle is applied to predict dynamic receptances of the tool point.

6.2.1 Receptance coupling substructure analysis for micro-milling

The individual coordinate and component of the model are defined with the method of RCSA [69]. As shown in Figs. 80 and 81, three simplified components were selected: a machine-spindle with free-fixed boundary conditions (III), a holder with free-fixed boundary conditions (II) and a micro-milling tool with free-free boundary conditions (I). Based on the

above definitions, the assembled receptances are expressed as a function of the individual component receptance.

For the micro-milling tool, the following direct receptances which include both translational and rotational dynamic behavior at the coordinate 1 end are:

$$h_{11} = \frac{x_1}{f_1} \quad l_{11} = \frac{x_1}{m_1} \quad n_{11} = \frac{\beta_1}{f_1} \quad p_{11} = \frac{\beta_1}{m_1} \tag{6.14}$$

Then the cross receptances at the coordinate 1 end are:

$$h_{12a} = \frac{x_1}{f_{2a}} \quad l_{12a} = \frac{x_1}{m_{2a}} \quad n_{12a} = \frac{\beta_1}{f_{2a}} \quad p_{12a} = \frac{\beta_1}{m_{2a}} \tag{6.15}$$
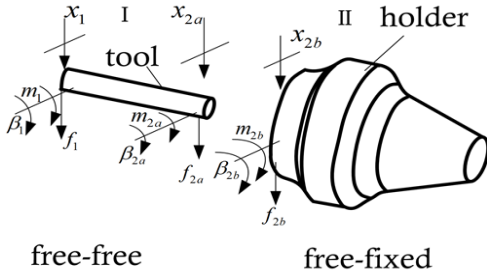
Fig. 80. Individual receptances model   Fig. 81. Receptances coupling model
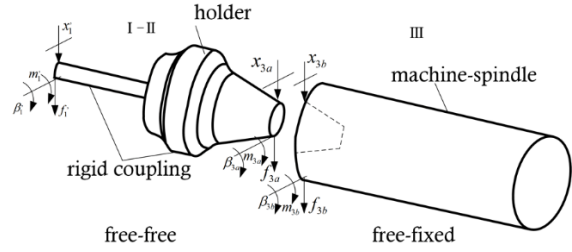
The direct and cross receptances at the coordinate 2a end are expressed as:

$$\begin{cases} h_{2a2a} = \dfrac{x_{2a}}{f_{2a}} \quad l_{2a2a} = \dfrac{x_{2a}}{m_{2a}} \quad n_{2a2a} = \dfrac{\beta_{2a}}{f_{2a}} \quad p_{2a2a} = \dfrac{\beta_{2a}}{m_{2a}} \\[2mm] h_{2a1} = \dfrac{x_{2a}}{f_1} \quad l_{2a1} = \dfrac{x_{2a}}{m_1} \quad n_{2a1} = \dfrac{\beta_{2a}}{f_1} \quad p_{2a1} = \dfrac{\beta_{2a}}{m_1} \end{cases} \tag{6.16}$$

For the free-fixed holder, the direct receptances at the coupling coordinate 2b end are obtained as:

$$h_{2b2b} = \frac{x_{2b}}{f_{2b}} \quad l_{2b2b} = \frac{x_{2b}}{m_{2b}} \quad n_{2b2b} = \frac{\beta_{2b}}{f_{2b}} \quad p_{2b2b} = \frac{\beta_{2b}}{m_{2b}} \tag{6.17}$$

where x is the displacement, f is the force, m is the bending couple and β is the rotation. The notations 1, 2a, 2b, 3a and 3b represent different receptances locations respectively.

Then the generalized receptances matrix R_{sk_v}, the substructure dynamics, can be given as:

$$R_{sk_v} = \begin{pmatrix} h_{sk_v} & l_{sk_v} \\ n_{sk_v} & p_{sk_v} \end{pmatrix} \tag{6.18}$$

where s represents measurement location and k_v represents excitation location. The four entries of R_{sk_v} are displacement-to-force, h_{sk_v}, displacement-to-couple, l_{sk_v}, rotation-to-force, n_{sk_v}, and rotation-to-couple, p_{sk_v}, respectively.

The assembly receptance G considering compatibility conditions at the end of coordinate 1 can be written as:

$$G_{11} = R_{11} - R_{12a}(R_{2a2a} + R_{2b2b})^{-1}R_{2a1} = \begin{pmatrix} H_{11} & L_{11} \\ N_{11} & P_{11} \end{pmatrix}$$

(6.19)

After the rigid coupling between the micro-milling tool and holder, the coupled components (I-II) can be viewed as a new component with free-free boundary conditions. Similarly, the direct and cross receptances of the coupled component (I-II) in Fig. 81 can be developed by replacing coordinate notations: substituting coordinate $\dot{1}$ for 1, coordinate 3a for 2a and coordinate 3b for 2b.

| (a) | (b) |
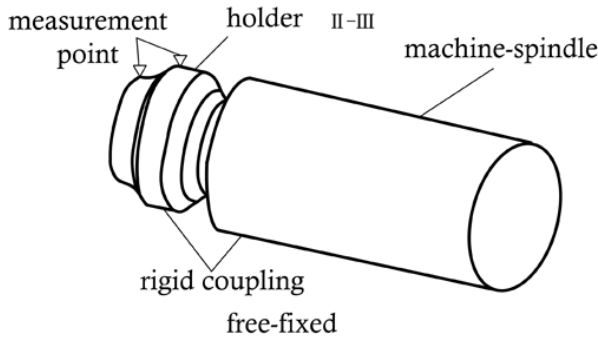
Fig. 82 (a). Inverse receptance coupling model Fig. 82 (b). EMA for holder-spindle-machine
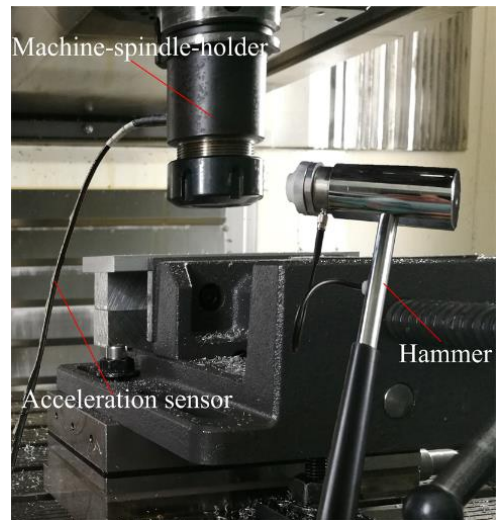
The final assembly receptance can be established as:

$$G_{11}' = G_{11} - G_{13a}(G_{3a3a} + R_{3b3b})^{-1}G_{3a1}$$

(6.20)

The assembly receptances G_{11}, G_{13a}, G_{3a3a} and G_{3a1} will be identified from corresponding coupled components, and R_{3b3b} can be developed with the method of "inverse RCSA" [1], as shown in Fig. 82.

$$R_{3b3b} = R_{3a2}(R_{22} - G_{22})^{-1}R_{23a} - R_{3a3a}$$

(6.21)

The assembly receptance $G_{22} = \begin{pmatrix} H_{22} & L_{22} \\ N_{22} & P_{22} \end{pmatrix}$ can be obtained straightforward through the EMA and "inverse RCSA". The Modal parameters of machine-spindle-holder are listed in Tab. 9. All the frequency of tool holder in Table 9 were measured in the X direction. The natural frequency measured at the end of tool holder and specified point fluctuated, while the stiffness nearly remained the same. This was probably because the acceleration sensor introduced additional mass for the measurement system, which may lead to the decrease of frequency. Therefore, the maximum frequency was applied to identify the FRF at the micro-milling tool point.

Table 9 Modal parameters of machine-spindle-holder

Direction	Natural frequency Min/Max (Hz)	Stiffness (N/m)	Modal mass Min/Max (kg)	Damping ratio (%)
X-Measurement	1089/1359	1.35×10^6	0.030/0.021	1
X-End	923/1023	9.51×10^5	0.028/0.024	1
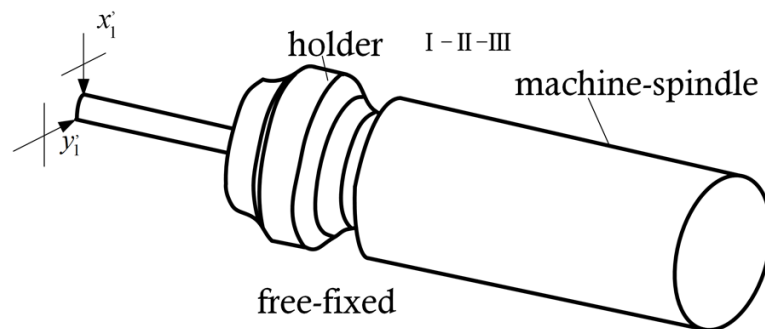
Fig. 83. FRFs at tool point of whole coupling model

6.2.2 FRF with different restricted/free overhang lengths

When the modal parameters of spindle-machine are identified through EMA, the FRFs at the end of spindle in X and Y direction are determined. As illustrated in Fig. 83, the receptance of micro-milling tool point in X direction, H_{11-x}, is identified and the receptance in Y direction, H_{11-y}, can also be identified similarly. The restricted/free overhang length is a significant component of individual substructure receptance, and different restricted overhang lengths of micro-milling tool clamped in the holder will cause the different free overhang lengths of the tool, which will affect the coupled receptances between the micro-milling tool and the holder. The curve fittings about FRF of micro-milling tool point in X and Y direction are performed based on the EMA and Eq. (6.20). As shown in Fig. 84, the three-dimensional

FRFs diagrams varying with restricted tool overhang length of the system for X direction is identified through the rigid coupling. As the micro-milling tool is regarded as a symmetrical cylinder, and modal parameters of X and Y direction are basically the same. Therefore, the three-dimensional FRFs diagrams for Y direction are nearly the same with X direction. It is worth mentioning that there is no specific law for the stiffness after coupling between restricted/free tool overhang length and tool holder. It is not that the longer the two coupled components length is, the lower the stiffness is [1]. The coupled stiffness depends on the characteristics of the tool and tool holder. Therefore, the combination of the two components can be used to adjust the stiffness of the tool point.
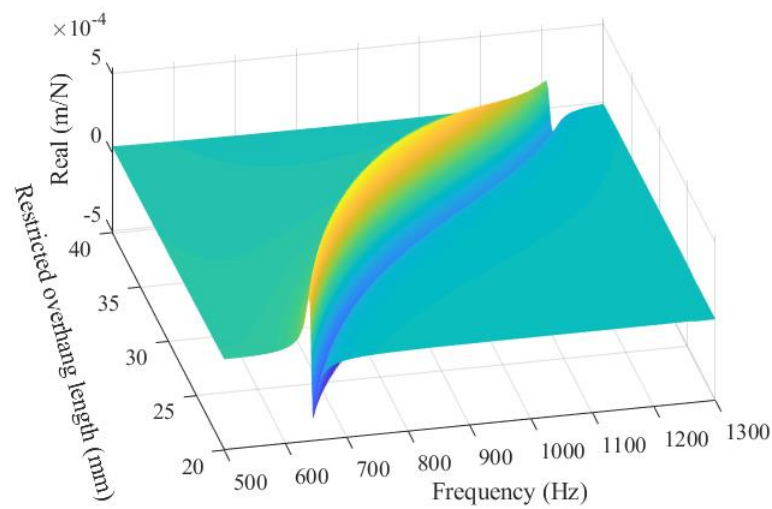
（a）
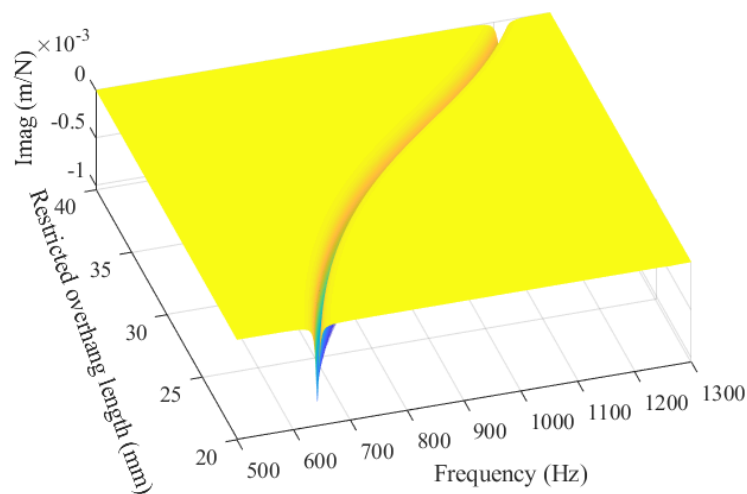
(b)

Fig. 84. Fitting diagram of FRF in X direction: (a) the real part, (b) the imaginary part

The cross FRFs (FRF_{xy} and FRF_{yx}) for micro-milling tool are set to zero because the radius of the micro-milling tool is small and the directions of X and Y are orthogonal, which makes

cross FRFs less obvious. The restricted/free tool overhang length in Z direction is considered as a function, and another form of FRFs in X and Y direction are established respectively. The first-order modal parameters are selected, and the direct FRFs can be written as

$$\text{FRF}_{xx} = H_{11-x}(z) = \frac{1}{-\text{M}_x(z)\omega^2 + i\text{C}\omega + \text{K}_x(z)}$$ (6.22)

$$\text{FRF}_{yy} = H_{11-y}(z) = \frac{1}{-\text{M}_y(z)\omega^2 + i\text{C}\omega + \text{K}_y(z)}$$ (6.23)

where M_x and M_y are the mass of micro-milling tool in X and Y directions, C is the structure damping, K_x and K_y are the stiffness of micro-milling tool in X and Y directions.

6.3 Stability and surface location error prediction

6.3.1 Establishment of SLE

During the interaction process between micro-milling tool and workpiece, dynamic response of micro-milling tool point and cutting force can bring about the displacement of tool in the corresponding directions, which also affects the machining accuracy. In this model, the cutting force for X and Y direction in the shearing zone can be written as

$$\begin{cases} F_x = \sum_{j=1}^{N} F_{x,j} = \sum_{j=1}^{N} [-K_t bh(\phi_j)\cos\phi_j - K_r bh(\phi_j)\sin\phi_j] \\ F_y = \sum_{j=1}^{N} F_{y,j} = \sum_{j=1}^{N} [-K_t bh(\phi_j)\sin\phi_j - K_r bh(\phi_j)\cos\phi_j] \end{cases}$$ (6.24)

The Fourier force model is used to solve the SLE, the function satisfying expansion conditions can be rewritten as:

$$f(x) = \frac{a_0}{2} + \sum_{n=1}^{\infty}(a_n\cos nx + b_n\sin nx)$$ (6.25)

where $a_0 = \frac{1}{\pi}\int_0^{2\pi} f(x)dx \quad a_n = \frac{1}{\pi}\int_0^{2\pi} f(x)\cos(nx)dx \quad b_n = \frac{1}{\pi}\int_0^{2\pi} f(x)\sin(nx)dx$

Then the Fourier transform is applied to F_x and F_y, and the integral force in X and Y direction can be developed as:

$$\begin{cases} F_x(\omega) = FFT\{F_x(\phi_j)\} = FFT\left\{\sum_{j=1}^{N}\left(a_{0x} + \sum_{n=1}^{\infty}(a_{nx}\cos(n\phi_j) + b_{nx}\sin(n\phi_j))\right)\right\} \\ F_y(\omega) = FFT\{F_y(\phi_j)\} = FFT\left\{\sum_{j=1}^{N}\left(a_{0y} + \sum_{n=1}^{\infty}(a_{ny}\cos(n\phi_j) + b_{ny}\sin(n\phi_j))\right)\right\} \end{cases}$$ (6.26)

During the machining process, the micro-milling tool contacts with the workpiece and the milling force acts on the interaction zone. The direct and cross receptances of the workpiece will be produced in X and Y direction under the action of micro-milling force which can cause the dynamic displacement of the micro-milling tool. Then the expression of displacements can be established through the corresponding FRFs and forces. Finally, the dynamic machining error can be obtained through the inverse Fourier transform. Therefore, Eq. (6.3) becomes

$$
\begin{cases}
x_t = x_f + r\sin(2\pi\Omega_1 t - \dfrac{2\pi j}{N}) + x_{FRF} \\[2mm]
y_t = r\cos(2\pi\Omega_1 t - \dfrac{2\pi j}{N}) + y_{FRF} \\[2mm]
\qquad x_f = Nf_z\Omega_1 t \\[2mm]
\quad x_{FRF} = x_{Txx} + x_{Txy} + x_{Wxx} + x_{Wxy} \\[1mm]
\quad y_{FRF} = y_{Tyy} + y_{Tyx} + y_{Wyy} + y_{Wyx}
\end{cases}
\tag{6.27}
$$

where x_{FRF} and y_{FRF} represent the theoretical value of SLE for X and Y directions respectively; the subscripts, T and W, represent micro-milling tool and workpiece respectively; x_{Txy} represents measurement in X direction with excitation in Y direction for micro-milling tool; the meaning of $x_{Txx}, x_{Wxy}, x_{Wxx}, y_{Tyy}, y_{Tyx}, y_{Wyy}$ and y_{Wyx} are similar to x_{Txy}.

As zero coupling between X and Y directions is assumed, the displacements, x_{Txy} and y_{Tyx}, equal zero in the Eq. (6.27). Then x_{FRF} and y_{FRF} become:

$$
\begin{cases}
x_{FRF} = IFFT\left\{\dfrac{X(\omega)}{F_x(\omega)}F_x(\omega)\right\} = IFFT\left\{\dfrac{X_{Txx}(\omega) + X_{Wxx}(\omega) + X_{Wxy}(\omega)}{F_x(\omega)}F_x(\omega)\right\} \\[3mm]
\qquad = IFFT\left\{(FRF_{Txx} + FRF_{Wxx} + FRF_{Wxy}) * F_x(\omega)\right\} \\[3mm]
y_{FRF} = IFFT\left\{\dfrac{Y(\omega)}{F_y(\omega)}F_y(\omega)\right\} = IFFT\left\{\dfrac{Y_{Tyy}(\omega) + Y_{Wyy}(\omega) + Y_{Wyx}(\omega)}{F_y(\omega)}F_y(\omega)\right\} \\[3mm]
\qquad = IFFT\left\{(FRF_{Tyy} + FRF_{Wyy} + FRF_{Wyx}) * F_y(\omega)\right\}
\end{cases}
\tag{6.28}
$$

6.3.2 Establishment of SLD

The dynamic cutting thickness in the shearing zone is employed to calculate and predict the stability of system with the static part ignored. Then the projections of the tangential and normal force in Eq. (6.24) onto the fixed (X and Y) coordinate frame are：

$$
\begin{pmatrix} F_x \\ F_y \end{pmatrix} = \frac{1}{2}bK_t \begin{bmatrix} a_{xx} & a_{xy} \\ a_{yx} & a_{yy} \end{bmatrix} \begin{pmatrix} \Delta x \\ \Delta y \end{pmatrix}
\tag{6.29}
$$

The time varying directional coefficients ($a_{xx}, a_{xy}, a_{yx}, a_{yy}$) can be found in the work of Altintas and Budak [5], and the dynamic equation of the system would be developed as:

$$\begin{cases} M_x\,\ddot{x}+C_x\,\dot{x}+K_x x = F_x \\ M_y\,\ddot{y}+C_y\,\dot{y}+K_y y = F_y \end{cases} \tag{6.30}$$

The limit depth of cut can be rewritten as:

$$b_{\lim} = -\frac{2\pi}{NK_t(\lambda_{Re}^2+\lambda_{Im}^2)}\bullet\lambda_{Re}(1+\frac{1}{\kappa^2}) \tag{6.31}$$

Then two new variables, λ and κ, are defined as:

$$\lambda=\lambda_{Re}+i\lambda_{Im} = \frac{4\pi}{NbK_t(1-cos(w_cT)+isin(w_cT))} \tag{6.32}$$

$$\kappa = \frac{\lambda_{Im}}{\lambda_{Re}} = \frac{-\sin\omega_cT}{1+\cos\omega_cT} = \tan\psi' \tag{6.33}$$

where ω_c is the chatter frequency, and ψ' is the phase shift of eigenvalue.

Then tooth passing periods and spindle speed can be expressed as:

$$T = \frac{1}{\omega_c}(\pi-2\psi'+2n\pi)=\frac{1}{\omega_c}(\varepsilon+2n\pi)\quad n=0,1,2,3\cdots \tag{6.34}$$

$$\Omega = \frac{60}{NT} \tag{6.35}$$

where ε is the phase shift between v_{j-1} and v_j.

Based on the above analysis, the calculation process of three-dimensional comprehensive diagrams combined SLE and SLD with considering restricted/free overhang length of micro-milling tool is detailed as follows:

Step 1. Use the method of RCSA and EMA to obtain the three-dimensional FRFs of micro-milling tool point in X and Y directions, which considers restricted/free overhang length of the micro-milling tool.

Step 2. Establish the dynamic equation of the system and use frequency domain method to calculate the limit depth of cut of the machining process with restricted/free different overhang lengths.

Step 3. Obtain the three-dimensional SLD with restricted/free tool overhang length as the variable.

Step 4. Apply the Fast Fourier Transform (FFT) to get $F(\omega)$. Then calculate the displacement in frequency domain and obtain displacement in time-domain through Inverse Fast Fourier Transform (IFFT).

Step 5. Obtain the predicted model of SLE by taking dynamics from both tool and workpiece in X and Y directions into consideration.

Step 6. Develop the three-dimensional SLE only in Y direction with depth of cut as the variable and choose parameters by combining the three-dimensional SLE and SLD comprehensively.

6.3.3 Identification for micro-milling cutting coefficients

The machining experiments were performed on a five-axis milling machine tool (DMU80 monoBLOCK by DMG MORI Co., Ltd.) with the experimental speed range from 10000 rpm to 18000 rpm. The experimental setup was shown in Figs. 85. A three-component piezoelectric dynamometer (Kistler 9257B) was fixed on the X-Y plane to measure forces in X and Y direction respectively. The workpiece was clamped by a fixture which was mounted on the dynamometer. The workpiece was made of aluminum alloy 2A12, and the basic parameters of the micro-milling tool were shown in Tab. 10. As shown in Figs. 86 and 87, the material of the cutting tool is cemented carbide K55SF (GUHRING Co., Ltd.). The two fluted micro end mill was fabricated with helix angle of 30°, rake angle of -3°, relief angle of 6°, first end teeth angle of 10° and second end teeth angle of 20°.
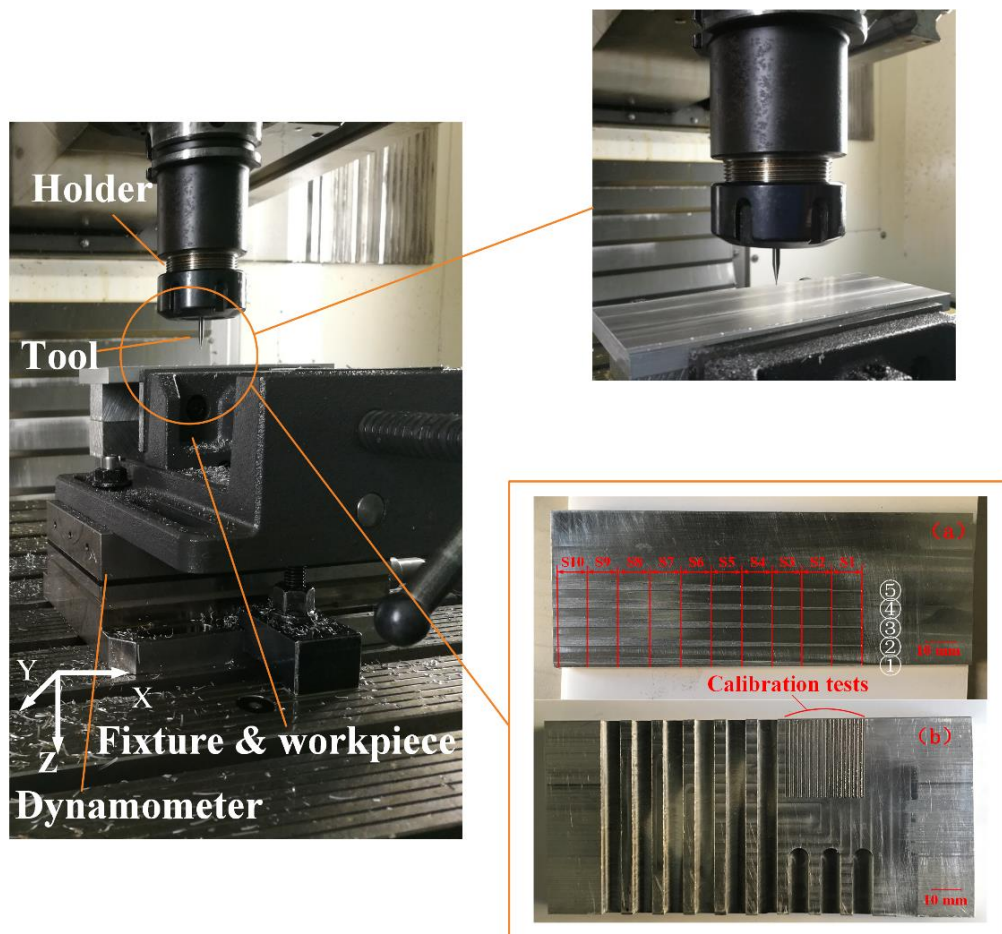

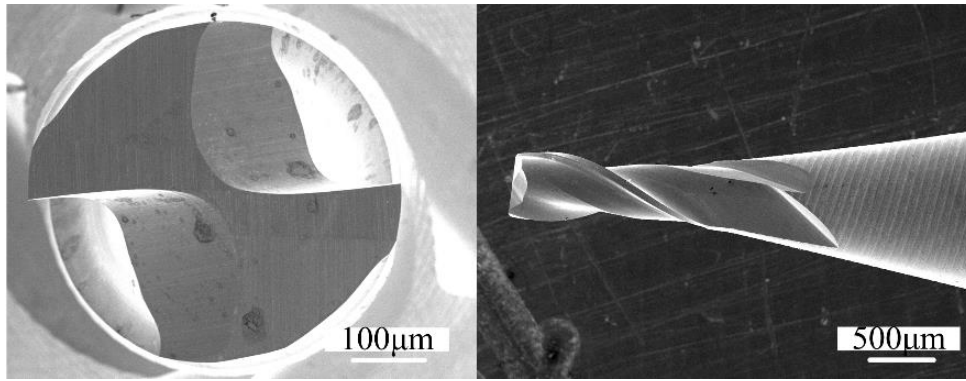Fig. 85. Experiment setup for micro-milling system

Fig. 86. Shape of micro-milling tool

Table 10 Parameters of micro-milling tool

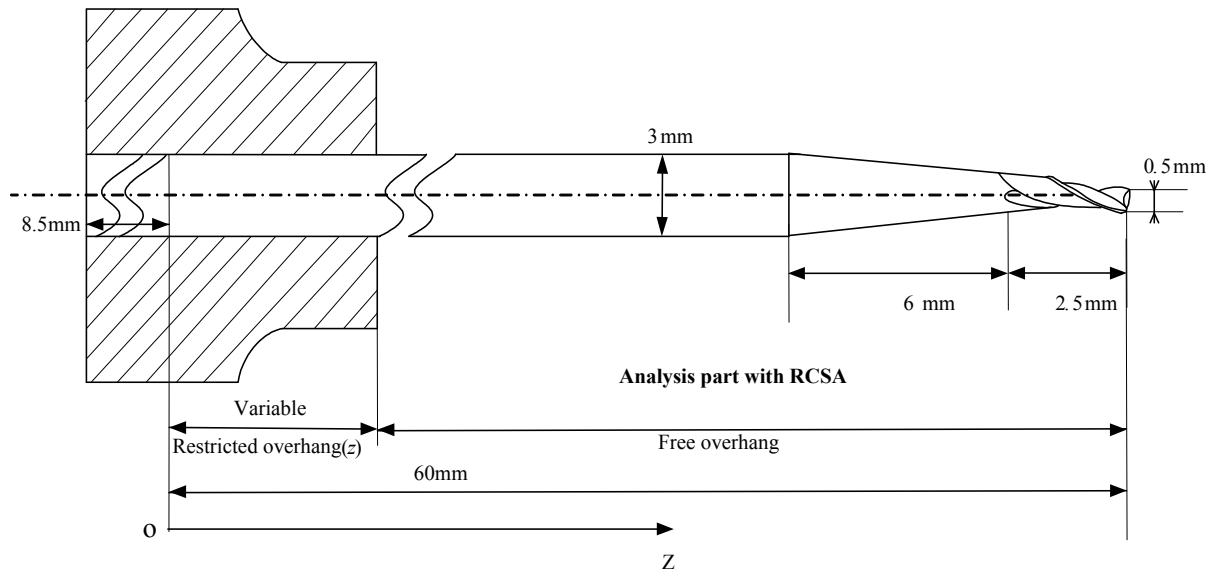| Geometric Property	Value
Cutting edge length (mm)	2.5
Diameter of cutting edge (mm)	0.5
Diameter of tool (mm)	3
Teeth number N	2
Tool length (mm)	68.5

Fig. 87. Clamping state of micro-milling tool

(a)   (b)
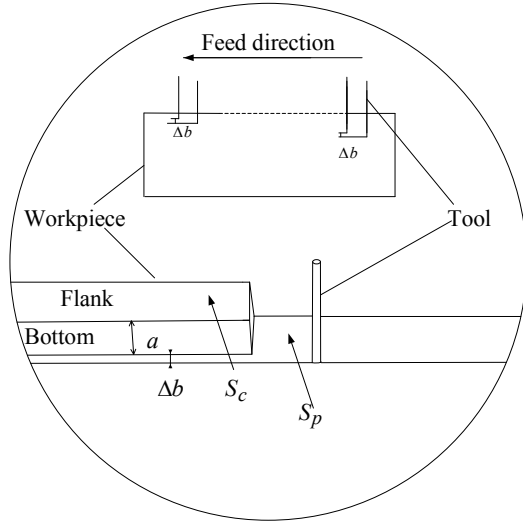
Fig. 88 (a). Schematic diagram of experimental   Fig. 88(b). Schematic diagram of experimental rib
workpiece
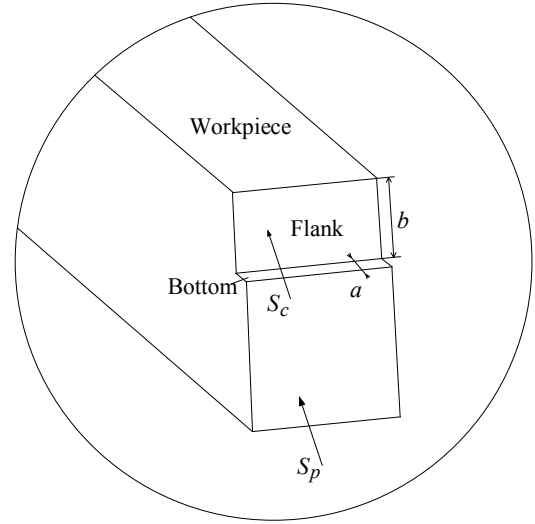
For the micro-milling, the difference between the current position vector, S_c, and the previous position vector, S_p, is the actual radial depth of cut, and the radial depth of cut, a, is the theoretical value. As shown in Fig. 88, the SLE measured by KEYENCE VK-100 can be written as:

$$SLE_m = \left| S_c - S_p - a \right| \tag{6.36}$$

As shown in Fig. 85, two sets of data for different depth of cut and feed per tooth were collected to calibrate the tangential cutting force coefficient, K_t, and the normal force coefficient, K_n. The spindle speed was 10000 rpm with full immersion (slotting), and the depth of cut was 20 μm and 50 μm respectively. The experimental results containing mean micro-milling forces and root mean square value of the resultant force were shown in Tab. 11.

Table 11 Two sets of data for micro-milling forces

No.	Feed per tooth (μm/tooth)	Depth of cut (μm)	$\bar{F}_x(N)$	$\bar{F}_y(N)$	Resultant force $\bar{F}(N)$
1	0.2	20/50	0.137/0.256	0.090/0.120	0.16/0.28
2	0.5	20/50	0.086/0.250	0.041/0.160	0.10/0.30
3	0.8	20/50	0.021/0.091	0.118/0.310	0.12/0.32
4	1	20/50	0.050/0.384	0.204/0.441	0.21/0.58
5	1.5	20/50	0.063/0.380	0.224/0.704	0.23/0.80
6	2	20/50	0.072/0.587	0.305/0.758	0.31/0.96
7	3	20/50	0.086/0.660	0.377/0.872	0.39/1.10
8	4	20/50	0.140/0.754	0.394/0.962	0.42/1.20
9	5	20/50	0.367/0.839	0.483/1.220	0.61/1.50
10	6	20/50	0.463/1.190	0.607/1.310	0.76/1.80
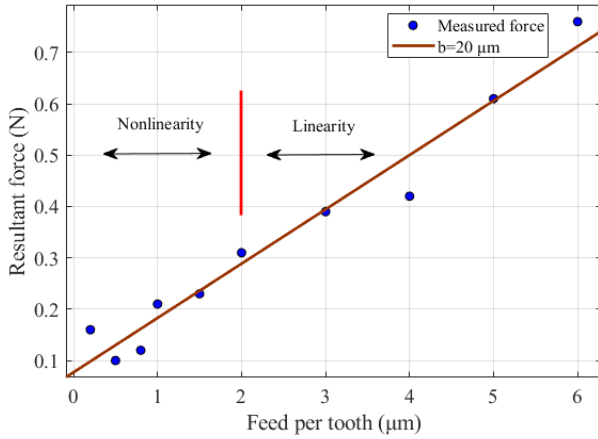
Fig. 89. Resultant forces with depth of cut of 20 μm   Fig. 90. Resultant forces with depth of cut of 50 μm
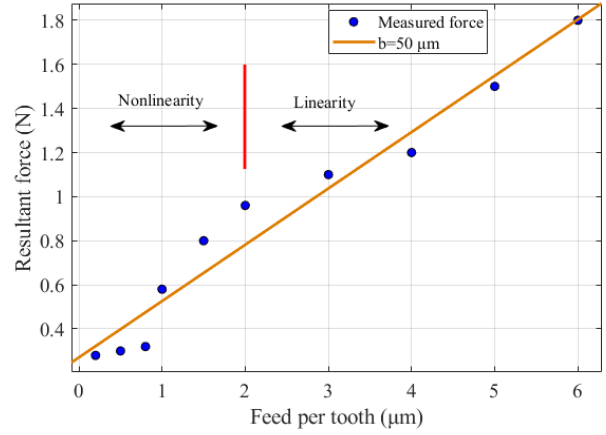
As can be seen from Figs. 89 and 90, the experiment showed that for feed per tooth which is larger than approximately 2 μm, the resultant force depicted a linear trend. Therefore, the value of feed per tooth over 2 μm was used to establish the coefficients.
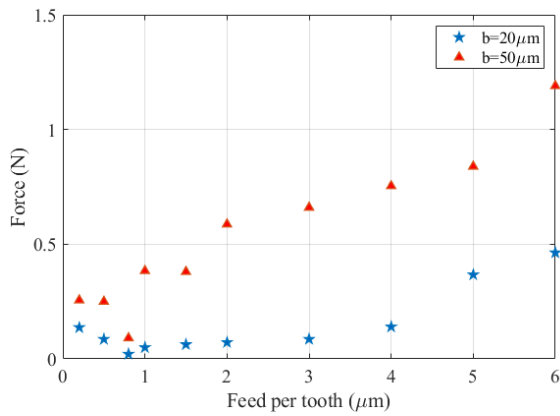
Fig. 91. Forces in X direction with two depth of cut   Fig. 92. Forces in Y direction with two depth of cut
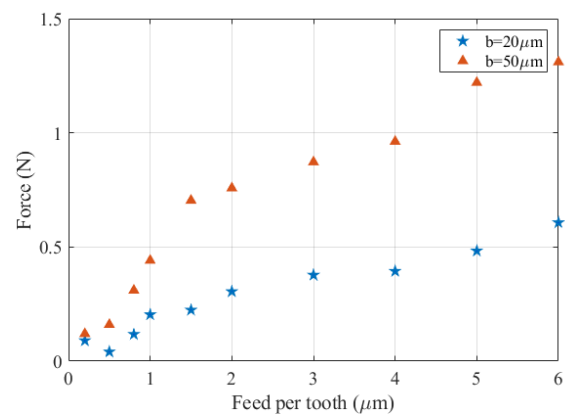
As shown in Figs 89, 91 and 92, the data of No.1 and No.3 did not lead the cutting forces to an upward trend with the feed per tooth becoming higher, and this phenomenon mainly occurred in X direction with depth of cut of 20 μm. That was probably because the smaller depth of cut and characteristics of workpiece. In this case, the characteristics of workpiece mainly included two aspects: the non-uniform distribution of hardness and flatness error of the workpiece. For the data of No.3, the hardness distribution of the workpiece was non-uniform in the two directions, and it led to a relatively small force in X direction and high force in Y direction. For the data of No.1, it was possible that the smaller depth of cut and flatness error made the actual depth of cut larger than the theoretical value of 20 μm. However, the calibration data were based on the data after No.5, so the data of No.1 and No.3 would not affect the whole calibration process.

Although the depth of cut was obviously different, the slopes of forces remained basically the same for corresponding directions. Finally based on Eq. (6.13), the milling coefficients could be solved as: $K_n = 5.4 \times 10^3$ N/mm^2, $K_t = 5.9 \times 10^3$ N/mm^2.

6.4 Cutting tests and discussion

6.4.1 The influence of restricted/free overhang length on SLD

When the modal parameters were identified from Fig. 84, the stiffness of the tool point varies between 1×10^4 N/m and 2×10^4 N/m. Due to the complexity of the micro-milling process, the conservative SLD is adopted to ensure that the parameters are available, which is similar to Chapter 5. In order to obtain the robust machining parameters, the stiffness of the tool point applied to the SLD calculation is reduced to no more than 1×10^4 N/m. Using Matlab to simulate the calculation steps, the three-dimensional SLD was shown in Fig. 93.
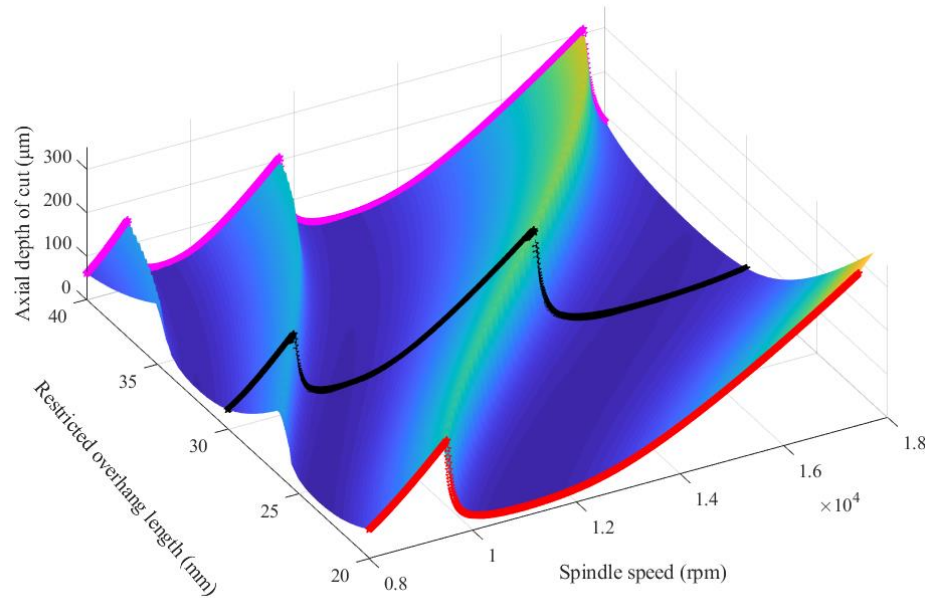
Fig. 93. Three-dimensional SLD with restricted tool overhang length

As shown in the Fig 85, the label ①-⑤ marked in workpiece corresponded to the spindle speed 11000 rpm, 12000 rpm, 13000 rpm, 14000 rpm and 15000 rpm with same restricted tool overhang length respectively. The feed per tooth is 8 μm/tooth, and the radial depth of cut is 300 μm. Experiments for down micro-milling were carried out by these above machining parameters. If the ratio of magnitude at the chatter frequency to the magnitude at the tool passing frequency in the frequency spectrum is larger than 0.005, the process is viewed as instability [12]. Due to the small scale of micro-milling, the sound signal collected from the cutting process is very weak, combined with the noise caused by the movement of machine tool, so it is difficult to determine the chatter frequency through the sound spectrum. As the

workpiece is always in contact with the dynamometer, the cutting force signal is applied to identify the machining frequency. But the dynamometer may be interfered by the spindle speed in the process of cutting force acquisition. When the cutting force signal was weak, it could only be used to help to judge whether chatter occurs. Therefore, the chatter determination of the micro-milling process must depend on the surface topography of the machined workpiece.
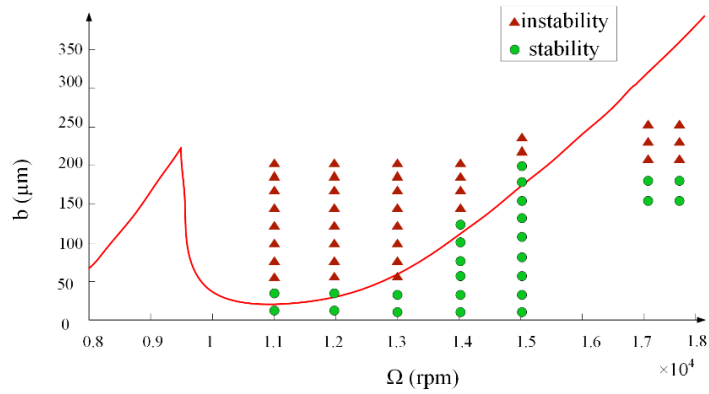
(a)
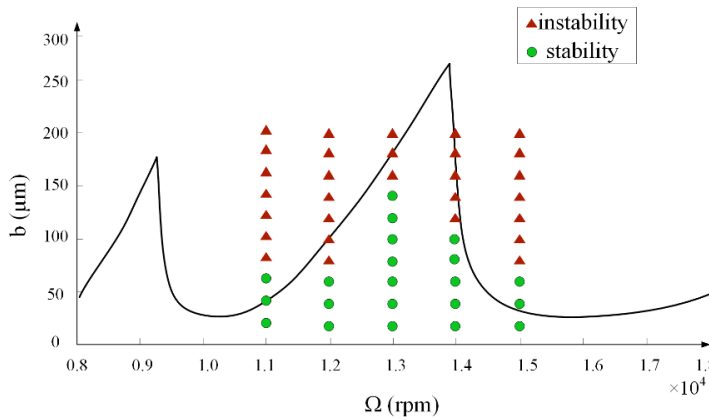
(b)
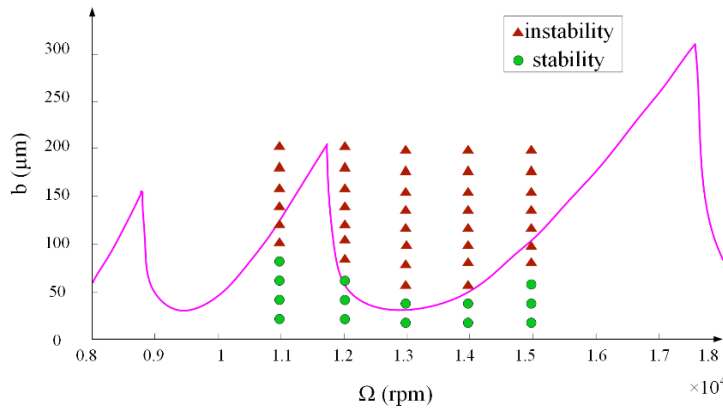
(c)

Fig. 94. (a) Two-dimensional SLD with restricted overhang length 20 mm; (b) Two-dimensional SLD with restricted overhang length 30 mm; (c) Two-dimensional SLD with restricted overhang length 40 mm

As shown in Fig. 94, the three two-dimensional SLD were intercepted from the three-dimensional SLD illustrated in Fig. 93 at different restricted tool overhang lengths. As shown in Fig. 94 (a), the spindle speed of 15000 rmp with restricted overhang length of 20 mm was selected, and experiments were carried out with depth of cut decreasing from 200 μm to 20 μm (Δb=20 μm), which can be seen in Figs. 85 (a) and 88 (a). Therefore, the machining test were divided into ten milling stages (from S1 to S10). As presented in Fig. 95, the milling force signal was collected and the time-domain cutting force signal was transformed into frequency domain by FFT. The frequency distribution was observed from the frequency spectrum, and the chatter frequency was not found. Then the spindle speed of 13000 rpm was tested according to the above method. As presented in Fig. 96, the frequency distribution was observed from the frequency spectrum, and the chatter frequency was found besides spindle frequency, tooth passing frequency and its harmonics. Then the spectrum of force at each stage was analyzed separately, it showed that chatter frequency occurred from the first stage (b=200 μm) and did not disappear until the eighth stage (b=40 μm), which seems to be in good agreement with the two-dimensional SLD. Then different spindle speeds, 11000 rpm, 12000 rpm and14000 rpm, were used to verify the diagram. Similarly, other points in the Figs. 94 (b) and 94 (c) were also verified.

(a)

(b)
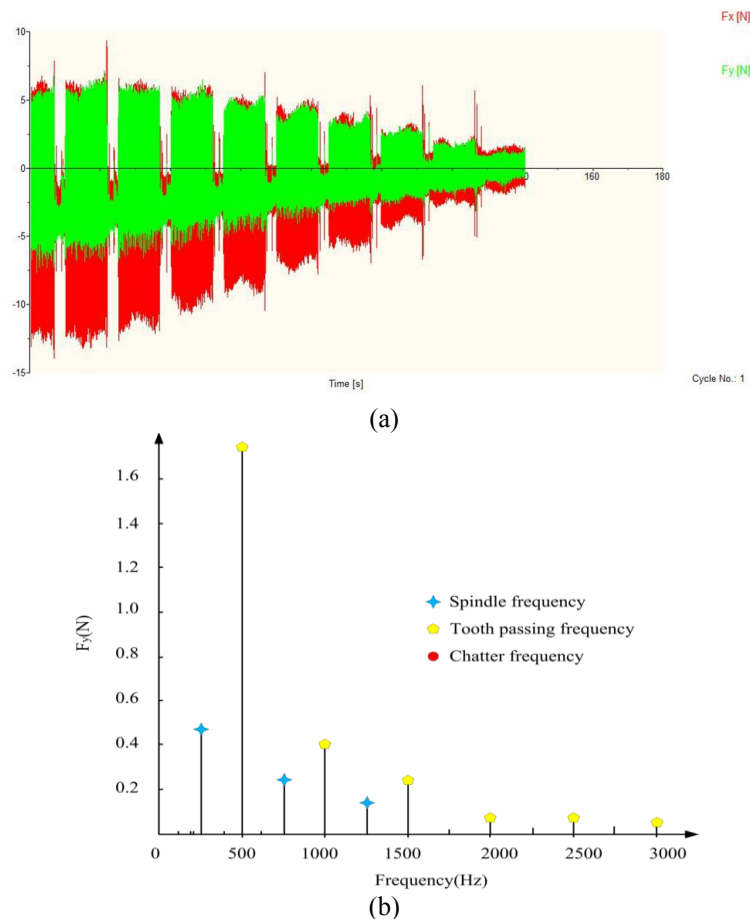
Fig. 95. (a) Forces for X and Y direction at 15000 rpm; (b) Frequency distribution for Y direction at 15000 rpm
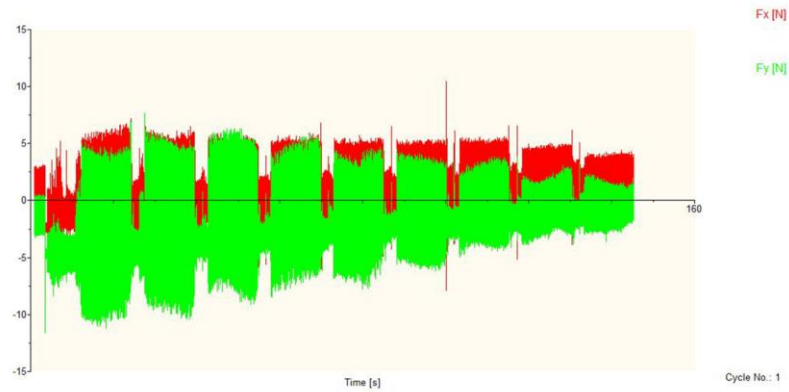
(a)
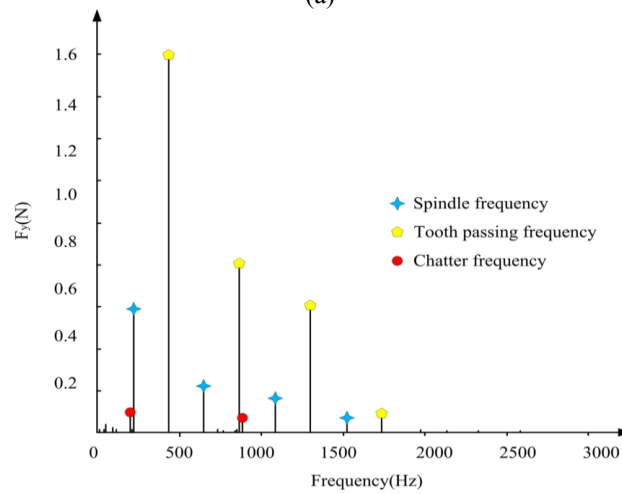
(b)

Fig. 96. (a) Forces for X and Y direction at 13000 rpm; (b) Frequency distribution for Y direction at 13000 rpm

Compared with unstable machining process in time-domain, the ten milling stages under stable condition had an obvious trend from large to small. As shown in Fig. 97, the flank-milling results also showed that in the unstable region machined surface topography left chatter marks, and in the stable region machined surface topography was glossy and smooth. In order to obtain a larger measurement area in flank, the workpiece shown in Figs. 85 (b) and 88 (b) was machined with two times for Fig. 97 (a) and six times for Fig. 97 (b) respectively.

Fig. 97. (a) Surface topography under unstable condition (Ω=13000 rpm, f_z=8 μm/tooth, b=80 μm, restricted overhang=20 mm); (b) Surface topography under stable condition (Ω=15000 rpm, f_z=8 μm/tooth, b=25 μm, restricted overhang=20 mm)

The experimental results matched well with the three-dimensional SLD except vicinity of the lobe boundary. It was mainly because there were uncertain parameters associated with these inputs, and the approximations of the stability algorithms also limited the accuracy. The prediction trend of the SLDs in Fig. 94 was similar. When the prediction and verification between Figs. 94(a) and 94 (c) were compared, the frequency difference caused by the restricted tool overhang length was further explained, which made the lobes shift in translational direction. Besides, another twelve points in Fig. 94 (a) with spindle speed 15000 rpm, 17000 rpm and 18000 rpm were tested, because the theoretical lobe boundary seemed to deviate from reality. It was possible that the next lobe did not intersect with the current lobe and variation of modal parameters might be the other reasons. However, Fig. 97 showed that the chatter marks on the bottom of the workpiece were not obvious, no matter whether chatter occurred. The roughness value at bottom was Ra=0.6 μm and Ra=0.4 μm for Figs. 97 (a) and 97 (b) respectively. It was possible that the contact between edge of micro-milling tool and the workpiece improved the stiffness at the end of the tool a lot. Then chatter had little effects on the surface topography at the bottom of workpiece.
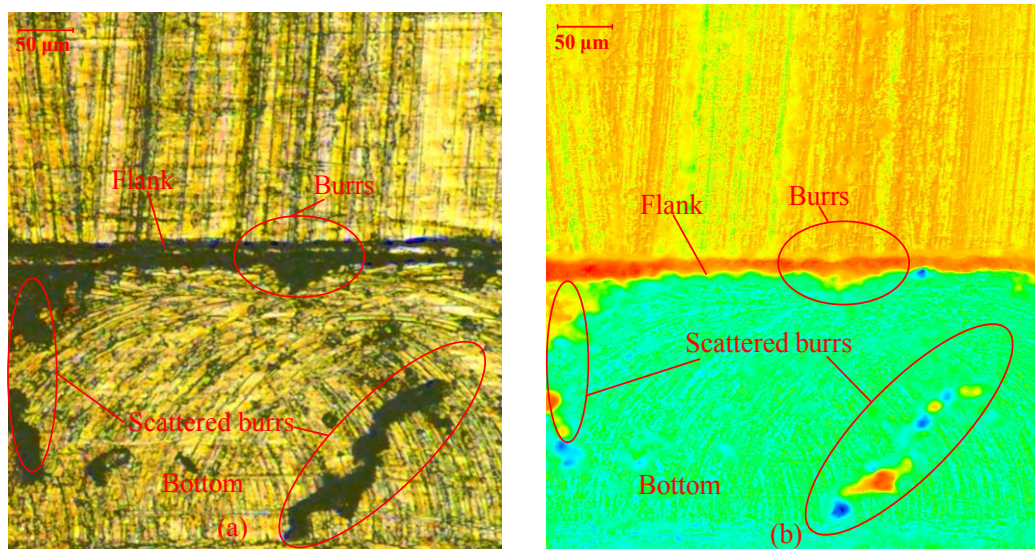
Fig. 98. Surface topography under stable condition (Ω=15000 rpm, f_z =8 μm/tooth, b=25 μm, restricted overhang=20 mm); (a) Surface topography by laser scanning (b) Surface topography with color

From the surface topography in Figs. 98 (a) and 99 (a), it could be seen that the distribution of micro burrs after machining was not very regular. Some burrs were attached to the edge of micro-milling tool and workpiece, mainly gathering at the corner above the flank, and the other parts were scattered on the surface of workpiece due to the vibration. As shown in Figs. 98 (b) and 99 (b), the height of burrs after unstable machining was larger than that after stable machining, because the corresponding depth of cut was larger during unstable processing. Then the contact area between edge of micro-milling tool and flank of workpiece was larger,

so there would be more burrs accumulation under unstable condition. Except for the relatively uniform distribution of burrs under stable condition, there was no apparent differences in both machining conditions: stability and instability. That was probably because chatter was not the main factor to constrain the formation of burrs.
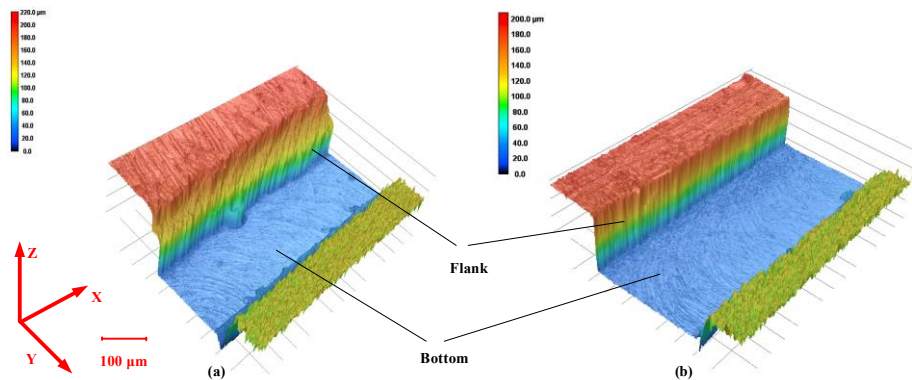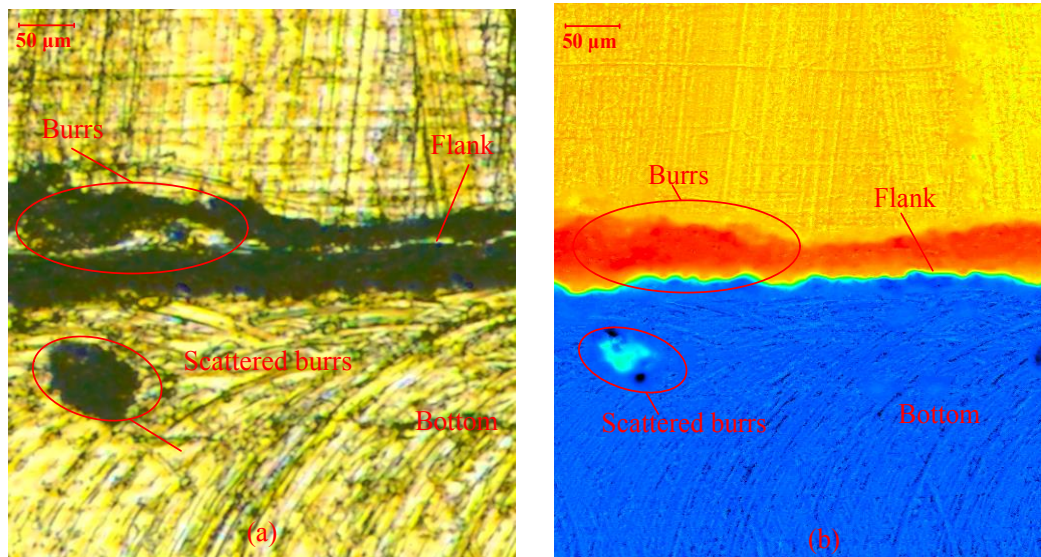

Fig. 99. Surface topography under unstable condition (Ω=13000 rpm, f_z =8 μm/tooth, b=80 μm, restricted overhang=20 mm); (a) Surface topography by laser scanning (b) Surface topography with color

6.4.2 The influence of restricted/free overhang length on SLE

As listed in Tab. 12, EMA method was applied to the workpiece clamped on the machine tool to identify the first-order modal parameters.

Table 12 Direct and cross response for workpiece

Direction	Natural frequency (Hz)	Stiffness (N/m)	Modal mass (kg)	Damping ratio (%)
FRF_{Wxx}	1442	1.15×10^7	0.14	1.5
FRF_{Wxy}	1334	1.1×10^7	0.16	1.5
FRF_{Wyy}	1531	1.05×10^7	0.11	1.5
FRF_{Wyx}	1409	1.22×10^7	0.16	1.5

Based on Eq. (6.3), the geometric trajectory of the micro-milling without dynamic effects could be obtained. The SLE was directly derived from the displacement caused by the dynamic response of the system, and it corresponded to the surface waviness. The machining parameter (15000 rpm, 60 μm) from stable region was selected, and the milling experiment (Δb=0, Figs. 85 and 88 (a)) were carried out with different restricted tool overhang lengths. Before measurement the workpiece was treated in the ultrasonic cleaning machine and the burrs were removed to the maximum extent. The results of the SLE measured in the stable region were illustrated in Fig. 100. As can be seen from Fig. 100, all the errors were within

102

the range of 15 μm, and the experimental results were all undercut situations. That is, s_c - s_p is less than a. The new trajectory of X versus Y coordinates considering dynamic effects was nearly the same as the former geometric trajectory due to the small value of feed per tooth. By calculation of Eq. (6.28), the theoretical value was about 7 μm (restricted overhang length: 40 mm；the spindle speed: 15000 rpm；the axial depth of cut: 60 μm). In fact, there would be corresponding dynamic displacement in the X direction, but lots of intersections would be generated. Besides, the continuous feed along X direction only affected the actual feed per tooth, so the subsequent SLE was analyzed only in Y direction.
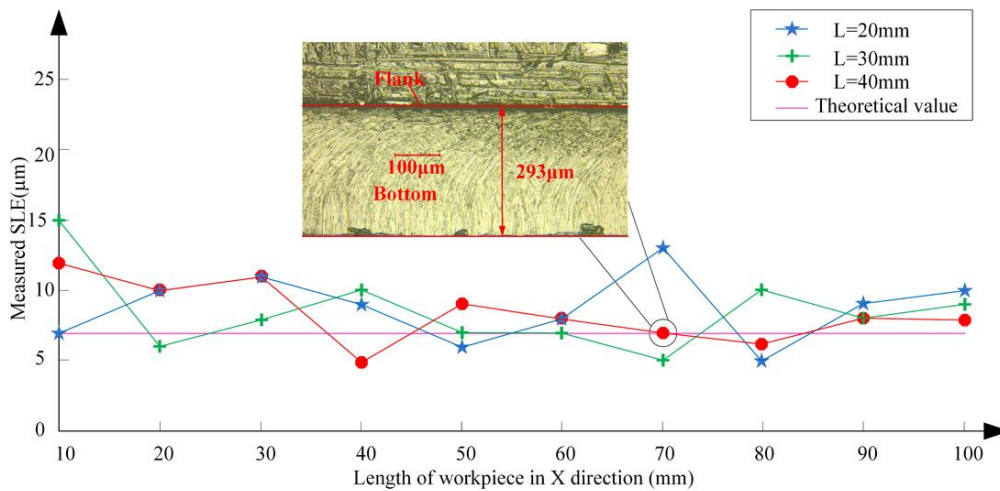
Fig. 100. Different overhang lengths vs SLE

The FRFs were measured directly in the experiment instead of designing a platform to calculate the FRFs, which is different from the experimental scheme in Ref [43]. According to the experimental results, the stiffness of workpiece under clamping condition was much greater than that of micro-milling tool, so the frequency response of workpiece may not have too much influence on the SLE. In addition, the machining scale for micro-milling was very small, and it is very hard to separate the error. Compared with macro-milling process, the SLE of micro-milling was difficult to trace the source. Therefore, the error was analyzed qualitatively in the experiment.

As the restricted overhang length was 40 mm, the stiffness of the tool point reached its maximum. When the order of magnitude of the tool stiffness is 10^4 N/m, the predicted SLEs from the micro-milling tool are even greater than the radius of the tool, which obviously does not accord with the measurement. When the order of magnitude of the tool stiffness are is 10^5 N/m, the predicted SLEs from the micro-milling tool are around 100 μm, which does not match with the experiment results. When the order of magnitude of the stiffness is 10^6 N/m, the theoretical value of SLE calculated in Y direction was about 7 μm which contained 5 μm

from the tool and the other 2 μm from the workpiece dynamics (restricted overhang length: 40 mm；the spindle speed: 15000 rpm；the axial depth of cut: 60 μm). In this case, the simulation result seemed to match well with the measurement. Combined with the above unstable machining parameter, there is no vibration mark at the bottom of the workpiece. It further shows that the effective support of the bottom may enhance the stiffness of the tool point, which is also inconsistent with the macro-milling process. Compared with the FRFs of tool, the direct and cross FRFs of workpiece measured by EMA were constant with small value due to its large stiffness. Besides, from Eq. (6.28) and Tab. 12, it can be seen that the FRF caused by workpiece dynamics accounted for little proportion of the whole FRFs. From the experimental results, it can be seen that the measured results were in good agreement with the predicted model (within ±3 μm) when the stiffness of 10^6 N/m of micro-milling tool was applied. It also showed that the change of restricted tool overhang length might have little effect on the SLE because of the existence of measurement error and the uncertainty. Another pivotal factor is the burr. The measurement cannot be conducted with the burrs. However, the actual machining dimension of the workpiece would be changed when the burrs were removed, which is very tricky to deal with. The measured SLE mainly depended on the location of parallel lines. The difference value between s_c and s_p increases as the notches

left by the burr root make the current position vector s_c larger. As a result, the measured values become smaller according to Eq. (6.36), and this is the main reason why the measured values are small (undercut situation). The peaks and troughs used to evaluate the roughness would limit the location of the measured parallel lines, so the roughness became another factor to influence the measured SLE. In this experiment, the flank roughness value of Fig. 97 (b) was about Ra=0.9 μm, which contributed to the error range, i.e. ±3 μm. That can also explain why under stable conditions a smaller SLE would be obtained.
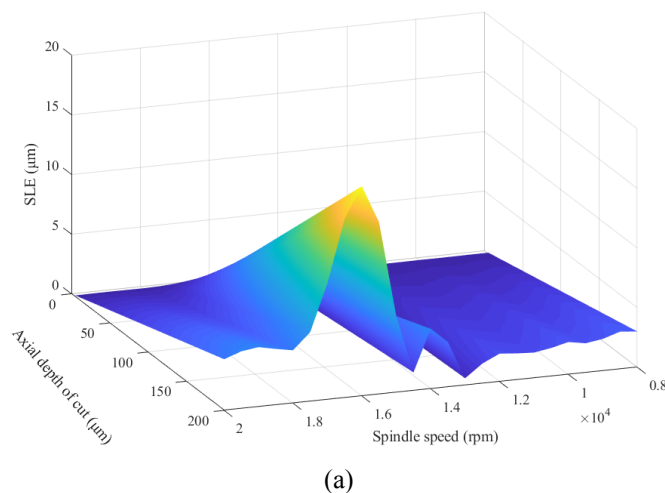
(a)
Fig. 101 (a). Three-dimensional SLE from workpiece

(b)
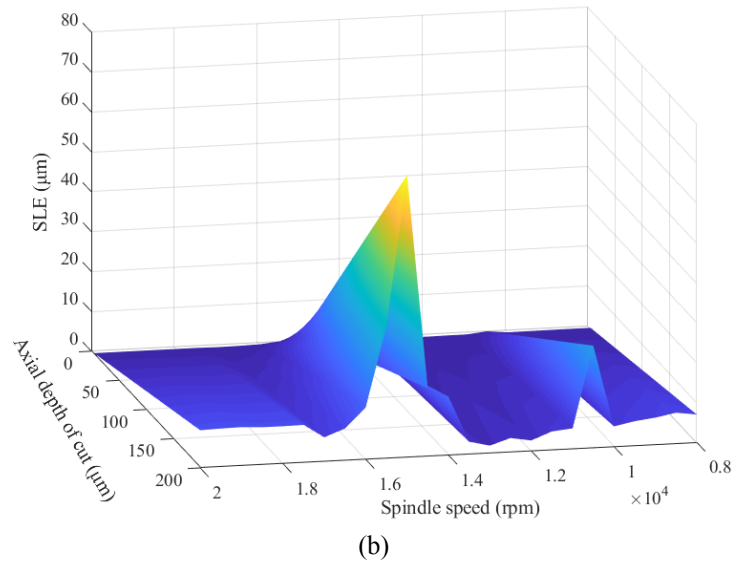
Fig. 101 (b). Three-dimensional SLE from micro-milling tool with assumption stiffness of 10^6 N/m

As the depth of cut directly affects the cutting force, the system would generate different displacement responses according to different forces. Once the feed per tooth is determined (in this case f_z =8 μm/tooth), the three-dimensional SLE diagram with different depths of cut can be drawn as Fig. 101.

Therefore, the two three-dimensional diagrams should be considered comprehensively when it comes to the selection for machining parameters, so that an optimal restricted/free overhang length, suitable depth of cut and spindle speed can be obtained to achieve the balance between stability and accuracy.

6.5 Summary

In this chapter, a simplified model for micro-milling and two three-dimensional diagrams were proposed comprehensively. The three-dimensional conservative SLD with variation restricted/free tool overhang length and the predicted model of SLE including the multi-directional FRFs of the tool and workpiece matched with the experimental results. This means the stability analysis of macro-milling is applicable for micro-milling. The following conclusions can be drawn:

There was a discrepancy between the stiffness at the tool point identified under static condition and the actual machining process. The model of micro-milling force proposed with some assumptions could predict the SLD and SLE, and the restricted/free tool overhang length affected the SLD indirectly by the change of FRFs at the micro-milling tool point. Under the condition of stable micro-milling, changes of restricted/free tool overhang length would not result in obvious changes of SLE, and the change of restricted/free tool overhang length had more significant influence on SLD than that on SLE as validated by the

corresponding experiments. As the burrs appearing during the machining process are major obstacles, the variation of SLE is mainly affected by the depth of cut when the distribution of burrs is ignored.

Regenerative chatter in micro-milling was still an important factor that restricted the machined surface quality. For flank micro-milling, the quality of surface topography under stable condition was better than that under unstable condition, but the chatter marks at the bottom of the workpiece were not obvious in both two machining conditions. Unlike macro milling process, the bottom support of the workpiece may increase the rigidity of the micro-milling tool. Besides, there was no significant differences for distribution of burrs in both machining conditions: stability and instability.

The dynamic behaviors of the system were dependent on the frequency responses of the tool point and workpiece. Based on the two three-dimensional diagrams, reasonable machining parameters and restricted/free tool overhang length were selected to avoid chatter vibration and ensure the surface precision in the practical processing.

According to experimental results in micro-milling there was a certain gap in terms of the prediction for SLD and SLE, and these two diagrams can only observe the general trend. It is much more difficult to predict the SLD and SLE for micro-milling than that of macro-milling because of the small machining scale, tool runout, nonlinear factors during the machining process and the cutting force coefficients that may vary with the spindle speed [106]. Meanwhile, micro-milling requires higher precision of measuring apparatus, which also brings difficulties for measurement.

7 Conclusion and outlook

In this dissertation, the SLDs and SLEs, which take into account the dynamic response of the IPW, are studied from both the macro and micro perspective. Firstly, based on the existed stability prediction methods, two novel methods are introduced. For macro-milling, the time-varying dynamics of workpiece is mainly studied. Then the stability prediction model of thin-walled workpiece considering in-process dynamics and process damping is established, and the SLE with continuous material removal is introduced subsequently. For micro-milling, because the micro-milling tool is more flexible than that of the workpiece, thus the dynamic response of the tool point is analyzed first. With the dynamics of workpiece obtained by experimental modal analysis, the SLD and SLE of micro-milling are developed. The conclusions of this dissertation are as follows:

For macro-milling, two complex machining situations are studied: milling of thin-walled workpiece and continuous radial milling of general workpiece. In both cases, it has been shown that material removal significantly affects the dynamics of the workpiece, mainly in terms of the natural frequency and amplitude of the IPW. Therefore, it is of practical importance to consider the incorporation of the dynamics of the workpiece into the dynamic analysis so that the diagram is closer to the real machining situation.

It is an effective method to identify the response of workpiece at the cutter-location point by using geometric conditions to determine the mass and stiffness variation matrix of the material to be removed. When machining a flexible system, the dominant modes switch between the workpiece and the milling tool, even though the workpiece is less rigid than the tool. The modes of tool are still excited, mainly due to the cutting forces during the interaction between the workpiece and the tool. Particularly at the low speed region where the axial depth of cut is greater (higher cutting forces), the process damping force consumes some of the vibration energy. At this point, the modes of milling tool are likely to be excited. At the high speed region where the process damping effect is less pronounced, large axial depth of cut will destabilize the cutting process and small axial depth of cut cannot excite the modes of the tool. Therefore, the modes of the workpiece dominate the entire machining process in this situation. For this reason, the established SLDs with considering the process damping and multiple mode shapes are more useful for machining the thin-walled weakly rigid workpiece.

For general workpiece with continuous milling, dynamic tests should be carried out in advance to ensure that the extracted mode shapes are closer to the real situation when the clamping height of the workpiece is small. Compared to machining the thin-walled workpiece, the dynamics of the general workpiece varies more significantly. Conservative

SLDs, which take the dynamics of IPW into account, can provide stable machining parameters in this case. With stable machining parameters, SLEs under continuous machining condition are more complex. The proposed model provides a good prediction of the error as well as robust parameters for the operators at the same time. Furthermore, in addition to the dynamics of the system including both tool and workpiece, which can influence SLEs, the measurement errors caused by the flank and bottom surfaces of the workpiece cannot be ignored either. The SLE of macro-milling process is therefore a combination of the dynamics of the system, roughness and measurement errors.

In micro-milling process, the methods for predicting macro SLD and SLE are still applicable. The restricted/free overhang length has a greater effect on SLD and almost no effect on SLE. Unlike macro-milling, the cutting forces in micro-milling are very low both in down-milling (separation in Fig. 53a) and up-milling (approach in Fig. 53d). The dynamic response of the micro-milling tool point always plays a dominant role due to the much less rigid tool. However, there is a discrepancy between the identified stiffness of tool point and the machining stiffness of tool point. The bottom support of the workpiece may increase the stiffness of the tool point due to the smaller geometry of the tool, which is not consistent with macro-milling. The burrs formed during micro-milling process pose a significant challenge for error measurement. Further analysis of SLEs is only possible when the effects of burrs are ignored, which is also clearly different from macro-milling process. However, the proposed SLDs and SLE diagrams can still provide a basis for the selection of parameters and the evolution of machining trends.

We must realize that the interaction between machine tool and machining process is very complicated, and it involves many factors of the system. Accordingly, there are still many issues worthy of further study.

The SLD mainly reveals the relationship between spindle speed and axial depth of cut during the process of tool-workpiece interaction, and the complicated interaction brings great challenges to the stability analysis of flexible milling system. In chapter 4, though the stiffness of the thin-walled workpiece was lower than that of the tool, the vibration mode of the tool was still excited during milling. When the modes of workpiece dominated the machining process, the change of the modal parameters would affect the SLD with the material removal. It was obvious that the dominant modes of machining system were transferred between the milling tool and workpiece. As different vibration modes correspond to different SLDs, accurate acquisition of dominant modes of the system is the key to obtain

the precise boundary of the SLD. Therefore, the determination of dominant modes and the analysis of modes transformation mechanism during material removal are the main research directions in the future.

For thin-walled workpiece, the difference of SLD with and without material removal was not very large. This was because the critical depth of cut was very small, and its change in such a small range was not obvious (Chapter 4). However, the smaller depth of cut had little significance for improving machining efficiency. For thin-walled workpieces, reducing radial immersion would increase the critical depth of cut, but smaller radial immersion would induce the bifurcation easier. Apart from SLD prediction, the focus should be on how to improve stiffness of workpiece to obtain a larger critical depth of cut. Therefore, under the given cutting conditions of milling tool and workpiece, the use of attaching mass or passive support for the thin-walled workpiece to improve the stability boundary is also a possible research direction.

For the workpiece from thick to thin-walled state, the critical depth of cut changed obviously (Chapter 5). That is, the dynamics of workpiece dominated the processing process and had a very significant influence on the machining process. Accordingly, it is inappropriate to use the modal parameters of machine tool-spindle-tool as the modal parameters of the system directly without analyzing the dynamic response of the workpiece, which would bring great risks to the machining process.

For micro-milling, due to the size effect and other factors different from macro-milling, the whole process of machining interaction is more complicated. The micro-cutting models are more difficult to develop than the conventional cutting models. Besides, there are many choices in the selection and simplification of models, and it is difficult to apply the impact tests to micro-milling tools directly, which brings great difficulties to the verification of FRF. Due to the emergence of burrs, small milling force and amplitude in spectrum, it is more difficult to identify chatter without assistance of surface topography during micro-milling process. The determination of tool point dynamics and burr suppression are still promising research direction of micro-milling. In addition, due to the relative flexibility of tool, the application of new materials to micro-milling tool and dynamics analysis, especially in micro-milling tool design and manufacture, are also the research directions worthy of further study.

In addition to the dynamics of milling tool and workpiece, runout of the milling tool, thermal errors, tool wear and the external environment factors will affect the machining process as well. Therefore, how to select the influence factors for the machining system is also an important issue that needs deep consideration.

Reference

[1] Schmitz TL, Smith KS. Machining dynamics: frequency response to improved productivity, Springer, New York, second edition; 2019.

[2] Quintana G, Ciurana J. Chatter in machining processes: A review. Int J Mach Tools Manuf. 2011;51:363-376.

[3] Yue CX, Gao HN, Liu XL, Liang SY, Wang LH. A review of chatter vibration research in milling. Chin. J. Aeronaut. 2019;32(2):215-242.

[4] Cheng K, Huo DH. Micro-cutting: fundamentals and applications, Wiley, Chichester;2013.

[5] Altintas Y, Budak E. Analytical prediction of stability lobes in milling. Annals of CIRP, 1995;44(1):357-362.

[6] Bravo U, Altuzarra O, Lopez de Lacalle LN, Sanchez JA, Campa FJ. Stability limits of milling considering the flexibility of the workpiece and the machine. Int J Mach Tools Manuf. 2005;45:1669-1680.

[7] Eksioglu C, Kilic MC, Altintas Y. Discrete-Time Prediction of Chatter Stability, Cutting Forces and Surface Location Errors in Flexible Milling Systrms. Manuf Sci Eng. 2012;134:061006-1-061006-13.

[8] Iglesias A, Munoa J, Ciurana J, Dombovari Z, Stepan G. Analytical expressions for chatter analysis in milling operations with one dominant mode. J Sound Vib. 2016;375:403-421.

[9] Yan ZH, Wang XB, Liu ZB, Wang DQ, Jiao L, Ji YJ. Third-order updated full-discretization method for milling stability prediction, Int J Adv Manuf Technol. 2017;92:2299-2309.

[10] Peng C, Wang L, Liao TW. A new method for the prediction of chatter stability lobes based on dynamic cutting force simulation model and support vector machine, J Sound Vib. 2015;354:118-131.

[11] Friedrich J, Hinze C, Renner A, Verl A, Lechler A. Estimation of stability lobe diagrams in milling with continuous learning algorithms, Robot. Comput.-Integr. Manuf. 2017;43:124-134

[12] Löser M, Otto A, Ihlenfeldt S, Radons G. Chatter prediction for uncertain parameters, Adv. Manuf. 2018;6:319-333.

[13] Mann BP, Garg NK, Young KA, Helvey AM. Milling bifurcations from structural asymmetry and nonlinear regeneration. Nonlinear Dyn. 2005;42:319-337.

[14] Balachandran B. Nonlinear dynamics of milling processes. Philosophical Transactions: Mathematical, Physical and Engineering Sciences. 2001;359:793-819.

[15] Seguy S, Dessein G, Arnaud L. Surface roughness variation of thin wall milling, related to modal interactions. Int J Mach Tools Manuf. 2008;48:261-274.

[16] Thevenot V, Arnaud L, Dessein G, Cazenave-Larroche G. Integration of dynamic behaviour variations in the stability lobes method: 3D lobes construction and application to thin-walled structure milling. Int J Adv Manuf Technol. 2006;27:638-644.

[17] Munoa J, Dombovari Z, Mancisidor I, Yang YQ, Zatarain M. Interaction between multiple modes in milling processes. Mach. Sci. Technol. 2013;17:165-180.

[18] Wan M, Ma YC, Zhang WH, Yang Y. Study on the construction mechanism of stability lobes in milling process with multiple modes, Int J Adv Manuf Technol. 2015;79:589-603.

[19] Zhang XJ, Xiong CH, Ding Y, Zhang XM. Stability analysis in milling of thin-walled workpieces with emphasis on the structural effect. Proc. Inst. Mech. Eng. Part B-J. Eng. Manuf. 2010;224(4): 589-608.

[20] Özşahin O, Budak E, Özgüven HN. In-process tool point FRF identification under operational conditions using inverse stability solution. Int J Mach Tools Manuf. 2015;89:64-73.

[21] Budak E, Tunc LT, Atlar S, Özgüven HN. Prediction of workpiece dynamics and its effects on chatter stability in milling, CIRP Annals, 2012;61:339-342.

[22] Olvera D, Elías-Zúñiga A, Martínez-Romero O, López de Lacalle LN, Martínez-Alfaro H, Siller HR, Pineda MW. Improved predictions of the stability lobes for milling cutting operations of thin-wall components by considering ultra-miniature accelerometer mass effects. Int J AdvManuf Technol, 2016;86:2136-2146.

[23] Biermann D, Kersting P, Surmann T. A General Approach to Simulating Workpiece Vibrations During Five-Axis Milling of Turbine Blades, CIRP Annals, 2010;59(1):125-128.

[24] Stepan G, Kiss A, Ghalamchi B, Sopanen Jussi, Bachrathy D. Chatter avoidance in cutting highly flexible workpieces. CIRP Annals, 2017;66(1):377-380.

[25] Thevenot V, Arnaud L, Dessein G, Cazenave–Larroche G. Influence of material removal on the dynamic behavior of thin-walled structures in peripheral milling. Mach. Sci. Technol. 2006;10:275-287.

[26] Tuysuz O, Altintas Y. Frequency domain updating of thin-walled workpiece dynamics using reduced order substructuring method in machining. Manuf Sci Eng. 2017;139:071013-1-071013-16.

[27] Tuysuz O, Altintas Y. Time-domain modeling of varying dynamic characteristics in thin-wall machining using perturbation and reduced-order substructuring methods, Manuf Sci Eng. 2018;140:011015-1-011015-15.

[28] Song QH, Liu ZQ, Wan Y, Ju GG, Shi JH. Application of Sherman-Morrison-Woodbury formulas in instantaneous dynamic of peripheral milling. Int J Mech Sci. 2015;96-97:79-90.

[29] Dang XB, Wan M, Yang Y, Zhang WH. Efficient prediction of varying dynamic characteristics in thin-wall milling using freedom and mode reduction methods. Int J Mech Sci. 2019;150:202-216.

[30] Hamann D, Eberhard P. Stability analysis of milling processes with varying workpiece dynamics. Multibody Syst Dyn 2018;42:383-396.

[31] Yang Y, Zhang WH, Ma YC, Wan M. Chatter prediction for the peripheral milling of thin-walled workpieces with curved surfaces. Int J Mach Tools Manuf. 2016;109:36-48.

[32] Mann BP, Young KA, Schmitz TL, Dilley DN. Simultaneous stability and surface location error predictions in milling. Manuf Sci Eng. 2005;127(3):446-453.

[33] Wan M, Ma YC, Feng J, Zhang WH. Study of static and dynamic ploughing mechanisms by establishing generalized model with static milling forces, Int J Mech Sci. 2016;114:120-131.

[34] Altintas Y. Manufacturing automation: Metal cutting mechanics, machine tool vibrations and CNC design, Cambridge university press, Second edition; 2012.

[35] Das MK, Tobias SA. The relation between the static and the dynamic cutting of metals. International Journal of Machine Tool Design and Research, 1967;7:63-89.

[36] Sisson TR, Kegg RL. An explanation of low speed chatter effects. J. Eng. Ind. 1969;91(4):951-955.

[37] Chiou RY, Liang SY. Chatter stability of a slender cutting tool in turning with wear effect. Int J Mach Tools Manuf. 1998;38(4):315-327.

[38] Budak E, Tunc LT. A new method for identification and modeling of process damping in machining. Manuf Sci Eng. 2009;131(5):051019-1-051019-10.

[39] Tunc LT, Budak E. Identification and modeling of process damping in milling. J. Manuf. Sci. Eng. 2013;135(2):021001-1-021001-12.

[40] Sellmeier V, Denkena B. High speed process damping in milling. CIRP J. Manuf. Sci. Technol. 2012;5:8-19.

[41] Molnar TG, Insperger T, Bachrathy D, Stepan G. Extension of process damping to milling with low radial immersion. Int J Adv Manuf Technol. 2017;89:2545-2556.

[42] Feng J, Wan M, Gao TQ, Zhang WH. Mechanism of process damping in milling of thin-walled workpiece. Int J Mach Tools Manuf. 2018;134:1-19.

[43] Kiran K, Rubeo M, Kayacan MC, Schmitz TL. Two degree of freedom frequency domain surface location error prediction. Precis Eng. 2017;48:234-242.

[44] Insperger T, Gradišek J, Kalveram M, Stépán G, Winert K, Govekar E. Machine Tool Chatter and Surface Location Error in Milling Processes. Manuf Sci Eng. 2006;128:913-919.

[45] Schmitz TL, Mann BP. Closed-form solutions for surface location error in milling. Int J Mach Tools Manuf. 2006;46(12-13):1369-1377.

[46] Mann BP, Edes BT, Easley SJ, Young KA, Ma K. Chatter vibration and surface location error prediction for helical end mills, Int J Mach Tools Manuf. 2008;48:350-361.

[47] Ding Y, Zhang XJ, Ding H. On a numerical method for simultaneous prediction of stability and surface location error in low radial immersion milling. J. Dyn. Syst. Meas. Control-Trans. ASME. 2011;133:024503-1-024503-8.

[48] Zhang X, Zhang W, Zhang J, Pang B, Zhao WH. Systematic study of the prediction methods for machined surface topography and form error during milling process with flat-end cutter. Proc. Inst. Mech. Eng. Part B-J. Eng. Manuf. 2019:233(1):226-242.

[49] Dai YB, Li HK, Yao JX, Liu SX. A novel approach with time-invariant transition matrix for surface location error prediction in low radial immersion milling. Int J Adv Manuf Technol. 2019;101:1267-1274.

[50] Schmitz TL, Ziegert J. Examination of surface location error due to phasing of cutter vibrations. Precis Eng. 1999;23:51-62.

[51] Schmitz TL, Couey J, Marsh E, Mauntler N, Hughes D. Runout effects in milling: Surface finish, surface location error, and stability. Int J Mach Tools Manuf. 2007;47:841-851.

[52] Kurdi MH. Robust multicriteria optimization of surface location error and material removal rate in high-speed milling under uncertainty. Dissertation: University of Florida; 2005.

[53] Ramos R. Applying decision analysis to milling with system dynamics constraints: a new frontier in machining science. Dissertation: University of Florida; 2009.

[54] Bachrathy D, Insperger T, Stépán G. Surface properties of the machined workpiece for helical mills. Mach Sci Technol. 2009;13(2):227-245.

[55] Siebrecht T, Kersting P, Biermann D, Odendahl S, Bergmann J. Modeling of surface location errors in a multi-scale milling simulation system using a tool model based on triangle meshes. Procedia CIRP, 2015;37:188-192.

[56] Honeycutt A, Schmitz TL. Surface location error and surface roughness for period-N milling bifurcations. Manuf Sci Eng. 2017;139(6):061010-1-061010-8.

[57] Yuan L, Zeng SS, Chen ZB. Simultaneous prediction of surface topography and surface location error in milling. Proc. Inst. Mech. Eng. Part C-J. Eng. Mech. Eng. Sci. 2015:229(10):1805-1829.

[58] Kiss KA, Bachrathy D. Explicit model of cumulative surface location error in milling processes. 12th Hungarian Conference on Theoretical and Applied Mechanics HCTAM, Miskolc, Hungary, 2015.

[59] Kiss KA, Bachrathy D, Stépán G. Cumulative surface location error for milling processes based on tool-tip frequency response function. Procedia CIRP, 2016;46:323-326.

[60] Li ZL, Tuysuz O, Zhu LM, Altintas Y. Surface form error prediction in five-axis flank milling of thin-walled parts. Int J Mach Tools Manuf. 2018;128:21-32.

[61] Chen WQ, Teng XY, Huo DH, Wang QL. An improved cutting force model for micro milling considering machining dynamics. Int J Adv Manuf Technol. 2017;93(9-12):3005-3016.

[62] Anad RS, Patra K. Modeling and simulation of mechanical micro-machining—A review. Mach. Sci. Technol. 2014;18(3):323-347.

[63] Bao WY, Tansel IN. Modeling micro-end-milling operations, Part I: analytical cutting force model. Int J Mach Tools Manuf. 2000;40(15):2155-2173.

[64] Malekian M, Park SS, Jun MBG. Modeling of dynamic micro-milling cutting forces. Int J Mach Tools Manuf. 2009;49(7-8):586-598.

[65] Afazov SM, Ratchev SM, Segal J. Modelling and simulation of micro-milling cutting

forces. Mater Process Technol. 2010;(15):2154-2162.

[66] Afazov SM, Ratchev SM, Segal J, Popov AA. Chatter modelling in micro-milling by considering process nonlinearities. Int J Mach Tools Manuf. 2012;56:28-38.

[67] Rezaei H, Sadeghi MH, Budak E. Determination of minimum uncut chip thickness under various machining conditions during micro-milling of Ti-6Al-4V. Int J Adv Manuf Technol. 2018;95(5-8):1617-1634.

[68] Boswell B, Islam MN, Davies IJ. A review of micro-mechanical cutting. Int J Adv Manuf Technol. 2018;94(1-4):789-806.

[69] Schmitz TL. Predicting High-speed machining dynamics by substructure analysis, CIRP Annals. 2000;49(1):303-308.

[70] Zhang J, Tony S, Zhao W, Lu BH. Receptance coupling for tool point dynamics prediction on machine tools. Chin. J. Mech. Eng. 2011;24(3):340-345.

[71] Schmitz TL, Burns TJ, Ziegert JC. Tool length-dependent stability surfaces, Mach Sci Technol. 2004;8(3):377-397.

[72] Schmitz TL, Duncan GS. Three-component receptance coupling substructure analysis for tool point dynamics prediction, Manuf Sci Eng. 2005;127(4):781-790.

[73] Mascardelli BA, Simon SP, Theodor F. Substructure coupling of micro-end mills to aid in the suppression of chatter, Manuf Sci Eng. 2008;130(1):011010-1-011010-12.

[74] Lu XH, Jia ZY, Zhang HX, Liu SQ, Feng YX, Liang SY. Tool point frequency response prediction for micromilling by receptance coupling substructure analysis, Manuf Sci Eng. 2017;139(7):071004-1-071004-13.

[75] Novakov T, Jackson MJ. Chatter problems in micro- and macrocutting operations, existing models, and influential parameters-a review. Int J Adv Manuf Technol. 2010; 47:597-620.

[76] Wang DQ, Wang XB, Liu ZB, Gao P, Ji YJ, Löser M, Ihlenfeldt S. Surface location error prediction and stability analysis of micro-milling with varia.tion of tool overhang length. Int J Adv Manuf Technol. 2018;99:919-936.

[77] Zhang XM, Zhu LM, Zhang D, Ding H, Xiong YL. Numerical robust optimization of spindle speed for milling process with uncertainties. Int J Mach Tools Manuf. 2012;61:9-19.

[78] Insperger T, Munoa J, Zatarain M, Peigné G. Unstable islands in the stability chart of milling processes due to the helix angle. CIRP 2nd International Conference on High Performance Cutting. 2006;12-13.

[79] Zatarain M, Munoa J, Peigne G, Insperger T. Analysis of the influence of mill helix angle on chatter stability. Annals of the CIRP, 2006;55:1-4.

[80] Sol I, Rivero A, Lacalle L, Gamez A. Thin-wall machining of light alloys: a review of models and industrial approaches. Materials. 2019;12(12):2012.

[81] Gradisek J, Kalveram M, Insperger T, Weinert K, Stepan G, Govekar E, Grabec I. On stability prediction for milling. Int J Mach Tools Manuf. 2005;45:769-781.

[82] Junior MV, Baptista EA, Araki L, Schmitz T. The role of tool presetting in milling

stability uncertainty. Procedia Manufacturing, 2018:1-9.

[83] Sun YW, Jiang SL. Predictive modeling of chatter stability considering force-induced deformation effect in milling thin-walled parts. Int J Mach Tools Manuf. 2018;135:38-52.

[84] Insperger T, Stépán G. Updated semi-discretization method for periodic delay-differential equations with discrete delay. Int J Numer Meth Eng. 2004;61(1):117-141.

[85] Ding Y, Zhu LM, Zhang XJ, Ding H. Second-order full-discretization method for milling stability prediction. Int J Mach Tools Manuf. 2010;50(10):926-932.

[86] Tang X, Peng F, Yan R, Gong Y, Li Y, Jiang L. Accurate and efficient prediction of milling stability with updated full-discretization method. Int J Adv Manuf Technol. 2017;88(9-12):2357-2368.

[87] Ding Y, Zhu LM, Zhang XJ, Ding H. A full-discretization method for prediction of milling stability. Int J Mach Tools Manuf. 2010;50(5):502-509.

[88] Zhou ZH. Machine Learning, Tsinghua University Press, 2016.

[89] Kuljanic E, Sortino M, Totis G Multisensor approaches for chatter detection in milling. J Sound Vib. 2008;312:672-693.

[90] Schmitz TL. Chatter recognition by a statistical evaluation of the synchronously sampled audio signal. J Sound Vib. 2003;262:721-730.

[91] Hynynen KM, Ratava J, Lindh T,Rikkonen M, Ryynanen V, Lohtander M, Varis J. Chatter detection in turning processes using coherence of acceleration and audio signals. Manuf Sci Eng. 2014;136: 044503-1-044503-4.

[92] Steve Suh. C, Liu MK. Control of cutting vibration and machining instability: A time-frequency approach for precision, micro and nano machining. Wiley, London, 2013.

[93] Nad M. Structural dynamic modification of vibration systems, Applied and Computational Mechanics, 2007;1:203-214.

[94] Huang CY, Wang JJJ. Mechanistic modeling of process damping in peripheral milling. J Manuf Sci Eng. 2007;129:12-20.

[95] Wu DW. Application of a comprehensive dynamic cutting force model to orthogonal wave-generating processes. Int J Mech Sci. 1998;30(8):581-600.

[96] Sims ND, Turner MS. The influence of feed rate on process damping in milling modelling and experiments. Proc. Inst. Mech. Eng. Part B-J. Eng. Manuf. 2011;225(6):799-810.

[97] Surmann T, Biermann D, Kehl G. Oscillator model of machine tools for the simulation of self excited vibrations in machining processes, The 1st International Conference on Process Machine Interactions, Hannover, 2008;23-29.

[98] Biermann D, Surmann T, Kersting P. Oscillator-based approach for modeling process dynamics in NC milling with position and time-dependent modal parameters. Prod. Eng. Res. Devel. 2013;7:417-422.

[99] Insperger T, Stepan G, Bayly PV, Mann BP. Multiple chatter frequencies in milling processes, J Sound Vib. 2003;262:333-345.

[100] Insperger T, Mann BP, Surmann T, Stepan G. On the chatter frequencies of milling processes with runout, Int J Mach Tools Manuf. 2008;48:1081-1089.

[101] Kiss KA, Bachrathy D. Experimental validation of cumulative surface location error for turning processes. Acta Polytechnica CTU Proceedings, 2016;3:25-29.

[102] Filho JMC, Negri D, Melotti S. Stable milling of cantilever plates using shell finite elements. Int J Adv Manuf Technol. 2018;99(9-12):2677-2693.

[103] Bachrathy D, Stépán G. Bisection method in higher dimensions and the efficiency number. Periodica Polytechnica Mechanical Engineering, 2012;56(2):81-86.

[104] Wang DQ, Löser M, Ihlenfeldt S, Wang XB, Liu ZB. Milling stability analysis with considering process damping and mode shapes of in-process thin-walled workpiece. Int J Mech Sci. 2019;159:382-397.

[105] Malekian M, Mostofa MG, Park SS, Jun MBG. Modeling of minimum uncut chip thickness in micro machining of aluminum, Mater Process Technol. 2012;212(3):553-559.

[106] Grossi N, Sallese L, Scippa A, Campatelli G. Speed-varying cutting force coefficient identification in milling. Precis Eng. 2015;42:321-334.

Appendix

Data for the parameter of 12100-8

Position	CSLE (μm)	Angle A (°)	Angle B (°)	Angle C (°)
CL0-1	140.92			
CL0-2	134.78	1.60	1.3	2.9
CL0-3	92.7			
CL1-1	110			
CL1-2	114.56	0.71	0.33	1.04
CL1-3	60.87			
CL2-1	110.36			
CL2-2	87.51	0.4	0.41	0.81
CL2-3	102.41			
CL3-1	101.65			
CL3-2	103.48	0.6	0.33	0.27
CL3-3	105.37			
CL4-1	39.01			
CL4-2	35.31	0.735	0.005	0.74
CL4-3	45.88			

Data for the parameter of 12100-12

Position	CSLE (μm)	Angle A (°)	Angle B (°)	Angle C (°)
CL0-1	168.86			
CL0-2	126.72	0.03	0.62	0.59
CL0-3	137.79			
CL1-1	148.86			
CL1-2	159.96	1.2	0.3	0.9
CL1-3	155.41			
CL2-1	89.48			
CL2-2	77.31	0.03	0.51	0.48
CL2-3	91.08			
CL3-1	43.84			
CL3-2	82.54	0.78	0.54	1.32
CL3-3	52.02			
CL4-1	58.23			
CL4-2	39.87	0.18	0.38	0.2
CL4-3	74.95			

Data for the parameter of 12250-12

Position	CSLE (µm)	Angle A (°)	Angle B (°)	Angle C (°)
CL0-1	114.17			
CL0-2	97.75	0.25	0.33	0.58
CL0-3	96.4			
CL1-1	105.1			
CL1-2	99	0.37	0.29	0.66
CL1-3	87.9			
CL2-1	82.12			
CL2-2	81.92	0.66	0.41	1.07
CL2-3	62.54			
CL3-1	56.83			
CL3-2	42.28	0.64	0.13	0.51
CL3-3	60.13			
CL4-1	35.53			
CL4-2	41.4	0.8	0.08	0.88
CL4-3	60.05			

Data for the parameter of 12400-8

Position	CSLE (µm)	Angle A (°)	Angle B (°)	Angle C (°)
CL0-1	132.57			
CL0-2	104.57	1.05	0.1	0.95
CL0-3	122.65			
CL1-1	116.17			
CL1-2	77.56	0.86	0.38	1.24
CL1-3	58.6			
CL2-1	124.79			
CL2-2	106.81	0.63	0.36	0.99
CL2-3	118.45			
CL3-1	83.33			
CL3-2	76.64	0.64	0.36	1
CL3-3	80.73			
CL4-1	72.65			
CL4-2	54.59	0.44	0.15	0.29
CL4-3	66.33			